Free-standing Silicon Quantum Dot Photoluminescence

by

Ross Andrew Lockwood

A thesis submitted in partial fulfillment of the requirements for the degree of

Doctor of Philosophy

Department of Physics
University of Alberta

Abstract

This thesis focuses on the photoluminescence (PL) of free-standing silicon quantum dots (QDs). Large changes in the emission spectrum were found to occur when the QDs were exposed to different environments while undergoing short-wavelength laser irradiation, a phenomenon that was the main focus of this thesis. In particular, the PL can change in intensity by orders of magnitude, either increasing or decreasing, depending on the gases or vapors present in the surrounding atmosphere. The presence of chemical species with -OH groups produced especially strong and rapid effects, when in the presence of oxygen. This process was found to feature a rapid reconstruction and oxidation of the Si-QD surface, as measured by Fourier transform infrared spectroscopy (FTIR) and electron spin resonance (ESR). A model for the physical and chemical changes that silicon QDs undergo during these surprisingly strong changes in the PL intensity was developed, factoring in the results from a range of experiments. The effects reported here suggest that silicon QDs could be used to "sense" changes in the surrounding atmosphere. Therefore, a silicon-QD-based fiber optic sensor was demonstrated and its viability for detecting ethanol and water vapors was established. Finally, the outstanding challenges and potential for future research were discussed in light of improving the selectivity and detection limits for sensors based on the luminescence of free-standing silicon QDs.

Preface

This thesis is an original work by Ross Lockwood. Chapters 3, 4 and 5 are first authored papers in which I am the main contributor. Appendix A is a co-authored paper, directly related to this thesis work; the lead author was a visiting student that I helped supervise for the data collection and analysis therein. Some changes to these publications were made to reflect the format of this thesis. Several other relevant papers were co-authored during my graduate work, but they are not included in this work. My supervisor, Dr. Al Meldrum, contributed intellectually to all aspects of this work from experiment design to publication.

Figures reproduced herein fall under Section 29 of the Copyright Act (R.S.C., 1985, c. C-42); reproductions and modifications of figures is stated in their captions. Section 29 expressly permits an exception for reproduction of copyrighted works for the purpose of research:

29. Fair dealing for the purpose of research, private study, education, parody or satire does not infringe copyright. R.S., 1985, c. C-42, s. 29; R.S., 1985, c. 10 (4th Supp.), s. 7; 1994, c. 47, s. 61; 1997, c. 24, s. 18; 2012, c. 20, s. 21.

Acknowledgements

This work represents a substantial fraction of my adult life, the creation of which seems Sisyphean in retrospect. It is humbling to not only make a discovery, however small, but share it for the benefit of future generations. It gives me great pleasure to acknowledge that I could not have created this work on my own, and to give thanks to everyone that contributed to its realization.

To Al Meldrum and the students he supervised: Aaron, Sulan, Yanyan, Shalon, Kyle, Stephen, and Zhihong: you have been the force driving my curiosity and guiding my discoveries. I owe an immeasurable debt to all of you for helping me with my research and for motivating me to grow professionally. Not only has your guidance been a tremendous help, but your flexibility in allowing me to explore my own interests has granted me experiences that few people are privileged to have.

Numerous academics and their students were also instrumental in my research. Jon Veinot from the Department of Chemistry and students in his group: José, Kevin, Iqbal, Tapas, and Christina; Ramaswami Sammynaiken and Gabriele Schatte at the Saskatchewan Structural Sciences Centre; Marek Malec and Xiongyao Wang at the National Institute for Nanotechnology: you have exceeded my expectations about collaboration, and it gives me great pride to know that our work together has led to dozens of co-authored publications. Don Mullen, Greg Popowich, and the rest of the technical and administrative staff in the Department of Physics: you helped me through all aspects of my graduate experience. Thank you for all your support.

Finally, it must be acknowledged that the PhD process is difficult, not only to myself, but to my family and friends who supported me throughout: Janet, Ron, Karla, Mark, Sarah and the Martens family: you have seen me through every frustration and every celebration. To you I owe the biggest debt of all, and recognize all that you have sacrificed to get me where I am today.

To everyone who has had a role in any aspect of this great adventure, I dedicate this to you:

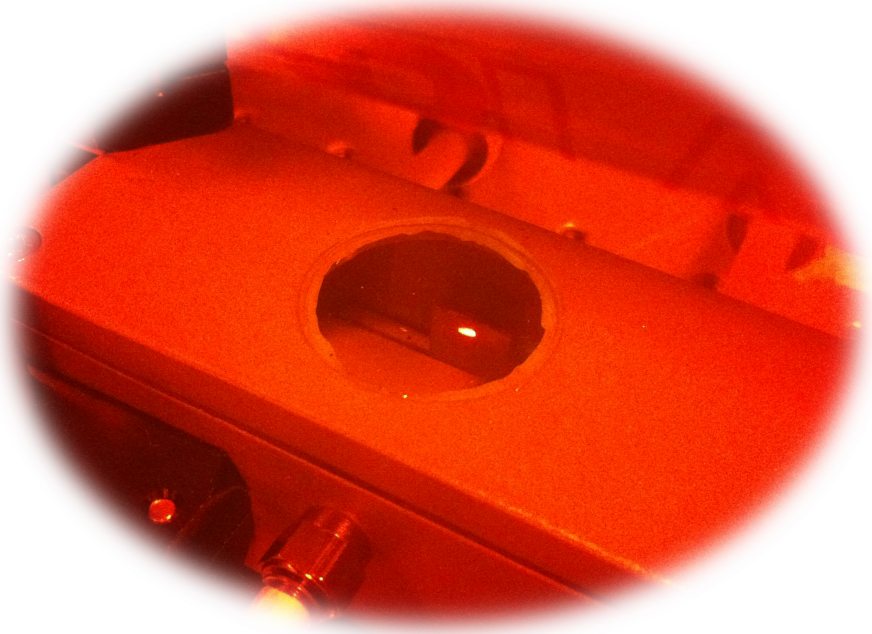

the future is ***bright***.

Table of Contents

List of Tables

List of Figures

List of Abbreviations

EELS	electron energy-loss spectroscopy
EFSTEM	energy-filtered transmission electron microscopy
ESR	electron spin resonance
FTIR	fourier transform infrared spectroscopy
HRTEM	high-resolution transmission electron microscopy
HSQ	hydrogensilsesquioxane
MIBK	methy isobutyl keytone
NMR	nuclear magnetic resonance
PA	photoactivation
PL	photoluminescence
PMT	photomultiplier tube
PSi	porous silicon
QD	quantum dot
SEM	scanning electron microscope
Si-QD	silicon quantum dot
TEM	transmission electron microscope

Chapter 1

Introduction: Photoluminescence in Nanoscale Silicon

Silicon plays a fundamental role in modern microelectronics. It comprises the major component of semiconductor transistors, which represent the building block for modern microprocessors and digital logic [1]. Technological developments continue to push devices to smaller sizes, in part due to the demand for smaller components and lower energy consumption. However, silicon technology is quickly approaching its theoretical size limit, which is dictated by the ability for components to dissipate heat and by quantum effects that occur when the dimensions are comparable to the electron wavelength [2, 3]. The implementation of silicon photonics, (*i.e.*, the use of silicon as an optical medium), to replace some aspects of standard microelectronics holds promise to reduce or eliminate problems associated with heat dissipation [4].

The bandgap of silicon is indirect, which means that direct optical transitions are forbidden in the bulk crystal, [5, 6]. Bulk silicon is therefore an inefficient light emitter, and did not seem to represent a promising route toward photonic technologies. However, a breakthrough occurred in 1990, with the discovery of room temperature light emission from porous silicon [7]. Light emission from silicon nanocrystals had previously been reported by Furukawa and Miyasato [8], but they did not include photoluminescence (PL) data or an explanation of the phenomenon. Luminescent nanoscale silicon (including porous silicon, oxide-embedded silicon quantum dots, and free-standing silicon quantum dots) have been since found to hold promise as

a bridging technology between silicon microelectronics and silicon photonics [9]. As we shall see however, the light emission mechanisms from nanoscale silicon seem far from optimal and are still highly debated [10].

Light-emitting nanocrystalline silicon has potential applications ranging from biological labels [11] to surface-accessible direct chemical sensors. Porous silicon (PSi; described below) in particular has been extensively researched for sensing applications for the last 30 years [12–28]. Oxide-embedded silicon quantum dots were suggested for sensing applications at least 10 years ago [29]. More recently, modern chemical synthesis techniques have been used to generate "free-standing" silicon quantum dots (Si-QDs) [30, 31]. These Si-QDs have a number of interesting and advantageous properties, due to their freely-accessible surfaces, which will be described in detail in this work.

Free-standing silicon quantum dots are not attached to a silicon backbone (as in porous silicon) or embedded in a solid matrix. Their geometry may overcome some of the limitations of porous silicon and oxide-embedded silicon quantum dots. For example, they are suspended and stored in non-polar solutions, which can be used to apply the particles to a variety of surfaces [32]. Due to their exposed surfaces, the QDs are more chemically accessible, which translates into a greater sensitivity to changes in their chemical environment.

The objectives of this thesis are therefore:

1. To describe the surface structural changes that affect the photoluminescence of free-standing silicon quantum dots. This is important because changes to the surface structure can control the luminescence spectrum and efficiency.

2. To demonstrate a chemical sensor for atmospheric vapors based on the surface structural changes that occur in free-standing silicon quantum dots. Based on the extensive previous work on luminescent PSi [13–19, 27, 28], the development of a free-standing silicon quantum dot sensor might increase sensitivity of existing nanoscale silicon sensors.

3. To generate a physical and chemical model of the processes involved in objectives 1 and 2 above. To use this model to predict how free-standing silicon quantum dots can behave as chemical sensors.

1.1 Nanoscale Silicon

Silicon was first isolated as an amorphous solid by Berzelius in 1823 [33], and in its crystalline form by Wöehler in 1843 [34], but its semiconductor properties were not well known until almost a century later due to the difficulty in producing a pure crystalline solid [35]. In 1947 the transistor effect in Si was discovered by Bardeen and Brattain at Bell Labs, sparking the semiconductor and microelectronics revolution [36,37]. Today, we are fast approaching the limits of Si microelectronics [2], and research is now turning toward the photonic capabilities of Si for its use in emerging technologies [4].

Porous silicon (PSi) was discovered by Uhlir in 1956, through electrochemical dissolution of silicon in hydrofluoric acid [38], but it wasn't until the mid-1980s that it was studied in earnest [39–41]. PSi consists of a network of deep pores extending perpendicular to the surface of a silicon wafer. The pores range in diameter from nanometers to micrometers, and they can extend up to a millimeter into the bulk of the wafer [42]. The remaining crystalline "skeleton" consists of rod-like bridges between crystalline domains with diameters typically between 3 and 10 nanometers (Fig. 1.1 and Fig. 1.2 (a) [13, 42].

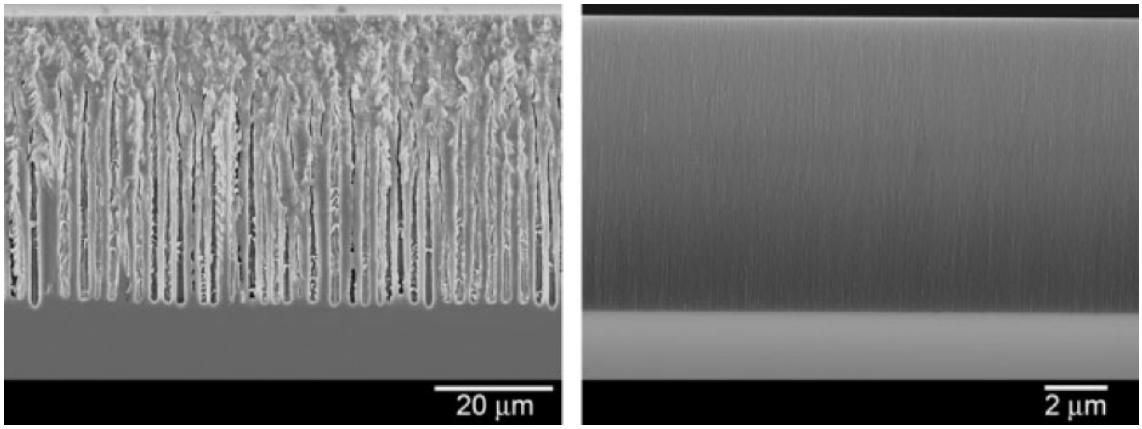

Figure 1.1. Scanning electron micrograph showing porous silicon samples in cross-section. The samples shown in the left and right images were etched under the same conditions, but the left sample was n-type silicon, whereas the right sample was heavily-doped p^{++} type. Figure reproduced from reference [27].

Interest in the use of PSi as a sensor preceded the discovery of its room-temperature photoluminescence, due to the large surface area available for chemical reactions

within the PSi network ($\sim$200 m^2/cm^3) [12]. Several different prototype sensors were proposed, based on the physical and chemical changes that can occur upon exposure to atmospheric water, alcohols, and oxidizing agents (Sec. section 1.3.2). However, the PSi system is inherently limited to flat geometries because the material is synthesized *via* wet chemical etching of a silicon wafer. Additionally, PSi tends to be mechanically brittle and quite fragile due to the nature of the interconnected porous silicon network. Furthermore, devices based on PSi cannot easily be manufactured in-situ with common CMOS processing techniques, since the PSi regions require wet-chemical etching that would destroy any unprotected parts on the wafer.

Oxide-embedded Si-QDs are nanocrystalline silicon particles that are embedded in a silica matrix (Fig. 1.2 (b)). They are usually manufactured by high-temperature annealing of silicon-rich oxides, which causes the excess silicon to nucleate and grow into Si-QDs. Silicon-rich oxides can be formed in various ways: for example, by ion-implantation [29, 43–47], physical or chemical vapor deposition [29, 43, 46–48], or laser ablation [49, 50]. Typical annealing temperatures range from 750 °C to 1100 °C, with Si-QD size increasing as a function of annealing temperature up to at least 950 °C [51]. Above 950 °C, the particle size can be controlled by varying the concentration of Si [51].

Si-QDs embedded in a silica matrix have limitations in comparison to PSi for sensing applications. The QDs are encapsulated by the oxide, restricting chemical access to the QD surface. Therefore, the luminescence is not significantly modified in the presence of atmospheric gases such as water, alcohols, or other oxidizing agents, which must diffuse through the solid host matrix in order to access the QD interface. For oxide-embedded QDs, the luminescence is more strongly controlled by the annealing temperature [51] and the annealing gas, which affects the luminescence *via* high-temperature diffusion of hydrogen and the resulting passivation of the QD surface [52].

Free-standing silicon quantum dots (FS-Si-QDs) [31] may circumvent many of the above-mentioned limitations of both PSi and oxide embedded Si-QDs (Fig. 1.2 (c)). Since the encapsulating oxide is removed, the FS-Si-QD surface is physically accessible to the surrounding medium. FS-Si-QDs have a larger surface area per unit volume than PSi, owing to the lack of the crystalline "skeleton". Finally, FS-

Si-QDs are not limited to flat geometries, unlike PSi, and can be applied to devices with curved surfaces such as microspheres and optical fibers. We will demonstrate later in this thesis that these qualities are beneficial toward the use of FS-Si-QDs as nanoscale sensors.

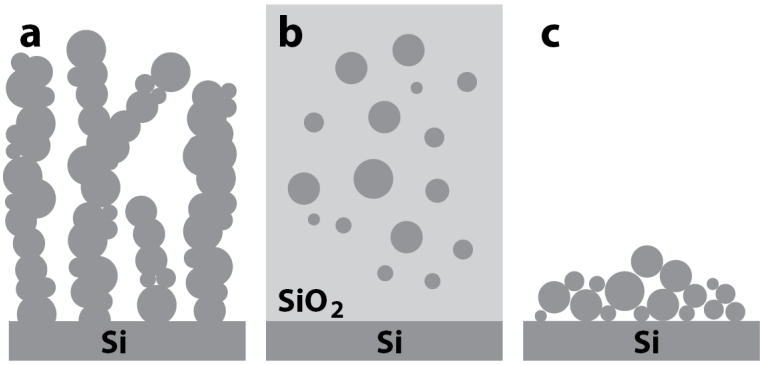

Figure 1.2. Diagram illustrating nanoscale silicon in various forms, a) porous silicon, b) oxide-embedded silicon quantum dots, and c) free-standing silicon quantum dots deposited on a Si wafer.

1.2 Origin of Photoluminescence in Nanoscale Silicon

In semiconductors, the electrons and holes (free carriers) can be excited across the bandgap by the absorption of photons. Absorption of a photon with energy greater than the bandgap energy excites an electron from the valence band into the conduction band. The bandgap energy for bulk silicon is 1.11 eV at 300 K [53]. However, the bandgap in nanoscale silicon (often referred to collectively as Si nanocrystals), depends strongly on the particle size.

Silicon has an indirect bandgap, so the emission of photons requires phonons in order to conserve momentum. Thus, lattice vibrations play an important role during the emission of radiation, and phonons must either be absorbed or emitted in indirect-gap transitions. This three-body process decreases the luminescence efficiency, especially at low temperatures [5, 6, 54]. The resulting slow radiative recombination rate increases the probability that carriers will participate in non-radiative combination due, for example, to the Auger effect or carrier capture at defects [54]. The internal quantum efficiency for bulk silicon luminescence is thus typically on the order of 10^{-6} [55].

In contrast to the case for bulk silicon, in 1990 Canham reported that PSi

can show bright photoluminescence at energies considerably higher than the bulk bandgap [7]. Initial reports of visible light emission from PSi were originally attributed to two-dimensional quantum confinement in free-standing Si quantum wires [7]. Since then, a number of theories explaining the origin of the luminescence of PSi have been developed, primarily based on quantum confinement models. These models state that the spatial confinement of electrons and holes causes an increase in the bandgap energy of Si. At the same time, the uncertainty principle permits the Γ-χ transition to take a direct-gap character, relaxing the need for momentum conserving phonons [54]. Spatial confinement also restricts the migration of free carriers, thus reducing the probability that they will be involved in non-radiative processes [54]. As a result of these various effects, materials like PSi, oxide embedded Si-QDs, and FS-Si-QDs can have much higher luminescence quantum efficiency than bulk silicon [7, 13, 29].

Since the discovery of light emission from nanoscale silicon, many reports have suggested that the origin of the luminescence is not due to quantum confinement alone, but is strongly affected by surface states in oxidized and partially oxidized samples [56–61]. For example, silicon-oxide structures like siloxene ($Si_6O_3H_6$) can be grown on bulk Si surfaces and they emit visible light in the yellow, red and near-infrared regions of the spectrum, with intensities comparable to that of porous silicon [56]. Some authors have reported that the peak photoluminescence wavelength of PSi does not change as a function of the depth of the surface oxide layer surrounding the PSi (thicker oxide layers reduce the size of the Si core), leading to the suggestion that oxide-related defects are the source of the luminescence rather than quantum confinement [57]. A later study of oxidized PSi proposed that carriers were confined to an amorphous oxide shell around the crystalline Si core and that emission was independent of core size [58]. Other studies suggested that the mechanisms for red and blue luminescence differ, with quantum confinement being responsible for the red emission and the oxide shell around the PSi being responsible for the blue emission [59–61]. Another model was proposed, in which the oxide shell ultimately controlled the peak emission wavelength of the nanocrystallites (discussed in Section 1.2.2) [62]. By the late 1990s, a rather large and bewildering array of mechanisms had been proposed to explain the PL of nanoscale silicon.

A common feature of most Si-QD systems is the relatively large difference between the absorption and photoluminescence energies [63]. This feature is generally referred to as a "Stokes shift" and is observable, to some degree, in the spectrum of virtually all fluorophores [64, 65]. For organic dyes, for example, the Stokes shift is typically smaller than 0.25 eV; however, in silicon QDs [64–66] the peak emission energy can be as much as 2 eV below the energy at which the QDs are strongly absorbing (Figs. 1.3 and 1.10). This Stokes shift can arise from several different physical processes [63]. In pure quantum models, the shift arises from electron-hole Coulomb and spin interactions amongst carriers in the lowest excited states, but these are typically on the order of the aforementioned 100 meV [66]. Larger Stokes shifts can occur if, for example, one absorbs across the silicon direct gap at 3.4 eV, and emits (after carrier thermalization) at the normal 1.1 eV bandgap [63]. However, many authors have suggested that the large Stokes shift in Si-QDs arises from the formation of radiative oxide-related sub-gap states [62, 67, 68]. In these models, the QDs absorb across the fundamental quantized energy gap, but the recombination happens after thermalization to the oxide-related radiative centers.

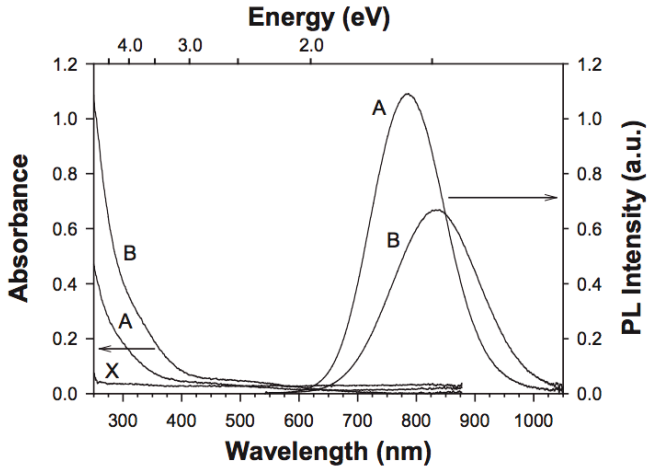

Figure 1.3. Absorption and emission spectra for two oxide-embedded Si-QD samples excited by 488 + 514 nm laser light (A with nanocrystal diameters of d ≈1.5 nm, σ =0.4 nm, and B with d ≈2.4 nm, σ =1.1 nm). X is the reference absorption spectrum of a blank fused quartz wafer. Figure modified from reference [66].

1.2.1 Quantum Confinement Effects

1.2.1.1 Confinement Energy

Quantum effects become apparent when the dimensionality of the material approaches the de Broglie wavelength of a particle in that system. An interesting (and relevant) example is the spatial confinement of electrons. In bulk materials, such as a metal or semiconductor, the electron density of states (DOS) is continuous (ignoring, of course, discontinuities like bandgaps caused by the crystalline lattice). However as the spatial dimensions are reduced, the structure of the DOS can be affected by quantum confinement, resulting in a quantization of the DOS. Materials having spatial confinement in one dimension are known as a quantum wells; in two dimensions they are known as quantum wires; and those with confinement in three dimensions are known as quantum dots (Fig. 1.4).

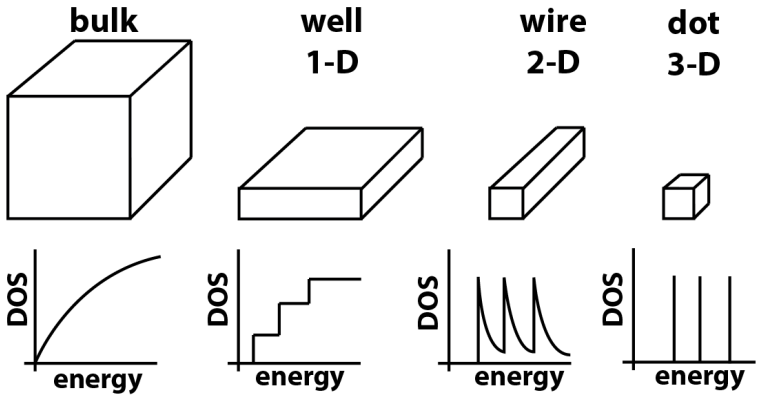

Figure 1.4. Density of states (DOS) as a function of energy for various dimensions of spatial confinement. As the dimensionality of spatial confinement increases, the DOS are modified from continuous (bulk) to discrete (dot). Figure modified from reference [69].

The simplest way to model the quantum confinement effect is to assume a particle in a spherically symmetric infinite potential well. The quantum confinement effect in the valence and conduction bands can be approximated by solving the quantum mechanical Hamiltonian for a carrier in a potential well [69]. This simple approximation, while not necessarily a complete picture, contains the basic physics needed to understand the fundamental origin of the effect. Thus, we will first examine the confinement energy for a particle in a spherical potential well. While this description is standard in many quantum dot text books, a brief review will help set the context

for the silicon QDs. We later discuss some refinements to the model that can capture more of the physics associated with the QDs.

Consider the Schrödinger Hamiltonian for quantum mechanical systems consisting of a particle of mass m

$$H = -\frac{\hbar}{2m}\nabla^2 + U(r), \tag{1.1}$$

where $-\hbar^2/(2m)\nabla^2$ is the kinetic energy operator and $U(r)$ is potential energy operator. Solutions for the energy of a quantum system can be calculated by allowing the Hamiltonian operator to act on a wavefunction

$$H\Psi = E\Psi, \tag{1.2}$$

where E represents the energy eigenstates of the system.

Equation 1.1 can be simplified for spherically symmetric potentials, $U(r)$, by making the transform between cartesian coordinates of x, y, and z, and a spherical coordinate system consisting of radius, r, polar angle, θ, and azimuthal angle ϕ, with $r = \sqrt{x^2 + y^2 + z^2}$

$$x = r\sin\theta\cos\phi,\ \ y = r\sin\theta\sin\phi,\ \ z = r\cos\theta. \tag{1.3}$$

Transforming Eq. 1.1 using Eq. 1.3 yields a modified Hamiltonian

$$H = -\frac{\hbar^2}{2mr}\frac{\partial}{\partial r}\left(r^2\frac{\partial}{\partial r}\right) - \frac{\hbar^2\Lambda}{2mr^2} + U(r), \tag{1.4}$$

where the Λ operator is given by

$$\Lambda = \frac{1}{\sin\theta}\left[\frac{\partial}{\partial\theta}\left(\sin\theta\frac{\partial}{\partial\theta}\right) + \frac{1}{\sin\theta}\frac{\partial^2}{\partial\phi^2}\right]. \tag{1.5}$$

The radial and angular components are separated, allowing the corresponding parts of the equation to be solved independently.

The wavefunction, Ψ, can also be separated into radial and angular components

$$\Psi_{n,l,m}(r,\theta,\phi) = \frac{u_{n,l}(r)}{r}Y_{l,m}(\theta,\phi), \tag{1.6}$$

where Y_{lm} are spherical functions in θ and ϕ. The function $u(r)$ satisfies a simplified version of Eq. 1.4

$$-\frac{\hbar^2}{2m}\frac{d^2u}{dr^2}+\left[U(r)+\frac{\hbar^2}{2mr^2}l(l+1)\right]u=Eu. \tag{1.7}$$

Here, Λ has been replaced by the radial solution $l(l+1)$, which comes from the spherical harmonic solutions, and E represents the energy eigenstate solution to Eq. 1.2. Since equation 1.7 is only a function of r, it can more readily be solved than equation 1.1.

The solutions for the Hamiltonian depend on the profile of the potential well, $U(r)$, and are most readily solved for the case of a spherical well with infinite potential barriers. Thus, we consider a model with infinite boundaries outside of a QD of radius a, such that

$$U(r)=\begin{cases}0 & \text{for } r\leq a\\ \infty & \text{for } r>a\end{cases}. \tag{1.8}$$

Since the boundaries are infinite, the wavefunction must be inside of the well ($r \leq a,\ U(r)=0$), and equation 1.7 simplifies to

$$\frac{d^2u(r)}{dr^2}=\left[\frac{l(l+1)}{r^2}-k^2\right]u(r). \tag{1.9}$$

Equation 1.9 has been simplified by using the substitution $k=\sqrt{2mE}/\hbar$ [70]. The general solution for equation 1.9 is given by

$$u(r)=Arj_l(kr)+Brn_l(kr), \tag{1.10}$$

where $j_l(kr)$ is the spherical Bessel function of the first kind with order l and proportionality constant A, and n_l is the spherical Bessel function of the second kind with order l and proportionality constant B. However, since spherical Bessel functions of the second kind go to infinity for r =0, B must be set to zero. The wavefunction $u(r)$ must also be zero at the boundary $r=a$, which adds the additional condition that $j_l(ka)$ =0. That is, the function $j_l(kr)$ must be a zero of the l^{th}-order spherical Bessel function at $r=a$. This requires that $ka=\chi_{nl}$, with χ_{nl} being the roots

(zeros) of the spherical Bessel equation (which are computed numerically), where n is the number of the root and l is the order of the function.

By substituting $k = \sqrt{2mE}/\hbar$ into $ka = \chi_{nl}$ we can solve for the quantum confinement energy

$$E_{nl} = \frac{\hbar^2 \chi_{nl}^2}{2ma^2} \ (eV). \tag{1.11}$$

The energy states are classified by the principal quantum number, n, and by the orbital quantum number, l, with every energy state having $(2l + 1)$ degeneracy. The orbital quantum number l determines the magnitude of the orbital angular momentum of the particle according to the equation $L^2 = l(l+1)\hbar^2$. A diagrammatic representation is given in Fig. 1.5.

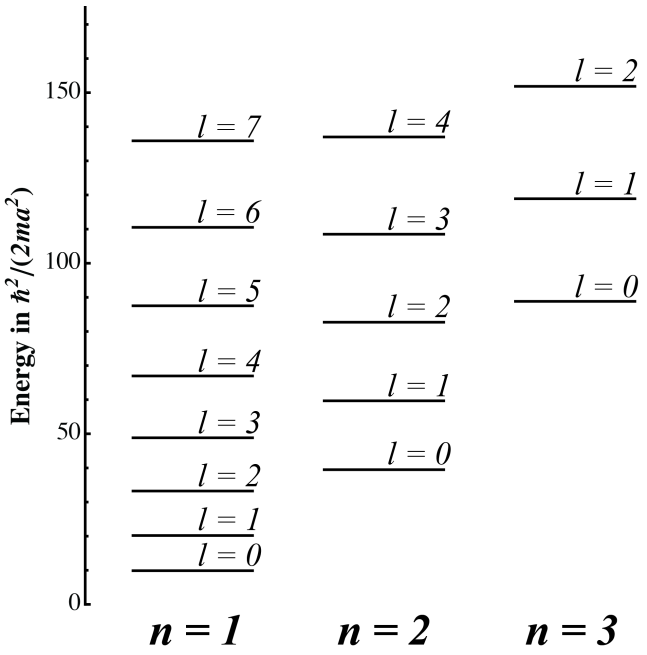

Figure 1.5. Energy levels of a particle with mass m in a spherically symmetric potential well of radius a. Energy is given in units of $\hbar^2/(2ma^2)$ at corresponding zeros of the Bessel function χ_{nl}^2. Figure modified from reference [69].

For l =0, the case where a particle has no orbital angular momentum, equation 1.11 reduces to the one-dimensional solution for a particle in a box

$$E_n = \frac{\hbar^2(\pi n)^2}{2ma^2} \ (eV), \tag{1.12}$$

which can be directly compared with equation 1.11. In both cases, the confinement energy is inversely proportional to the square of the well dimension, a. So, as a first approximation to the bandgap energy, we add the contribution calculated from the quantum confinement energy term of each particle, the electron, m_e, and the hole, m_h,

$$E = E_{gap} + \frac{\hbar^2 \chi_{nl}^2}{2m_e a^2} + \frac{\hbar^2 \chi_{nl}^2}{2m_h a^2} \ (eV). \tag{1.13}$$

This equation can be simplified by considering the reduced mass of the system, given by

$$\mu = \frac{m_e m_h}{m_e + m_h}, \tag{1.14}$$

which simplifies equation 1.13 to

$$E = E_{gap} + \frac{\hbar^2 \chi_{nl}^2}{2\mu a^2} \ (eV). \tag{1.15}$$

Equation 1.15 provides a simple picture of how the energy gap is affected by particle size. Experimentally, however, QDs cannot be thought of as having infinite potential barriers, implying that Equation 1.15 will overestimate the magnitude of the quantization effect. A complete model of the QD system would take a finite-barrier approach to the solution, but analytical solutions to finite barriers require additional complexity and their solutions are often approximated numerically [71].

1.2.1.2 Exciton Energy

An additional effect that modifies the bandgap energy is the binding energy of the electron and hole, known as the exciton energy. When an electron is promoted into the conduction band, a hole is left in the valence band. Since the electron is negatively charged and the hole positively charged, they attract one another and form a pseudo-particle known as an *exciton*. In the bulk crystal, the electron and hole can form a bound two-particle system that resembles the hydrogen atom. To model the interactions between electron and hole, the solution to the hydrogen atom can be modified to describe the electron-hole system by renormalizing the mass and

considering the behavior of a single-particle in an effective field (the same treatment given to the electron in the hydrogen system).

By analogy, we consider the hydrogen atom consisting of a proton of rest-mass M_0 and an electron of rest mass m_0, each interacting with each other *via* a mutual Coulomb potential (with elementary charge, e). The potential is given by

$$U(r) = -\frac{e^2}{r}. \tag{1.16}$$

The two-particle Hamiltonian for this system is written as

$$H = -\frac{\hbar^2}{2M_0}\nabla_p^2 - \frac{\hbar^2}{2m_0}\nabla_e^2 - \frac{e^2}{|r_p - r_e|}, \tag{1.17}$$

where $\mathbf{r}_p$ and $\mathbf{r}_e$ are the radius-vectors of the proton and electron. By introducing the relative radius vector, r, and the radius vector for the center of mass, R, given by

$$\mathbf{r} = \mathbf{r}_p - \mathbf{r}_e, \ \mathbf{R} = \frac{m_0\mathbf{r}_e + M_0\mathbf{r}_p}{m_o + M_0}, \tag{1.18}$$

as well as using the total mass, M and the reduced mass, μ, given by

$$M = m_0 + M_0, \text{ and } \mu = \frac{m_0 M_0}{m_0 + M_0}, \tag{1.19}$$

we can simplify equation 1.17 into the Hamiltonian of a free particle with rest mass (describing the center-of-mass motion of the two-particle atom), M, and a particle with mass μ in a potential $-e^2/r$ (describing the internal electronic states)

$$H = -\frac{\hbar^2}{2M}\nabla_R^2 - \frac{\hbar^2}{2\mu}\nabla_r^2 - \frac{e^2}{r}. \tag{1.20}$$

Solving the energy equation $H\Psi = E\Psi$ with this Hamiltonian gives rise to the well-known expression for the energy levels of the hydrogen atom

$$E_n = -\frac{Ry}{n^2}\ (eV), \tag{1.21}$$

where $Ry = e^2/2a_B$ is the Rydberg constant and $a_B = \hbar^2/\mu e^2$ is the Bohr radius.

This approach can be equivalently applied to an exciton in a crystal with a dielectric constant ϵ by replacing the mass of the proton and electron with the effective

masses of the electron (m_e^*) and hole (m_h^*) in equations 1.19. Thus, the *exciton Bohr radius* becomes:

$$a_B = \frac{\epsilon\hbar^2}{\mu e^2} = \epsilon\frac{m_0}{\mu} \times 0.53 \ \mathring{A} \tag{1.22}$$

and the *exciton Rydberg energy* becomes:

$$Ry^* = \frac{e^2}{2\epsilon a_B} = \frac{\mu e^4}{2\epsilon^2\hbar^2} = \frac{\mu}{m_0}\frac{1}{\epsilon^2} \times 13.6 \ (eV) \tag{1.23}$$

[69]. For silicon, the commonly accepted values of the electron effective mass and hole effective mass at 300 K are given as ([72] and references therein):

$$m_e = 1.09m_0, \ m_h = 1.15m_0, \tag{1.24}$$

which results in an exciton Rydberg energy of 15 meV and an exciton Bohr radius of 4.3 nm [69]. Note: for the infinite-well model, values for the effective mass of the electron and hole were chosen to demonstrate the maximum quantization energy.

Taking the results for spherical confinement together with the effective mass approximation for the binding energy of the exciton, we refine the energy of the excited state in two different regimes: the *weak confinement regime*, where the QD radius is greater than that of the Bohr exciton (*i.e.,* $a > a_B$), and the *strong confinement regime*, where the QD radius is much smaller than that of the Bohr exciton (*i.e.,* $a \ll a_B$). In the weak confinement regime, the QD energy is,

$$E_{nml} = E_{gap} - \frac{Ry^*}{n^2} + \frac{\hbar^2\chi_{nl}^2}{2Ma^2} \ (eV), \tag{1.25}$$

where M is the total mass of the exciton. The total energy is slightly reduced from the pure confinement situation, owing to the attraction between the electron and hole. However, in the strong confinement regime, where $a \ll a_B$, the QD energy is expressed as,

$$E_{nl} = E_{gap} + \frac{\hbar^2\chi_{nl}^2}{2\mu a^2} \ (eV), \tag{1.26}$$

where μ is the reduced mass of the electron and hole. Strong confinement corresponds to the situation in which the electron and hole have no bound states corresponding

to a hydrogen-like exciton. However, treating the electron and hole as independent in the strong confinement regime not completely justified, and an analysis of the two-particle Hamiltonian, including kinetic energy, Coulomb potential, and the confinement potential result in a ground state energy (electron-hole pair in the 1s1s state) expressed by:

$$E_{1s1s} = E_g + \frac{\hbar^2\pi^2}{2\mu a^2} - 1.786\frac{e^2}{\epsilon a}\ (eV), \tag{1.27}$$

where the third term reflects the Coulomb interaction.

1.2.1.3 Bandgap Energies Derived from Band Theory

Another approach to calculate bandgap energies in Si-QDs is derived strictly from band theory. Using *ab initio* quantum mechanical calculations, Belyakov *et al.* calculated the bandgap of Si-QDs as a function of radius R to be [73]:

$$\epsilon_g^{(1)}(R) = \sqrt{\epsilon_g^2 + \frac{D_1}{R^2}}\ (eV), \tag{1.28}$$

where D_1 =4.8 eV^2/nm^2, and ϵ_g = 1.17 eV = $\Delta_{\chi\Gamma} + E_{el}^{(sp)} + E_h^{(s)}$ with $\Delta_{\chi\Gamma}$ =1.24 eV and $E_{el}^{(sp)}$and $E_h^{(s)}$ are the lowest energies in the conduction and valence bands, respectively. Equation 1.28 is a refinement to the infinite potential approximation, since it includes the effects of a finite barrier and the effective mass discontinuity at the interface. It predicts a smaller size dependance of the bandgap, as compared to the simple model leading to Equation 1.27.

1.2.1.4 Bandgap Energies Estimated from Experiment

Experimental results from Delerue *et al.* [54] and Ledoux *et al.* [74] suggest that the quantum confinement models described above are approximations that can describe the bandgap energy reasonably well. The experimental data obtained by Delerue fits a power-law with the form:

$$E_{PL}(d) = E_{gap} + \frac{3.73}{d^{1.39}}\ (eV), \tag{1.29}$$

where d is the QD diameter. The experimentally-obtained exponential factor of 1.39

instead of 2 suggests that the effective-mass theory does not provide a completely adequate description of the energy levels in nanocrystallites [54]. The addition of an attractive Coulomb energy of the ground-state electron-hole pair represents a further refinement:

$$E_{PL}(d) = E_{gap} + \frac{3.73}{d^{1.39}} - 3.572\frac{e^2}{\epsilon d}\ (eV). \tag{1.30}$$

(Note: the -3.572$e^2/(\epsilon d)$ term is the same as the term added to Equation 1.27, with $d = a/2$). Inclusion of a lattice parameter could explain why the exponential factor is smaller than expected [74].

The lattice parameter in small crystallites is a function of particle size [75]. Due to the high curvature of the QD surface, the lattice parameter decreases for smaller QD sizes, affecting the peak PL position [75]. Experiments by Sood *et al.* demonstrated that the peak PL wavelength redshifts when pressure is applied to PSi in a diamond anvil cell, with a "proportionality factor" of f =4×10^{-2} eV/GPa [76]. The experimentally obtained change in the lattice parameter of Si-QDs as a function of diameter is given by [74, 75]:

$$\Delta d_{\{111\}} = \frac{0.023}{d} - 0.0064\ (nm), \tag{1.31}$$

where d is the lattice parameter of bulk silicon ($d_{\{111\}}$ =0.3134 nm). The change in the bandgap energy can then be expressed as a function of the compressibility of Si:

$$\Delta E = \frac{f}{\kappa} 3 \frac{\Delta d_{\{111\}}}{d_{\{111\}}}\ (eV), \tag{1.32}$$

where f =4×10^{-2} eV/GPa and κ =0.01 GPa^{-1} is the compressibility of Si, and $\Delta d_{\{111\}}/d_{\{111\}}$ is the change in the lattice parameter. Combining 1.29 with 1.31 and 1.32 gives an empirical equation for the PL energy of Si-QDs:

$$E_{PL} = E_{gap} + \frac{3.73}{d^{1.39}} + \frac{0.881}{d} - 0.245\ (eV), \tag{1.33}$$

which is in good agreement with experimentally determined values of peak PL and Si-QD size given by Delerue [74]. Note, however, that Equation 1.33 does not include the Coulomb correction term, and that it is not suitable for describing large QDs,

since the energy does not approach the bulk value (Fig. 1.6).

To summarize, several models were proposed to explain the recombination energy as a function of size for Si nanocrystallites. Equation 1.27 uses a simple quantum-confinement model to approximate the energy of a Si-QD [69]. Similarly, equation 1.28 derives Si-QD energies with a more thorough treatment and band-theory approximations [73]. Finally, both equations 1.30 and 1.33 incorporate experimental data to generate fitting parameters, taking into account the effective-mass of the electrons [54] and changes in the lattice-parameters of QDs as a function of their size [74]. The calculation of the Si-QD bandgap is no trivial task, and is further complicated when surface-oxides are included.

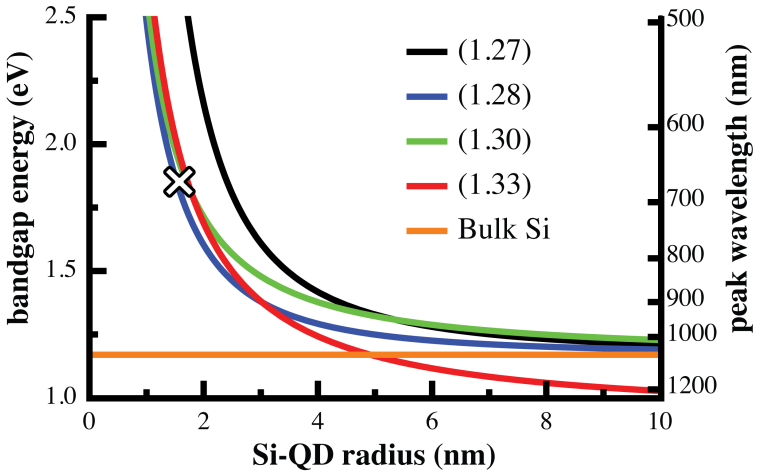

Figure 1.6. Calculated Si-QD bandgap energies and corresponding PL wavelengths as a function of QD size for various theoretical models shown in Eqs. 1.27, 1.28, 1.30, and 1.33. The X denotes experimentally obtained values for the mean Si-QD radius and peak emission energy (~3.2 nm diameter, ~750 nm emission from [77]). This figure illustrates the range of empirical and theoretical calculations in the literature.

1.2.2 The Role of Oxygen

Shortly after the discovery of efficient luminescence from porous silicon [7], several observations suggested that oxides might play a key role in the luminescence spectrum [56–58, 60–62, 68, 78–80]. If thermal oxidation of the QD surface decreases the size of the QD core, a blue-shift in the PL might be expected. However, upon thermal oxidation the opposite behavior was observed: the emission spectrum redshifted [57]. One study proposed that the PL in oxidized samples arises from siloxene compounds

($Si_6O_3H_{6-n}(OH)_n$ with $1 \leq n \leq 6$) on the QD surface, with the peak PL wavelength progressively redshifting with increasing n [56]. However, studies performed using X-ray-induced photoexcitation methods suggested that the luminescence in PSi does not derive from siloxene [78], with some studies suggesting that the PL arises from SiO_2-related structures [60]. Si–O–Si, Si–O–H, and Si–H bonds were then suggested to control the emission spectrum [61]. Exciton confinement in the interfacial layer between the Si-core and the surrounding amorphous silicon-oxide was also suggested as being responsible for the strong PL over unoxidized samples [58].

Wolkin *et al.* [62] proposed a highly-cited model that explained how quantum confinement and surface states could be related. They reported that etched PSi stored in argon had few to no oxide-related features (Si–O–Si, Si–O–H, Si=O) in the infrared spectrum, but that after exposure to air, the peak PL wavelength redshifted and oxide-related features began to appear. These authors suggested that the Si=O double bond was responsible for the localized electron and hole levels that appeared within the bandgap when it had become sufficiently widened by quantum confinement [62]. The Si=O bond was compelling because it could passivate two neighboring dangling bonds at the surface of a Si nanocrystallite, reducing the large compressive stresses on the highly curved surfaces [75]. Accordingly, Wolkin proposed three size-dependent "zones" as follows (Fig. 1.7):

1. In "Zone I" (QDs between 3 and 5 nm in diameter): the Si=O bond energy was calculated to be equal to the Si-QD bandgap energy, so recombination occurs *via* a free electron and a free hole.

2. In "Zone II" (QDs between 1.5 nm and 3 nm in diameter): the Si=O bond traps a free electron in a lower-energy p-orbital on a Si atom. The free hole energy governed by the size dependent QD energy, and thus recombination of the trapped hole occurs with the trapped electron at a lower energy than the quantum confinement model suggests.

3. In "Zone III" (QDs below 1.5 nm in diameter): the electron is trapped in a p-orbital on the Si atom and the hole is trapped in a p-orbital on the O atom. Trapped electron and hole energies are still size dependent, but lower in energy than the quantum confinement model predicts. Recombination occurs when

both an electron and hole are trapped by the same Si–O complex, a so-called "trapped-exciton".

Wolkin's model is compelling in its simplicity and it appeared to describe the observations quite well; there is also experimental evidence that luminescence mechanisms are both size and oxidation dependent. For large Si nanocrystallites ($d \approx$2.9 to 3.4 nm, *i.e.* Zone I) oxidation causes the PL to blue-shift [68], presumably due to a decrease in the Si-core. However, the PL redshifts during oxidation of smaller ($d \approx$2.5 to 2.8 nm, *i.e.* Zone II) Si-QDs after the formation of ∼0.3 monolayers of native oxide, consistent with the formation of an oxygen-related states within the bandgap [68].

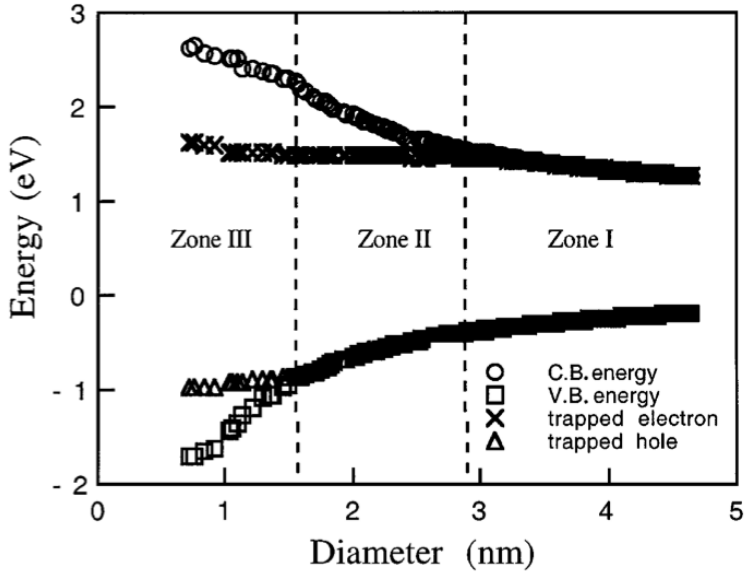

Figure 1.7. PSi bandgap, calculated for a Si-QD with an Si=O surface bond. Zone I, for large PSi crystallites, represents recombination of free excitons. The PL energy increases as the nanocrystallite size decreases, as predicted in the quantum confinement model. In Zone II, an electron can be trapped by a surface state and recombine with a free hole. In Zone III, both electron and hole can be trapped, and recombination occurs *via* a trapped exciton. Figure reproduced from reference [62].

Subsequent experimental evidence indicated that the Si=O double bond is a short-lived transient [79] [81] and is therefore not likely to be the origin of the luminescence. In fact, the Si=O bond interacts with atomic hydrogen (which is likely present around freshly-etched nanocrystallites) to drive the insertion of oxygen and transform Si=O structures into Si–O–Si bonds in a process sometimes called "back-

bonding". Later work showed that other structures related to Si sub-oxides, such as Si–O–Si and Si–O–H conformations, are likely to be present on oxidized Si-QDs and can produce sub-gap radiative centers [67]. In 2000, Garrido *et al.* performed a series of photoluminescence excitation experiments and reported evidence in favor of an SiO_2-related phonon-assisted emission mechanism that accounted for the observed Stokes shift of ∼0.26 eV. Thus, while numerous and sometimes contradictory models have been proposed, surface oxidation does seem to produce radiative sub-gap centers (mainly due to Si–O–Si or Si–O–H bonds) whose effect appears to be size-dependent (as in the original model of Wolkin et al.). Oxide-related phonon emission may also play a role in the recombination process [80].

Although the luminescence from silicon nanocrystallites seems to be governed in large part by the quantum confinement effects in Si-QDs, there is now a wealth of experimental evidence that supports the role of oxygen surface species in photoluminescence [56–58, 60–62, 68, 78–80]. The theory proposed by Wolkin *et al.* [62] is especially attractive but appears to be flawed due to the transient nature of the Si=O double bond. However, other oxide-related structures such as Si-O-Si bridges are stable and may lead to the observed red emission from small QDs [67, 79, 81].

1.2.3 Non-Radiative Recombination

Non-radiative processes in Si-QDs also affect the luminescence spectrum and efficiency. Non-radiative recombination is much faster than radiative processes in indirect-gap semiconductors like Si [54, 82]. When non-radiative recombination is extensive, the luminescence is weak and the measured PL lifetimes are short [54]. The main non-radiative pathway in nanoscale silicon is thought to be a surface dangling bond on a Si atom, known as a P_b center [83]. The P_b center can capture free-carriers and provides a non-radiative recombination channel *via* a multi-phonon process [83]. This lowers the overall PL intensity [52] and can often cause the peak wavelength to blue-shift due to the greater probability (per QD) of finding defects on larger particles [73]. The concentration of defects, such as dangling bonds, is thus a key parameter that influences the emission spectrum and efficiency.

1.2.3.1 Defects in PSi

Electron spin resonance (ESR) (discussed in detail in 2.6.2) is a technique that can be used to measure the concentration of non-radiative P_b centers in nanoscale silicon. The power of this technique arises in part from the lack of paramagnetic species in silicon other than those due to unpaired electrons in unsatisfied chemical bonds (*n.b.*, the ^{29}Si isotope contributes to the hyperfine peaks in ESR spectra, but it is generally not significant since ^{29}Si accounts for less than 5% of naturally occurring silicon). Since the P_b center is an unsatisfied bond on a silicon atom, ESR can be employed to measure the concentration of this species.

The paramagnetic centers in Si-SiO_2 structures were discovered by Nishi in 1971 in samples of oxidized bulk Si [84], and were labelled as P_A, P_B and P_C centers (Table 1.1). These centers are characterized by their "g-factor", formally known as the dimensionless magnetic moment, which relates the total magnetic moment of an unpaired electron to the Bohr magneton (discussed in detail in Section 2.6.2). The P_A and P_B centers appeared when Si was oxidized in a dry oxidizing ambient (low H_2O concentrations), whereas the P_C centers appeared either after rapid cooling from 1000 °C, or after exposing the material to hydrogen gas at 1000 °C for 10 minutes.

The P_A, P_B and P_C centers were distinguished by their ESR signal in relation to the crystal orientation in bulk Si. The ESR signal from the P_A center was isotropic with respect to the applied magnetic field, and was attributed to a trapped electron at a defect site in a surface oxide near the interface [84]. The strength of the ESR response associated with the P_B and P_C centers depends on the angle of the magnetic field with respect to the crystal orientation. The P_B center was attributed to a "trivalent Si which has a non-bonding orbital electron in the Si network" [84]; *i.e.,* a dangling-bond defect on a Si atom at the interface. The P_C center was attributed to a trapped hole at the site of an unpaired electron in the bulk Si [84].

Defect	g-factor
P_A	2.000
P_B	2.000∼2.010
P_C	2.06∼2.07

Table 1.1. Values of the g-factors associated with paramagnetic defects in Si-SiO_2 structures, proposed by Nishi in 1971 [84].

There have been numerous ESR investigations on the structure of PSi (Sec. 2.2). These studies generally concluded that the ESR-active sites are related to dangling bonds or oxygen vacancy defects on the surface of the PSi nanostructure [85–90]. The P_b defect in particular has been extensively studied and is recognized as a dangling-bond defect on a Si atom located on the (111) crystal plane of Si [86,91,92]. Although there is precedent for using the capitalized subscript "B" in P_B, most references from Ref. [91] forward refer to the defect as the lower-case subscripted P_b center.

A model of the P_b defect was proposed by Stirling and Pasquarello [93], in which $Si{\equiv}Si_nO_{3-n}$ defect-type structures were examined (Fig. 1.8). Note: here, use of the symbol '≡' is used to denote three single-bonds, not a triple bond. For n =3, we recover the $^{\bullet}Si{\equiv}Si_3$ trivalent structure of the P_b defect (where $^{\bullet}$ represents the unpaired electron). This structure is attributed to a lattice mismatch between the Si (111) crystal surface and the oxide overlayer, in which sp^3 hybridized orbitals from neighboring oxygen atoms deform the sp^3 hybridized P_b defect through Pauli repulsion (and not through electrostatic interaction). P_b defects also arise on pure, hydrogen terminated surfaces upon the removal of hydrogen atoms, which occurs in freshly etched FS-Si-QDs [94]. Experimentally-measured ESR g-factors associated with the P_b center depend on the local environment and preparation method (Table 2.2).

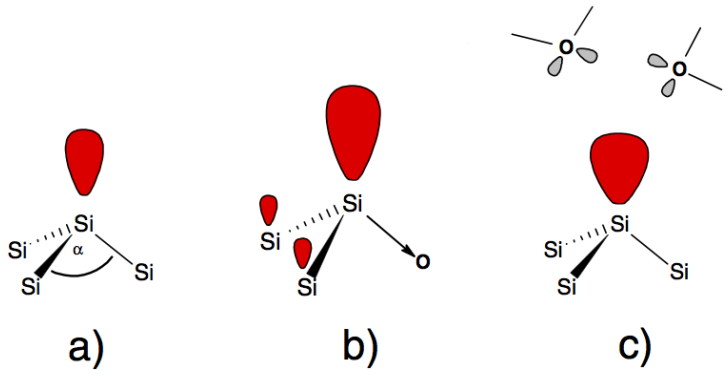

Figure 1.8. Diagram showing a P_b defect on the silicon (111) crystal surface. a) P_b defect extending from the Si (111) surface, b) delocalization of the P_b defect due to a bound oxygen atom, c) Pauli repulsion of the P_b defect due to sp^3 hybridized orbitals from the neighboring oxide. Figure reproduced from reference [93].

At the Si (001) interface there are two additional sub-categories of paramagnetic defects, denoted P_{b0} and P_{b1}. The P_{b0} center is attributed to a Si dangling bond oriented in the (111) direction on the Si(001)/SiO_2 interface, as opposed to the P_b center, which occurs on the Si(111)/SiO_2 interface [88]. Both the P_b and P_{b0} have identical radial symmetry and g-factor values, where the P_{b0} center is only distinguishable *via* its hyperfine interaction with the ^{29}Si nucleus [88, 89]. The P_{b1} center (Fig. 1.9) is distinguished by having lower radial symmetry than the P_b and P_{b0} [88], with the axis of the dangling bond forming an angle of 32° with the interface normal [93]. The P_{b1} defect could be associated with a surface that has been significantly reconstructed, *i.e.,* a disordered or amorphous structure, as in the case of small Si-QDs that have highly curved surfaces [93].

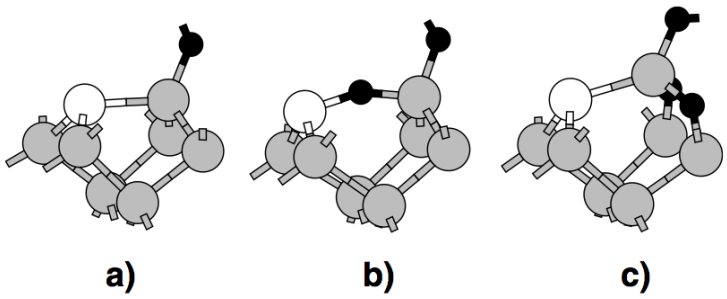

Figure 1.9. Diagram of the proposed P_{b1} defect structures, showing the difference possible geometries of surface oxides to produce the P_{b1} defect. Here grey indicates saturated Si atoms (*i.e.*, all valence electrons satisfied), black indicates oxygen atoms and white indicates the Si atoms with P_{b1} defects. (a) strained dimer model, (b) oxygen bridge model, (c) asymmetrically oxidized dimer model. Figure reproduced from reference [93].

An additional defect type that can be of importance is known as the E' center (g =2.002 [95]). The E' center is a positively charged oxygen vacancy within the SiO_2 framework [95]. Using the terminology defined above, the E' center can be represented as $\cdot Si{\equiv}O_3$, where the defect is associated with a Si atom backbonded to the silica matrix [93]. E' centers can be eliminated in samples annealed at 1100 °C [95]. Unlike the P_b defect, P_a, P_c, and E' defects are thought to occur below the surface of the bulk Si crystal [92].

1.3 Nanoscale Sensors

The luminescence from Si-QDs depends on the QD size, surface composition, and defect concentration. As a result, changes in any of these properties can cause measurable changes in the PL of the Si-QD ensembles, which could be useful for environmental sensing applications. Sensor response could be based on the Si-QD PL intensity, the peak PL wavelength, or the PL lifetime.

Although there is no unanimous definition of a "sensor", there are four general criteria which a sensor should fulfill [96]:

1. A sensor must quantifiably measure changes in the environment and transduce it into a more readily measurable form.

2. A sensor must be selective for a particular environmental variable, so that changes in other environmental variables do not alter the measurement of the quantity of interest.

3. A sensor must be stable over the useful lifetime of the device, producing reliable and reproducible results as the device ages, without influencing the measured property.

4. A sensor should be reversible, to allow the same element to be re-used over many cycles. "Use-once" sensors can be an exception if they are cost-effective.

Sensors based on quantum dots might occupy smaller volumes and consume less power than standard sensors, properties that may also make them less expensive to produce and maintain. This makes nanoscale sensors attractive candidates that may compete with existing sensor technologies.

1.3.1 Quantum Dot Sensors

Interest in the use of semiconductor quantum dots began in the 1990s [97,98], mainly for possible use in biological applications. Biological labeling was one of the first uses for QDs [64], with Bruchez *et al.* using colloidal cadmium-selenide/cadmium-sulfide quantum dots enclosed in silica shells as replacements for conventional fluorophores. Fluorophores are fluorescent compounds that are used in biological imaging to trace fluids, stain biological structures for imaging, or serve as markers for bioreactive agents. Bruchez *et al.* functionalized the II-VI QDs with biotin, allowing researchers to label and image fibroblasts within mouse tissue [64]. Chan and Nie [99] demonstrated that semiconductor QDs could be used for biomolecule detection (proteins, DNA, and viruses), through visible light photoluminescence. They compared QDs to organic dyes, such as rhodamine, and reported that the QDs are 20 times brighter (*i.e.*, 1 CdSe QD is equivalent to 20 rhodamine molecules), 100 times more stable, and have one third the spectral line width [99, 100]. As replacements for biomolecular fluorophores, colloidal quantum dots represented one of the first commercial applications of nanotechnology [101].

Semiconductor QDs also have important benefits over organic dyes: QDs have longer photostable lifetimes, they are tunable over a large range of wavelengths,

and they have chemically functionalizable surfaces [100, 101]. QDs are immediately competitive with existing organic chromophores because their one- and two-photon absorption spectra are two to three times more intense as compared to conventional fluorescent probes [102]. Additionally, QDs have a larger Stokes shift between the absorption and emission spectra, resulting in less "cross-talk" between the excitation and measurement channels than traditional fluorophores (Fig. 1.10). QDs seem only outshone in modern biomedical applications by genetic approaches to designing new organic fluorophores, since biological organisms can incorporate genetic code and generate fluorophores using existing cellular machinery *in vivo* [103], under genetically relevant conditions.

Semiconductor QDs are promising for biomolecular detection and biological imaging [65,104,105]; however, one major issue is their cytotoxicity [106,107]. CdSe QDs with ZnS shells are a popular choice for biomolecular detection [65, 106], in part because the ZnS shell passivates the CdSe surface, protects it from oxidation, and prevents Cd and Se atoms from direct contact with the surrounding environment [65]. Despite these measures, however, there is still evidence that the CdSe core can be oxidized and that Cd and Se can be released into biological samples [65]. Recent studies of CdSe/CdS/ZnS QDs for biomedical imaging in primates claimed that there is no sign of acute toxicity from micelle-encapsulated QDs, however the same study showed that the liver, spleen and kidneys of those animals retained cadmium after 90 days, indicating a low clearance of the QDs from their bodies [107]. Despite attempts to produce biocompatible quantum dots, many jurisdictions heavily restrict *in vivo* research if the QDs contain known toxic substances like cadmium. One possible way to circumvent the dangers presented by II-VI and III-V semiconductor compounds is the use of silicon-based QDs, which have been shown to have low-toxicity in small quantities (>8 μg/ml) in living animals. Although Si-QDs are expected to be less toxic than their group II-IV and III-V counterparts, they have not been widely used owing to challenges in making them water-dispersible and compatible with biological fluids [108].

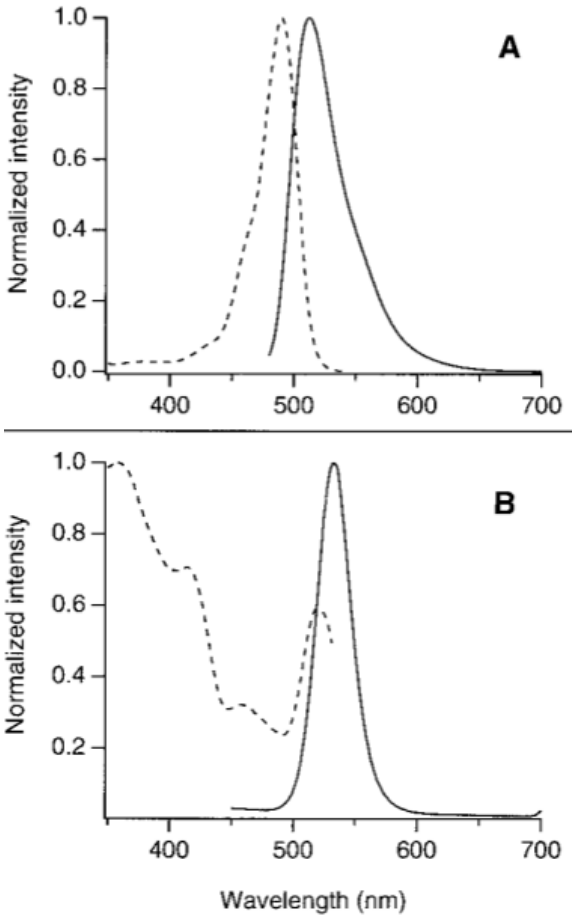

Figure 1.10. Absorption (dashed lines) and photoluminescence (solid lines) spectra of the common fluorophore fluorescein (A) versus CdSe quantum dots in solution (B). The CdSe QDs have a narrower emission spectrum (32 nm compared to 45 nm at the FWHM), and an absorption spectrum that extends to shorter wavelengths than the narrow absorption spectrum of fluorescein. Figure reproduced from reference [64].

1.3.2 Porous Si Sensors

The use of silicon as a sensor began as early as 1963, when Zias described its use as a single-crystal piezoresistive pressure sensor [109]. Porous Si (PSi) was discovered in 1956 by Uhlir at Bell Labs [7], but it wasn't introduced as a sensor until 1990, when Anderson *et al.* developed a capacitance based PSi sensor that detected changes in atmospheric humidity [12]. Other transduction methods in PSi use macroscopic properties like resistivity [21, 23, 24], capacitance [12, 21, 25, 26], optical reflectivity [20, 22], and luminescence [13–19, 27, 28]. These transduction methods are based on chemical interactions that occur on the surface of the PSi network.

PSi-based sensors have many of the benefits of semiconductor QDs, while reducing the toxicity problems associated with group II-IV and III-V QDs [106, 108, 110]. Silicon has a rich molecular chemistry that can extend the utility of Si-based sensors through a process called functionalization [111]. In essence, by binding specific molecules to the Si surface, analyte specificity can be achieved. The sensitivity can be increased significantly as a result of the large surface areas, which can exceed 1200 m^2 per cubic centimeter of nanocrystalline Si.

Analytes of interest for sensing with PSi include toxins, volatile organic compounds, polycyclic aromatic hydrocarbons, explosives, DNA, and proteins. The luminescence spectrum of PSi can be affected by the presence of various gases and liquids, such as benzene (C_6H_6), methanol (CH_3OH), dichloromethane (CH_2Cl_2) and bromine (Br_2) [17]; tetrahydrofuran ($(CH_2)_4O$) [14]; ethanol (C_2H_5OH) [20]; water (H_2O), ethanol (C_2H_5OH) and isopropanol (C_3H_8O) [15]; nitric oxide (NO) and nitrogen dioxide (NO_2) [16]. The transduction method for luminescent PSi is exhibited as a characteristic change in luminescence intensity (for example, it strongly decreases when exposed to ethanol; Fig. 1.11) [27].

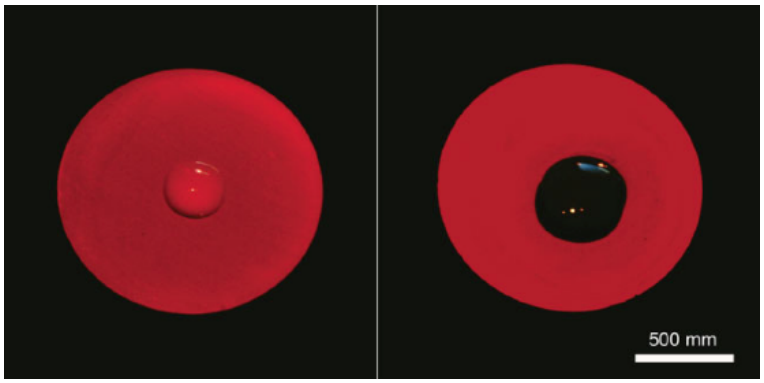

Figure 1.11. Quenching of PSi luminescence due to water (left) and 40% ethanol in water (right). Since the PSi surface has a hydrogen-terminated hydrophobic surface, pure water cannot infiltrate the small PSi pores. However, ethanol can infiltrate the pores and quenches the PSi PL *via* local interactions as discussed in Ref. [17]. Figure reproduced from reference [17].

The biocompatibility of silicon also extends the utility of PSi sensors into the field of biology. Luminescence-based sensing in PSi has found applications in the detection of biomarkers [22], and as biodegradable fluorescent markers for *in vivo* imaging [11],

where the PSi is broken into small free-standing clusters by ultrasonication. One major benefit of silicon nanocrystallite sensors is that they appear to be harmlessly eliminated from the body [11].

1.3.3 Free-Standing Silicon Quantum Dot Sensors

Free-standing silicon quantum dots (FS-Si-QDs) offer potential advantages compared to PSi for sensing applications. Since FS-Si-QDs are, by definition, free-standing, they can be cast onto any surface, curved or otherwise, and potentially used *in situ* as a sensor transducer. Si-QDs surfaces can be functionalized, allowing analytes to selectively interact with the QDs [112–114]. They also have a greater exposed surface area as compared to PSi, since there is no connection between neighboring nanocrystallites. This potentially increases the overall sensitivity of the free-standing Si-QD ensembles.

Many methods of fabricating FS-Si-QDs have been developed [31]. Several involve chemical reactions of silicon compounds. These include solution-based precursor reduction [115–118], and precursor thermolysis and pyrolysis [74, 119–122]. The solution-based methods pioneered by Heath *et al.* in 1992 [115], hold the promise of achieving fine control over particle size and surface chemistry, and can be used to fabricate large amounts of material [31]. Si-QDs produced by this method ranged in diameter from 2 to 9 nm, and Fourier transform infrared spectroscopy (FTIR) studies revealed the presence of Si–O, Si–H, and Si–Cl bonds on the surface. Si-QDs produced by solution-based methods were reported to be "somewhat sensitive to air and moisture" [118]. In 2001, Korgel *et al.* reported the supercritical-fluid synthesis of Si-QDs *via* a thermolysis of diphenylsilane, with mono-dispersed particle diameters of ∼1.5 nm [121]. Decomposition of silane gas (SiH_4) in high-temperature aerosols [119, 120] or silane pyrolysis by CO_2 [122] is another means to produce FS-Si-QDs, but they tend to be in the size range of ∼30-80 nm.

Free-standing Si-QDs can also be produced by physical methods, typically involving the pulverization [123] or sonication [27] of PSi. However, the average domain size using these methods are often much larger than the Si-QD sizes themselves [27, 31, 123], indicating the presence of a remaining silicon-backbone that connects the Si-QDs. While parts of the surface may indeed be chemically and physically

accessible, these fabrication methods thus do not always produce truly free-standing Si-QDs. This method of preparation allowed researchers to investigate the PL of single "grains" of Si-QDs dispersed on substrates from diluted solutions [123]. Simulations of the PL emission from hydrogen-terminated Si-QDs were found to differ substantially from their oxide-terminated counterparts [124], suggesting that "true" free-standing Si-QDs should by hydrogen-terminated. In Ref. [123], the authors note that an efficient method to break the PSi "grains" into sub-micron domains was still a technical challenge.

In this work, FS-Si-QDs are synthesized from a powder of annealed hydrogen silsesquioxane [30, 31], discussed in Section 2.1.1. Liberation of the Si-QDs requires a two-step process: physical pulverization followed by chemical etching to produce free-standing Si-QDs. The resulting Si-QDs have hydrogen-terminated surfaces, can be stored in a non-polar solvent such as toluene, and can be cast onto a variety of surfaces.

1.4 Thesis Organization

This thesis outlines an investigation of free-standing silicon quantum dot photoluminescence under optical irradiation in various vapor environments. Potential applications associated with modifications to the surface structure are discussed. The chapters in this thesis are presented as follows:

- Chapter 2 outlines the experimental methods used to prepare free-standing silicon quantum dots, and their characterization by transmission electron microscopy, photoluminescence spectroscopy, Fourier transform infrared spectroscopy, and electron paramagnetic resonance. The theoretical aspects of these techniques will be discussed as appropriate.

- Chapter 3 discusses the observed changes in FS-Si-QD photoluminescence when the particles are exposed to laser irradiation at different wavelengths, and examines the Fourier transform infrared absorption spectrum. This work was originally published in the Journal of Luminescence [125].

- Chapter 4 discusses the effect of vapors of ethanol and water on the observed

changes in FS-Si-QD photoluminescence, and uses Fourier transform infrared spectroscopy to describe the chemical changes that the Si-QDs undergo during optical irradiation. This work was originally published in Sensor Letters [126].

- Chapter 5 investigates the QD surface structure changes during laser irradiation, using a combination of Fourier transform infrared spectroscopy and electron spin resonance. In this work, a model for the oxidation of the Si-QD surface was proposed. This work was originally published in Chemistry of Materials [77].

- The conclusion summarizes the work done and suggest promising areas of future study for FS-Si-QDs and their function as sensors.

- Appendix A discusses the application of FS-Si-QDs as the transducing element in a fiber-coupled sensor. In this work, a sensor capable of detecting ethanol and water in a pure oxygen environment was demonstrated [127]. This work was published in Sensors and Actuators B: Chemical.

- Appendix B provides samples of Mathematica code used for analysis of the photoluminescence, lifetime, Fourier transform infrared spectroscopy, and electron spin resonance data.

Chapter 2

Experimental Methods

In this section, the methods used to fabricate and characterize free-standing silicon quantum dots will be described. The procedures and methods used will be discussed in detail in order to facilitate reproduction of the results in this work. Many of the methods were developed and built "in-house", so a more detailed review is provided in order to further explain the methodology discussed in the three chapters that follow.

2.1 Synthesis

2.1.1 Free-Standing Silicon Quantum Dot Preparation

Free-standing Si-QDs were prepared using a fast-etching variant of the synthesis method developed by Hessel *et al.* in Ref. [30]. This method employs a molecular precursor called hydrogen silsesquioxane (HSQ). HSQ has the chemical formula $H_8Si_8O_{12}$ and is thought to form a cage-like molecule with silicon atoms on the corners (Fig. 2.1). HSQ dissolved in methyl isobutyl ketone (MIBK) is typically sold under the trade name FOX-15 as a spin-on negative resist made by Dow Corning Corporation (Midland, MI). However the HSQ used in the present work was from a powdered stock of pure HSQ provided to the Veinot lab by Dow Corning, under the serial number 9-5101. HSQ can be used to form gram-scale quantities of Si-QDs by processing the powder at 1100 °C; the high-temperature collapses the cage structure and phase separates the resulting composite into a mixture of silicon particles within

a silicon oxide matrix [31].

In this work, the QDs were synthesized by annealing ∼250 mg of HSQ powder at 1100 °C for one hour, in an atmosphere of 95% nitrogen and 5% hydrogen. The heating and cooling were done in stages, ramping from room temperature to 1100 °C in ∼60 minutes (ramp rate of 18 °C per minute), then dwelling at 1100 °C for an additional 60 minutes, and finally cooling back to room temperature overnight. The hydrogen-containing atmosphere was selected in order to passivate defects on the surface of the resulting Si-QDs [128]. After annealing the powder became reddish-brown in color; it was then mechanically pulverized using a mortar and pestle or wrist-action shaker until the resulting powder turned slightly orange. At this point, the sample consisted of small, sub-millimeter grains of silicon oxide with embedded Si-QDs .

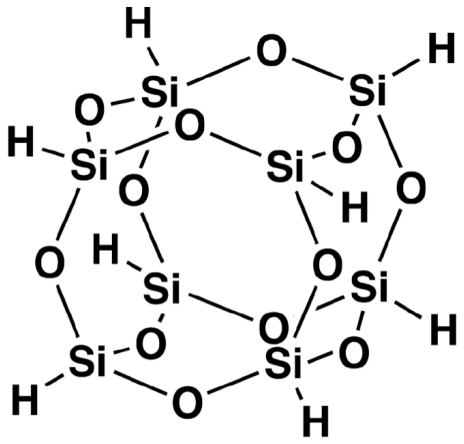

Figure 2.1. Diagram of the hydrogen silsesquioxane molecule. HSQ has a silicon-oxygen cage structure with a silicon atom at the vertices of the cube and oxygen atoms occupying the edges. Figure modified from reference [31].

An etching procedure using hydrofluoric acid (HF[1]), hydrochloric acid (HCl), and ethanol (EtOH or C_2H_6O) was used to free the Si-QDs from the silica matrix. Briefly, approximately 250 mg (weighed using a digital scale) of the annealed and pulverized powder was mixed with a solution of 0.2 mL HCl (36.5% aqueous HCl)

[1]WARNING: HF is an acute poison! Contact exposure may cause deep, initially painless burns and ensuing tissue death. HF interferes with body calcium metabolism, and may cause systemic toxicity leading to cardiac arrest and death. Proper training in procedures, use of safety equipment, and use of antidotes was undertaken prior to handling HF, and the etching procedure was supervised by trained professionals.

and 7.5 mL HF (49% aqueous HF) in a teflon beaker. The solution was mixed for 10 minutes using a magnetic stir plate at its lowest setting. After 10 minutes had elapsed, 5.0 mL of ethanol (95% aqueous EtOH) was added to the solution, while the stirring process continued for an additional 5 minutes. This etching procedure dissolves the silica matrix, and ensures good passivation of the QD surfaces [31]. This proccess results in hydrogen-terminated FS-Si-QDs suspended in the $HCl/HF/H_2O$ solution [30].

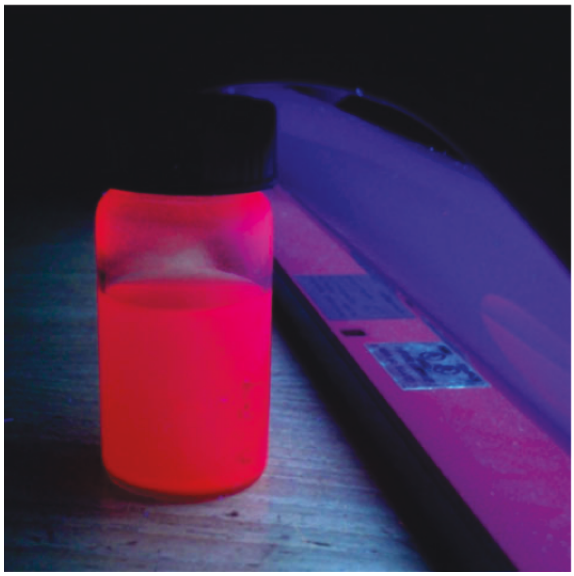

Figure 2.2. The FS-Si-QD/toluene suspension. FS-Si-QDs are suspended in toluene after a successful etch. The PL is being excited by a UV lamp.

To extract the FS-Si-QDs from the etching mixture, 30 mL of toluene was added to the solution while the magnetic stir plate continued to agitate the mixture. The Si-QDs are hydrophobic due to their hydrogen-terminated surface, and thus are easily suspended into non-polar solvents such as toluene. The addition of toluene captures the Si-QDs, and, after stopping the magnetic stir plate, an immiscible toluene layer carrying the Si-QDs formed on top of the acid solution. This FS-Si-QD/toluene suspension (Fig. 2.2) was extracted with a Pasteur pipette, transferred into a new glass vial, and sealed in an argon filled glove-box to minimize QD oxidation.

2.1.2 Sample Preparation

Experiments using the FS-Si-QDs required them to be removed from the toluene suspension and dispersed onto a flat wafer. To start with, the FS-Si-QD/toluene suspension was removed from the argon glove box and transported to the experimental setup. The Si-QDs would precipitate to the bottom of the vial after several hours, so the solution had to be shaken to re-suspend them. A standard glass-pipette was then used to place a few drops of the FS-Si-QD/toluene suspension onto a wafer. Typically, a 1 cm $\times$ 1 cm Si wafer (for PL experiments), a 1-cm-diameter quartz wafer (PL and transmitted light) or a 1 cm diameter KBr plate (for Fourier transform infrared spectroscopy experiments), was coated with 1 to 10 drops from the glass pipette. To evaporate the toluene, dry nitrogen was blown across the wafer surface. This "blow-drying" technique formed a more uniform Si-QD coating, compared to allowing the toluene to simply evaporate in ambient air. Even so, there was some amount of fine-scale agglomeration that could not be avoided (Fig. 2.3).

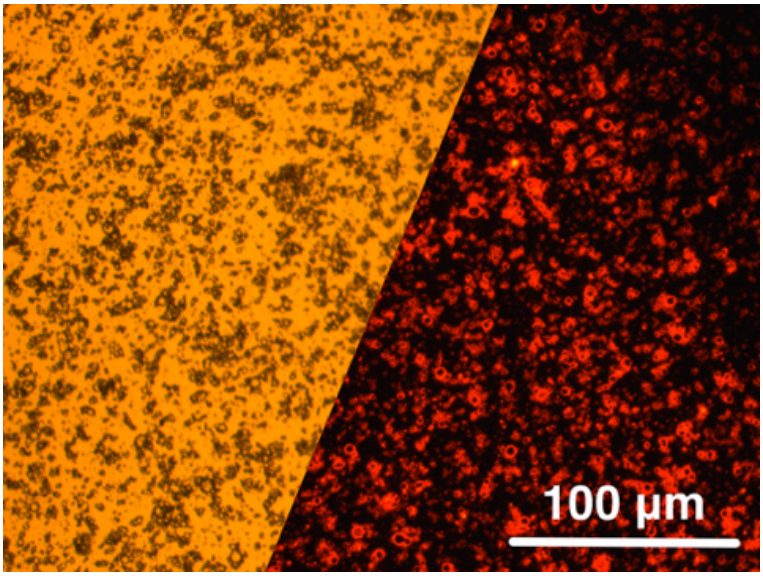

Figure 2.3. FS-Si-QDs on a silicon wafer seen in transmitted visible light (left) and under laser irradiation (right). A 550-nm long-pass filter is in place for both images, giving the visible light an orange hue. In the transmitted light image, the QDs appear as dark "clumps" up to a few microns in size; whereas in the PL image they appear as red "glowing" regions.

To deposit the FS-Si-QDs on non-planar surfaces, different methods were em-

ployed. In the case of the optical fibers, the tip of the fiber was first cleaned with methanol, then cleaved at the end to expose a clean and relatively flat surface. The FS-Si-QD/toluene suspension was concentrated by blowing dry nitrogen into the vial to evaporate a fraction (∼90%) of the toluene. The fiber was then briefly (˜1 s) dipped into the concentrated suspension. After removing the fiber from the suspension, the toluene quickly evaporated, leaving Si-QDs on the end facet and the sides of the fiber. For the electron spin resonance studies, samples needed to be prepared inside a standard NMR tube. To do this, an NMR tube was simply filled with the FS-Si-QD/toluene suspension to a height of several cm. A Schlenk line vacuum system was then used to rapidly evaporate the toluene, leaving behind several tens of milligrams of powder at the bottom of the tube (the powder can be weighed by re-dissolving the FS-Si-QDs from a control sample back out of the NMR tube and allowing the solvent to evaporate on a weighing surface).

2.2 Physical Characterization

Transmission electron microscopy (TEM), high-resolution transmission electron microscopy (HRTEM), and scanning electron microscopy (SEM) were performed in order to characterize the microstructure of the samples. These techniques were used to verify the material composition of the FS-Si-QDs (TEM/HRTEM), elucidate their physical microstructure (TEM/SEM), and image QD-coated fibers and flat wafers (SEM).

2.2.1 Transmission Electron Microscopy

Samples were prepared for TEM by drop-casting the FS-Si-QD/toluene suspension onto a "home-grown" 16-nm-thick carbon film, suspended on a 400-mesh copper grid and allowing the toluene to evaporate. Bright field imaging was used to observe the size and distribution of the Si-QDs. Electron diffraction, where the back focal plane of the magnetic lens system is placed on the CCD sensor, was used to confirm the presence of silicon nanocrystals (and only silicon). Both the bright-field imaging and electron diffraction were performed using a JEOL 2010 TEM with a LaB_6 filament, operating at 200 keV (Fig. 2.4). TEM was performed with the assistance of Shalon

McFarlane.

Figure 2.4. The JEOL 2010 transmission electron microscope with a LaB_6 filament operated at 200 kV used to generate TEM images of the FS-Si-QDs.

2.2.2 High-Resolution Transmission Electron Microscopy

High-resolution transmission electron microscopy (HRTEM) and energy-filtered scanning transmission electron microscopy (EFSTEM) were performed using a Hitachi HF 3300 cold-field emission STEM, or a JEOL field emission 2200FS TEM, both equipped with an Ω-filter. Electron energy loss spectroscopy (EELS) imaging was accomplished by centering an Ω-filter slit at an energy loss of 99 eV (slit width from 4 to 10 eV), corresponding to the silicon L-3,2 edge. In EFSTEM images, the FS-Si-QDs appear bright against a dark background. These imaging techniques were performed by Xiongyao Wang at the National Institute for Nanotechnology.

2.2.3 Scanning Electron Microscopy

A scanning electron microscope (SEM) was employed to characterize the microstructure of the FS-Si-QDs on the end of an optical fiber. Fibers were mounted on a SEM stage using standard double-sided carbon adhesive, with approximately 2 mm of the optical fiber protruding from the side of the SEM mount. SEM samples were then transported to the SEM facility at the Department of Earth and Atmospheric

Sciences. Prior to imaging, the samples received a thin, conductive coating of gold, which was deposited using a Xenosput XE200. Imaging was accomplished with a Zeiss EVO MA 15 SEM operated in secondary electron mode. SEM was performed by Shalon McFarlane under the supervision of George Braybrook in the Department of Earth and Atmospheric Sciences.

2.3 Photoluminescence Spectroscopy

2.3.1 Collecting PL Spectra

Short-wavelength laser irradiation was used to excite the FS-Si-QD luminescence. The laser most commonly used as an excitation source was the Arctic Spyder III sold by Wicked Lasers. It has a wavelength of 445 nm and a maximum output power of ∼1 W. A HeCd laser with an output wavelength of 325 nm and output power of ∼10 mW, as well as an Ar-ion laser with wavelengths 457 nm, 514 nm, 568 nm, and 647 nm (power selectable up to a few hundred mW) were also used in various experiments. The PL from the Si-QDs was collected by an optical fiber, passed through a long-pass filter in order to remove the scattered light from the excitation source, and fed into an Ocean Optics USB2000 miniature spectrometer.

The spectral efficiency of the spectrometer was calibrated using an LS1 blackbody radiator, also from Ocean Optics. This unit has a color temperature of 3100 K. Calibration required two sets of data to be imported into the SpectraSuite software package: a bright spectrum, supplied by the LS1 blackbody radiator, and a dark spectrum, taken with the excitation laser and calibration lamp turned off. The bright and dark spectra are needed to calibrate the spectrometer spectral efficiency and background. The calibration process is quite simple and is given by the following formula

$$I(\lambda) = B_{3100\ K}(\lambda) \cdot \frac{I_S(\lambda) - I_B(\lambda)}{I_{BB}(\lambda) - I_B(\lambda)}. \tag{2.1}$$

Here, $I(\lambda)$ is the calibrated spectral intensity, $B_{3100\ K}(\lambda)$ is Planck's law for the known color temperature (3100 K), $I_S(\lambda)$ is the raw luminescence intensity from the sample, I_{BB} is the raw intensity of the LS1 blackbody source (the "bright"),

and $I_B(\lambda)$ is the background intensity (the "dark"). SpectraSuite handles this entire process internally, displaying the processed spectrum as a graph onscreen. Wavelength calibration was not needed, as the spectrometer comes with its own internal calibration file and the internal components are all fixed.

The integration time was chosen to provide a sufficient signal-to-noise ratio, without saturating the spectrometer. For dimmer samples, the integration time could be as long as one minute; whereas brighter ones could require integration times as short as 100 ms. In order to investigate changes in the PL spectrum over the duration of an experiment, the PL spectra were auto-saved at regular intervals, henceforth called a "time-series". SpectraSuite was set up to automatically save a time-series by collecting spectrum of a fixed integration time, at a certain "save frequency". For example, a bright sample might use an integration time of 100 ms, with one spectrum being saved every five seconds (the "save-frequency") over the course of a 1-hour experiment. The save frequency was selected in order to appropriately capture any spectral changes that occurred during the experiment. The resulting "time-series" data could then be analyzed, as discussed below.

Note: Photoactivation

During routine PL collection performed early on in this project, a clear increase in the FS-Si-QD PL intensity was frequently observed while the laser light was incident on the sample. The term "photoactivation" (PA) was used to describe this effect (*i.e.*, the PL getting brighter over the course of an experiment). This was surprising and opposite to the normally observed photobleaching that is common in nanoscale silicon [15, 27, 90, 129, 130]. Photoactivation of Si-QDs is one of the main phenomena studied in this thesis and forms the basis of the sensing mechanism. Time-series PL measurements, as described above, were performed in order to capture the PA process. It also motivated a series of PL experiments to be conducted in controlled gas environments, as discussed in Section 2.5. The physical and chemical changes that occur during the photoactivation process will be explored in Chapters 3, 4, and 5.

Short-wavelength irradiation was chosen to excite the Si-QD PL, however, irradi-

ation was also responsible for chemical changes to the silica surfaces. These changes are caused when the reactivity of the Si-QD surface (*i.e.* the Si-H bonds) is altered due to a light-induced change of the electron density [17]. In particular, the rate of Si-H bond dissociation is inversely proportional to the irradiation wavelength [131]. This photochemical effect has been used to introduce defects into Si-QDs via removal of the hydrogen species under UV irradiation [132]. This effect has also been employed to initiate "exciton-mediated" Si-QD etching [133].

2.3.2 Luminescence Spectral Analysis

A typical PL time-series could result in hundreds of spectra being collected over the course of an hour or more. In order to process the data, the raw spectra were saved by SpectraSuite as text files that were afterwards imported into Mathematica for analysis. The basic process was as follows. First, the spectral data was imported from the text files; these included a timestamp, the integration time, and columns for wavelength and intensity. The imported datasets were imported into multidimensional matrices in Mathematica. Each individual spectrum in the time-series was normalized according to the integration time. This was necessary because some samples required a change of integration time during a single time-series (*i.e.*, sometimes the photoactivation process was so strong that an initially dim sample could begin to saturate the detector, necessitating a decrease in the integration time). Timestamps were converted to measure the time since the beginning of the experiment. Finally, a numerical bandpass filter was applied in order to select only the wavelength range over which PL was significant (*i.e.*, the noisy, negligible-intensity "edges" of the spectra were discarded in order to save processing time). The Mathematica code for PL time-series analysis can be reviewed in Appendix B.

To analyze the imported data, the spectral intensities were numerically integrated to convert them into a form recognized by the fitting function. Prior to fitting, best guesses for the integrated intensity, peak wavelength, and line-width of each spectra were calculated and used for the initial values to seed the fitting function. Fitting (*i.e.*, parametric waveform analysis) used a skew-normal distribution [134]

$$A * e^{-Log[2]*(Log[1+(2b*(x-\mu))/\sigma]*\frac{1}{b^2}}, \tag{2.2}$$

in which μ is the mean, σ is the standard deviation, b is a skewing factor, and A represents the area under the curve. A skew-normal function was necessary, as many of the spectra were clearly asymmetric and could therefore not be well fit with standard Gaussian or Lorentzian functions. An example is shown in Figure 2.5 (b), where we clearly observe that the skew-normal distribution gives the best fit. One should note, however, that no special physical meaning is assigned to the choice of a skew-normal; the decision is based on the simple practicality that the spectrum needed to be "well fit" in order to produce a reliable analysis. Finally, time-series plots were generated using a rainbow colorspace that colored each spectrum according to its position along the time-series. The initial spectrum of a time-series was colored blue, and subsequent spectra varied continuously through the colors of the rainbow to red, representing the final spectrum. An example time series spectrum (Fig. 2.5(a)) and the corresponding PL peak position (Fig. 2.5 (d)) is shown in order to illustrate the results that could be produced with this method. The figure shows how the peak PL wavelength varied during a single time-series experiment.

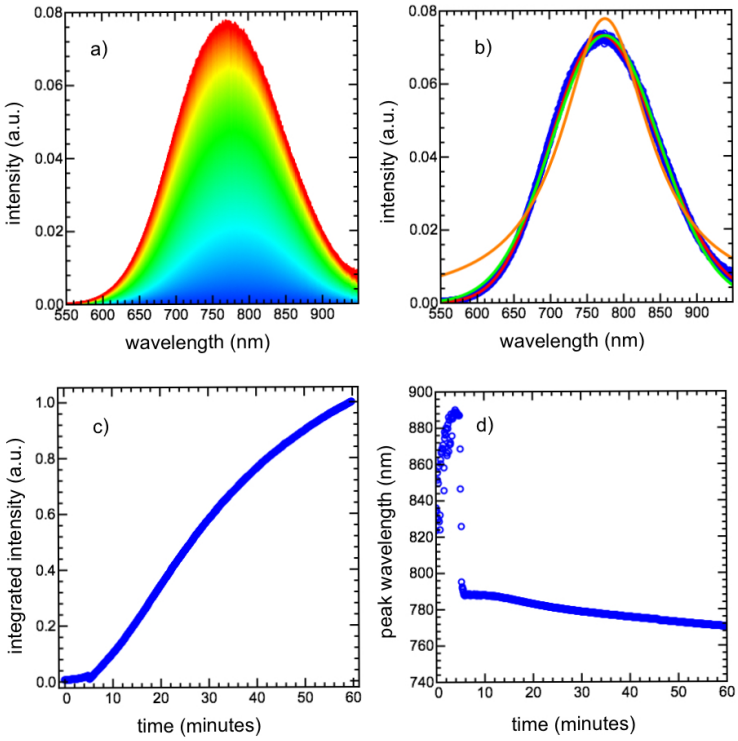

Figure 2.5. Analysis of PL time-series data: a) Spectral data from a 60-minute time-series, shown here with the initial spectrum in blue and the final spectrum in red. b) Spectrum 645 (out of 720 total spectra) is shown (blue), with best fits using a skew-normal function (red), a Gaussian function (green), or a Lorentzian function (orange). c) Integrated intensity of the FS-Si-QD PL during the time-series as a function of time. d) Peak wavelength of the time-series spectra plotted as a function of time.

2.4 Photoluminescence Lifetime Spectroscopy

2.4.1 Lifetime Data Collection

Lifetime spectroscopy was performed by modulating the excitation laser light and using a photon-counting photomultiplier tube (PMT) instead of a spectrometer. For this work, an argon ion laser (using a wavelength of 476 nm at a power of ∼5 mW to 2 W) was modulated by using an acousto-optic modulator (AOM) interfaced to a function generator. The function generator produced a 5-volt square-wave signal (50% duty cycle) at a frequency of 500 Hz. The PL was collected by an optical-fiber as before, sent through a 550-nm long-pass filter to eliminate scattered laser light, and was then incident on a Hamamatsu H7422P-50 photomultiplier interfaced to a

Becker-Hickl PMS-400A digital multiscaler card. The PMS software was typically configured to collect the PL intensity in 1 μs bins, corresponding to 4000 bins for the 4 μs cycle (2 μs with the laser pumping the QDs, 2 μs with the laser off). Typically, 50,000 "sweeps", or cycles, were accumulated in order to achieve a good signal-to-noise ratio. In order to measure how the lifetime evolved during the photoactivation process, a two-laser setup was used: an intense 445-nm diode laser was used to periodically photoactivate the sample, and a weak, modulated 476-nm Ar laser was used to measure the lifetime.

2.4.2 Lifetime Data Analysis

The PL lifetime data was saved as text files for importing into Mathematica. The data was fit using a stretched exponential function, as is commonly done for nanocrystalline silicon [27, 61, 62, 66, 90]. This function represents a distribution of lifetimes that can be caused by size and defect distributions, as well as carrier hopping between QDs [73, 135, 136]. The stretched-exponential intensity decay is given by

$$I(t) = I_0 * e^{-(t/\tau)^{\beta}} + C, \tag{2.3}$$

where I_0 is the initial intensity, τ is the effective lifetime, β is a stretching parameter that can vary between 0 and 1 (where smaller values indicate broader range of lifetime distributions) [136], and C is a DC offset. To facilitate fitting over a wide range of lifetimes, initial guesses to seed the fit were generated for τ by first finding the $1/e$ time directly from the data and using that value as the initial guess for τ. Similar to the PL time-series plots, a time-series of lifetimes (*i.e.*, during the photoactivation process) could then be generated, using the blue (initial lifetime) to red (final lifetime) colormap.

2.5 Controlled Gas Experiments

A gas handling system was built in order to conduct PL experiments under controlled environmental conditions. The idea was to have a setup in which the QDs could be exposed to a desired "carrier" gas (*e.g.,* O_2, N_2, Ar) and analyte vapor (*e.g.,* H_2O, ethanol, long-chain organics, dinitrotoluene, nitrobenzene, *etc.*). The

controlled gas environment consisted of a gas-mixing manifold connected to a sealed sample chamber.

The manifold was built to mix a carrier gas with analyte vapors at desired concentrations. The manifold consisted of two "branches", a "dry" line and a "bubbler" line (Fig. 2.6). The carrier gas first passed through a flow meter to measure the total flow, which was then split between the two main "branches" of the apparatus. A second flow meter was employed on the "dry" line, and a third one was placed on the "bubbler" line. In the "bubbler" line of the manifold, the carrier gas passed through a liquid bubbler, which produces a saturated vapor that is then carried down the bubbler line. Control over the flow rate in each branch allowed the concentration of the analyte vapor to be adjusted to the desired value. The gas in both branches was then merged into a single flow before being input into the sample chamber. Typical carrier gas flow rates were on the order of 8 L/minute.

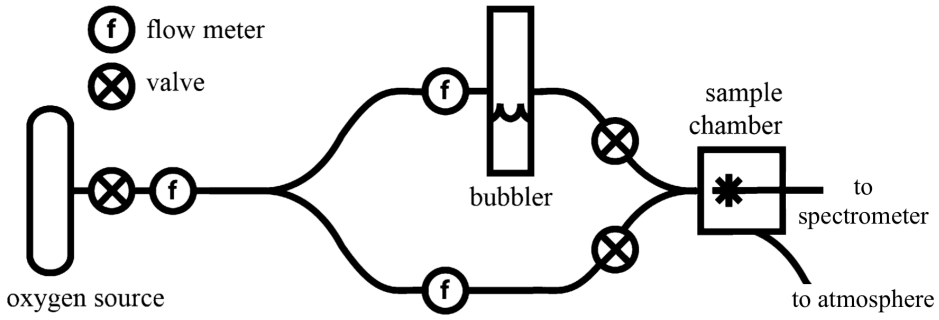

Figure 2.6. Diagram of the gas mixing manifold. Here, an oxygen source is connected to a flow meter, before branching between the "bubbler" and "dry-line". Manipulation of the flow meters allows control over vapor concentration that enters the sample chamber.

The gas manifold fed into a customized aluminum chamber, consisting of an aluminum box with an O-ring-sealed lid, a gas inlet and outlet, an SMA optical-fiber port, and a quartz window. The sample was held in a vertical slot that was machined into a block of aluminum designed to fit inside the box. A 1-inch quartz window was epoxied into a chamfered hole machined into the lid of the sample chamber, through which the diode laser was directed toward the sample. The gas inlet and outlet were 1/4-inch Swagelok ports threaded directly into the aluminum box on either side of the quartz window, which directed the mixed gases over the sample. The optical-

fiber port was threaded directly into the aluminum box opposite the sample holder, allowing the PL to be collected from the sample. Prior to experimentation, the sample was inserted into the chamber, and the mixed gases were flowed for several minutes to expunge the ambient air. The entire apparatus could fit onto a 1 foot square optical breadboard (Fig. 2.7), although an equally functional setup could be made on reduced scales.

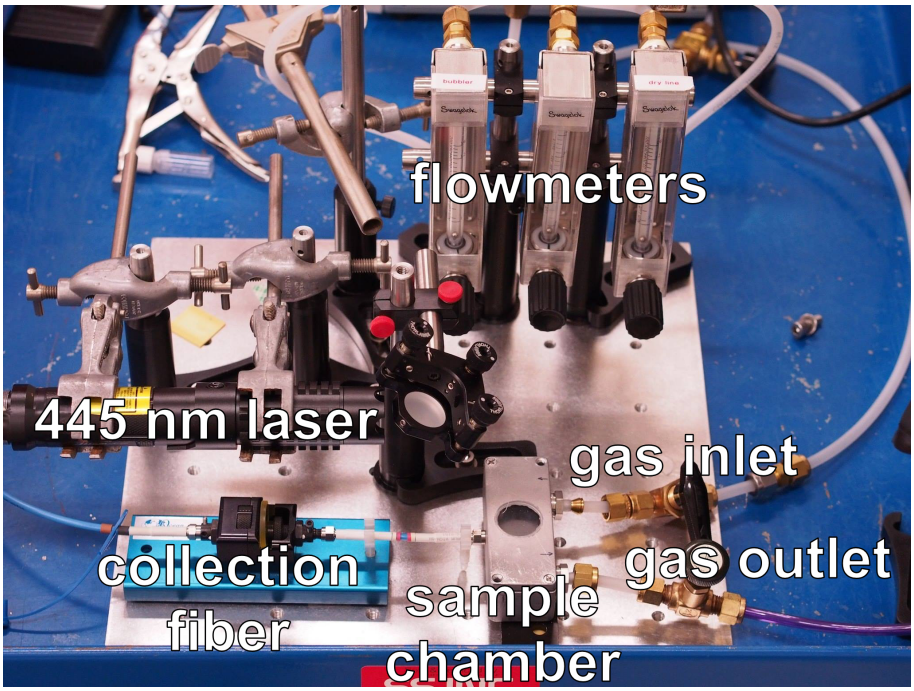

Figure 2.7. Photo of the gas mixing manifold and free-space irradiation setup. Light from the laser is reflected from the mirror (center) into the sample chamber through the quartz window. Gasses from the mixing manifold are sent to the bubbler (not shown) and dry lines, where they combine before entering the sample chamber.

In most of the experiments, a free-space laser was employed both as the irradiation source (for photoactivation) and to excite the FS-Si-QD PL. The laser most commonly used in these experiments was the 445 nm diode laser described earlier (Sec. 2.4.1). Prior to entering the sample chamber, the laser light was sent through a diverging lens to expand the beam so that the sample received a more uniform irradiation. However, the FTIR or ESR experiments required a different procedure, since there was no way to excite the samples *in-situ*. For FTIR studies, the QDs were deposited on KBr plates, which were periodically removed from the controlled

gas environment for FTIR analysis (Sec. 2.6.1). After collecting an FTIR spectrum, the KBr plate was resealed in the sample chamber, and the photoactivation process proceeded. For ESR studies, an NMR tube and glass pipette were used in place of the aluminum chamber. The NMR tubes were interfaced directly with the gas mixing manifold by connecting the gas outlet of the manifold to the wide end of a glass pipette. The narrow end of the pipette was inserted into the NMR tube, delivering controlled gasses directly to the sample. The outside diameter of the glass pipette and the inside diameter of the NMR tube could be tightly fit due to the taper of the pipette, producing what was hoped to be a reasonable seal for the gas flow (some leakage of gas flowing from inside the tube would be irrelevant in any case). Laser irradiation was done through the transparent sidewalls of the NMR tubes, which were rotated to produce a more uniform irradiation of the entire sample.

In the co-authored work (Appendix A), a coupled optical fiber (50% coupling at 800 nm; Fig. 2.8) was employed to irradiate the FS-Si-QDs that were located on the tip of an optical fiber. Here, the 445-nm laser light was focussed into one arm of a 2×2 fiber coupler by using a microscope objective mounted on a micropositioning stage. The coupler was approximately 10% efficient at 445 nm, so 90% of the laser light propagates down the input fiber, whose opposite end was coated with quantum dots. This end of the fiber was threaded into the SMA port in the aluminum box using a NBG-02 bare fiber adapter "bullet", for exposure to controlled gas environments (the idea being to test the ability of the QDs to act as the active element of a fiber-optic gas sensor). The remaining ∼10% transmitted laser power was coupled to the opposite fiber, which was connected to a THORLABS PM100A power meter and SC150C photodiode to monitor the stability of the laser. A fraction of the Si-QD PL travels back up the fiber and is coupled (∼50%) into the "spectrometer" arm.

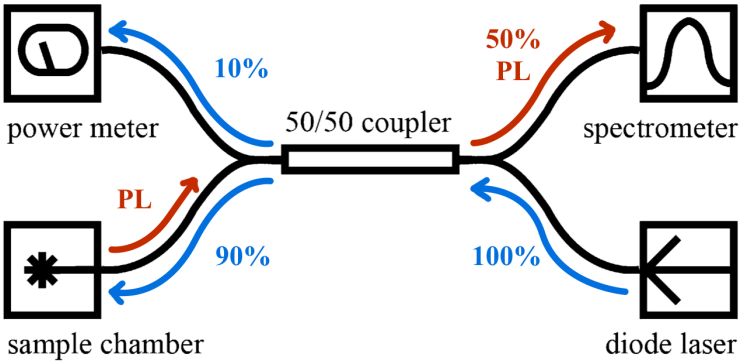

Figure 2.8. Diagram of the fiber-coupler setup used in Appendix A. The directions of the pump light and PL are illustrated by the blue and red arrows.

2.6 Chemical Characterization

Fourier transform infrared spectroscopy (FTIR) and electron spin resonance (ESR) were performed to characterize the chemical changes in the FS-Si-QDs during the PA process. FTIR was used to monitor the formation of various chemical surface bonds, whereas ESR investigated electronic defects in FS-Si-QDs. Since these techniques were used extensively in this thesis, a more detailed description of the methods as applied to Si-QDs will be provided.

2.6.1 Fourier Transform Infrared Spectroscopy

Fourier transform infrared spectroscopy is the study of the interaction between infrared light and matter. In FTIR experiments, the wavelength of light is (unfortunately, in this author's opinion), still measured in *wavenumbers*, given as a reciprocal of the wavelength in inverse centimeters (cm^{-1}). The mid-infrared frequency range from 4000 to 400 cm^{-1} is commonly used for FTIR, which corresponds to infrared photon energies from 0.05 to 0.50 eV (corresponding to wavelengths from 24.8 μm to 2.48 μm). This energy range is characteristic of many interatomic bond vibrations [137]. Since FTIR covers the range of energies associated with vibrational modes, absorption of the incident IR radiation occurs at wavenumbers determined by the nature of the interatomic bonds. Analysis of the FTIR absorption spectrum can therefore be used to identify the chemical bonds in a compound by correlation

with known values for FTIR resonances. Typical wavenumbers associated with interatomic bond vibrations in samples consisting of silicon, oxygen and hydrogen are listed in Table 2.1.

FTIR analyses were performed using a Thermo Nicolet Nic-Plan FTIR attached to a Magna 750 main bench microscope with a wavenumber resolution of 4 cm^{-1}, over a range from 4000 to 650 cm^{-1}. This covers the wavelength range of all of the vibrational modes listed in Table 2.1. The QDs were deposited onto KBr plates, as mentioned earlier, in order to avoid complications from absorptions in the wafer itself (KBr is transparent to infrared photons in the wavelength range investigated, and is commonly used as a substrate in FTIR studies). Thirty-two scans per spectrum were averaged in order to increase the signal-to-noise ratio, taking approximately 1 minute to average all 32 scans. FTIR was performed under the supervision of Wayne Moffat and Brett Mason in the Department of Chemistry.

During the collection period, the samples were unavoidably exposed to ambient atmosphere when transferring to and from the sample chamber, and during collection of the FTIR spectra. Therefore, a control sample was also prepared in order to monitor any changes that occurred in the PL due to atmospheric oxidation as the analysis proceeded. The control sample was not photoactivated, instead, the PL was simply measured over periodic intervals in order to measure whether the exposure to ambient conditions over the duration of the experiment could affect the PL. By comparing the initial and final PL of the control sample, it was determined that exposure to the atmosphere caused negligible changes over the time periods needed for transport and data collection.

Material	Infrared Mode Assignment	FTIR Resonance (cm^{-1})	Reference
Bulk Silicon Si(111)-7x7	Si–H stretch	2090	Gupta (1991) [138]
	Si-O-H stretch	3680	
	Si-O-Si stretch	900 - 1100	
	Si–H stretching in $HSi–Si_{3-n}O_n$n for n=1, 2, and 3	2119, 2716, 2268	
Amorphous silicon	Si–H wagging	640	Zacharias* (1996) [139]
	Coupled mode of a-Si:H:O	780	
FS-Si-QDs	Si–H_n scissoring n = 1, 2, and 3	910	Kelly (2010) [112], Rodriguez (2012) [133]
Amorphous silicon	Si–O–Si asymmetric stretching in an a-Si:H network	1055	Zacharias* (1996) [139]
FS-Si-QDs	Si–O–Si bonds	1000 - 1250	Kortshagen (2011) [140]
Amorphous silicon	Si–O stretching in low-temperature plasma enhanced CVD	1055	Zacharias* (1996) [139]
Si-QDs	Si–O–Si stretching	1074	Liptak (2009) [94]
Amorphous silicon	Si–O stretching in thermally grown SiO_2	1080	Zacharias* (1996) [139]
Plasma synthesized FS-Si-QDs	Si–O–Si stretching	1092	Liptak (2009) [94]
FS-Si-QDs	Si–O–Si stretching	1100	Kelly (2010) [112]
Si-QDs	Si-CH_2 scissoring and stretching	1461, 1261	Wang (2012) [141]
Amorphous silicon	Si–H stretching in dense a-Si:H	2000	Zacharias* (1996) [139]
Plasma synthesized FS-Si-QDs	Si–H stretching in Si–H	2085	Liptak (2009) [94]
	Si–H stretching in Si–H_2	2110	
	Si–H stretching in Si–H_3	2136	
	Si–O–Si stretching in O_2SiH_2	2175	
FS-Si-QDs	Si–H_n stretching n=1, 2, and 3	2100	Kelly (2010) [112], Rodriguez (2012) [133]
FS-Si-QDs	Partially oxidized Si–H, O_3Si–H	2250	Kelly (2010) [112]
FS-Si-QDs	Si–H stretching in intermediate oxidation states O_2SiH_2 and O_2SiSiH	2255	Kortshagen (2011) [140]
Plasma synthesized FS-Si-QDs	Si–O–Si stretching in O_3SiH	2270	Liptak (2009) [94]
Amorphous silicon	Si–H stretching in $HSi–Si_{3-n}O_n$n for n=1, 2, and 3	2100, 2195, 2265	Zacharias* (1996) [139]
FS-Si-QDs	CH_2 and CH_3 ν stretching	2400	Kelly (2010) [112]
Si-QDs	CH_2 Symmetric Stretching, Asymmetric Stretching and CH_3 Stretching	2856, 2926, 2960	Wang (2012) [141]
Plasma synthesized FS-Si-QDs	Si–OH stretching	3400	Liptak (2009) [94]
Amorphous silicon	O–H stretching	3500	Zacharias* (1996) [139]
Plasma synthesized FS-Si-QDs	Si–OH stretching	3650	Liptak (2009) [94]

Table 2.1. FTIR assignments for various bonds that may occur in nanocrystalline silicon. (* and references therein.)

To examine how the FTIR spectrum evolved during the photoactivation process, the controlled gas environment system described previously was moved adjacent to the FTIR setup. The Si-QDs were photoactivated in the controlled gas environment, their PL collected at the end of each minute of irradiation, and then taken out of the sealed chamber and measured in the FTIR apparatus. This procedure was repeated over a series of PA times until the observed changes had nearly saturated.

Figure 2.9. Continuum FTIR microscope and Thermo Nicolet 8700 FTIR main bench.

Data collected from the FTIR instrument was displayed in the OMNIC v8.3 software suite. Raw data often showed a sloping baseline, typically due to increased scattering of shorter wavelengths. This necessitated a "baseline correction". Basically, one identifies parts of the spectrum that are "featureless" and connects them with the baseline correction tool. Baseline-corrected data has a horizontal baseline showing near-zero absorbance. Next, the FTIR absorption peaks were directly correlated with specific chemical bonds in the FS-Si-QDs using the various known Si/O/H-related bond vibration energies given in Table 2.1. Changes in the magnitude of the absorption peaks were interpreted relative to the initial spectrum, by graphing the absorption data as a time-series, colored using a rainbow colormap corresponding to PA time.

2.6.2 ESR Theory

Electron spin resonance spectroscopy, also known as electron paramagnetic resonance spectroscopy, measures the absorption spectrum of unpaired electrons in molecular systems. It works on the basis of the fact that the degeneracy of the electron spin states ($m_s = \pm 1/2$) can be broken by an external magnetic field. The electronic transition between spin states can then be induced by the application of electromagnetic radiation of a specific frequency [142].

The governing equations for ESR are derived from a full quantum mechanical description of electron spin energies associated with unpaired electrons in a magnetic field. The energy levels of the spin states for an electron in a magnetic field will split proportional to the magnitude of the applied field, a phenomenon known as the Zeeman effect. The associated energies are described by the spin Hamiltonian

$$\hat{H}_s = g\mu_B B\hat{S}_z \tag{2.4}$$

where g is simply called the *"g*-factor", μ_B is the Bohr magneton (9.274×10^{-4} J/G), B is the magnetic field strength in Gauss, and S_z is the z-component of the spin angular momentum operator (with the magnetic field defined *a priori* to be in the z-direction).

The energy for an electron spin in the presence of an external magnetic field is the eigenvalue of the Hamiltonian above, which can be expressed as

$$E_\pm = \pm\frac{1}{2}g\mu_B B. \tag{2.5}$$

The energy difference between the two non-degenerate spin states can be expressed in terms of a photon of energy, $h\nu$, according to the equation

$$\Delta E = E_+ - E_- = g\mu_B B = h\nu, \tag{2.6}$$

where h is Planck's constant ($h = 6.626 \times 10^{-25}$ J/GHz), and ν is the photon frequency. Rearranging Eq. 2.6 leads to an expression for the g-factor

$$g = \frac{h\nu}{\mu_B B}. \tag{2.7}$$

Thus, if we fix either $h\nu$ or B and vary the other, we effectively scan over a range of g-factors. When one "hits" a specific g-factor corresponding to the electron states in a given sample, the microwave energy is absorbed as electrons are excited from one spin state to the other.

Since the coefficients of absorption and stimulated emission are equal, no net absorption would be observed if the electrons were equally distributed between the two spin-states. However, the population of electron spins instead follows the Boltzmann distribution according to the equation

$$\frac{n_{excited}}{n_{ground}} = e^{-\frac{\Delta E}{kT}}, \tag{2.8}$$

where k is Boltzmann's constant, T is the temperature, ΔE is the energy difference between the two states, and $n_{excited}$ and n_{ground} are the number of electrons in E_+ and E_- respectively. Thus, at high temperatures, microwave radiation will be absorbed by unpaired electrons in their ground states.

Let us describe the so-called "g-factor", since it is characteristic of unpaired electrons in specific environments (*e.g.*, a P_b-type defect in silicon) and determines the energy of the ESR absorption lines. The g-factor is also known as the *dimensionless magnetic moment*, which relates the experimentally observed magnetic moment of a particle (in this case a localized, unpaired electron), to the fundamental unit of magnetism, the Bohr magneton. The free-electron g-factor ($g_e = 2.002319304361(53)$) is one of the most precisely measured values in physics.

The ESR spectrum of an unpaired electron represents one of the simplest forms of spectroscopy, consisting of a single absorption line. However, in physical systems there are several environmental factors that can affect the unpaired electron g-factor. These effects include the local electronic environment, which alters the angular momentum of the unpaired electron, and the nuclear spin of the atom, which can couple through hyperfine interactions to the spin of the unpaired electron. However, since 98% of naturally occurring Si is ^{28}Si, the hyperfine interactions in Si-QDs are very weak. Thus, unpaired electrons can be distinguished based on the local electronic structure [142]

In a material the g-factor is affected by spin-orbit coupling and nuclear hyperfine

interactions [142]. The g-factors for electrons in materials are often calculated using a matrix-based approach, which contains terms for the orbital angular momentum operators acting upon electronic states in neighboring atoms. Higher-order terms can also be added to describe the nuclear hyperfine interactions. This "g-matrix" describes the components of the magnetic moment of an electron in 3-dimensional space. The components of the g-matrix are determined by the extent that nearby p-, d-, or f-orbitals interact with the electron being considered [142]. While a detailed re-derivation of these equations is beyond the scope of this thesis, the important point to understand is that the electron g-factor is a signature of the local electronic structure. As for FTIR, "atlases" of g-factors can be compiled for unpaired electrons in a wide variety of chemical environments [142]. By comparing the ESR results to known absorption lines, one can extract the types of paramagnetic "defects" present in the sample.

FS-Si-QDs are a good system for characterization by ESR. The fast-etching process produces QDs with a hydrogen-terminated surface [30], implying that in an ideal sample, all electrons on the QD interfaces are covalently paired with an electron from a bound hydrogen atom. However, when a hydrogen atom is missing from the surface of a silicon QD, the resulting unpaired electron can become an absorber in an ESR experiment. These unpaired electrons form the P_b-type surface defects described previously (Sec. 1.2.3). In powdered samples, randomly oriented electronic defects (such as those present in P_b centers in powders of FS-Si-QDs), can be characterized by the components of their g-matrices parallel and perpendicular to the direction of the magnetic field (*e.g.* $g_{\parallel}$ and $g_{\perp}$).

To summarize the key points, ESR is used to generate absorption spectra associated with unpaired electrons in materials. In this work, these unpaired electrons are mainly located at the surface of the silicon QDs [143]. By measuring the g-factor and comparing it to a list of known values (Table 2.2) for related materials (mainly porous silicon), one can extract information about the type, and equally important, the quantity of defects present in samples of FS-Si-QDs.

Material	Defect	g-factor	Reference
P-type PSi	P_b	$g = 2.0055$	Bardeleben 1993. [85]
PSi	P_b center	$g_\parallel = 2.0021 \pm 0.0002$ $g_\perp = 2.0089 \pm 0.0002$	Bratus 1994. [86]
PSi (aged in ambient for 2 months)	Si dangling bond (P_b center)	$g_\parallel = 2.0020 \pm 0.0001$ $g_\perp = 2.0089 \pm 0.0001$	Schoisswohl 1995. [87]
	Si dangling bond defect	$g = 2.0055$	
Oxidized PSi	P_b & P_{b0}	$g_\parallel[111] = 2.0019 \pm 0.0003$ $g_\perp[111] = 2.0089 \pm 0.0003$	Cantin 1996. [88]
	P_{b1}	$g_\parallel[0\bar{1}1] = 2.0058 \pm 0.0003$ $g_\parallel[2\bar{1}\bar{1}] = 2.0029 \pm 0.0003$ $g_\parallel[111] = 2.0069 \pm 0.0003$	
P-type PSi	P_b & P_{b0}	$g_\parallel[111] = 2.0019$ $g_\perp[111] = 2.0089$	Cantin 1996. [89]
	P_{b1}	$g_\parallel[0\bar{1}1] = 2.0058$ $g_\parallel[2\bar{1}\bar{1}] = 2.0029$ $g_\parallel[111] = 2.0069$	
Porous SiGe	Ge dangling bond	$g = 2.0019$	Schoisswohl 1996. [90]
	Si dangling bond	$g = 2.0055$	
	Si P_b	$g_\parallel = 2.0022$ $g_\perp = 2.0084$	
Si-QDs in SiO_2	E'center (oxygen vacancy)	$g = 2.002$	Pellegrino 2003. [95]
	Si dangling bond (P_b center)	$g = 2.005$	

Table 2.2. Paramagnetic centers in porous silicon, porous SiGe, and Si-QDs and their corresponding g-factors, from selected works in the literature.

2.6.3 ESR Data Collection

FS-Si-QDs were prepared as described in Sec. 2.1.2 and transported to the University of Saskatchewan's Structural Sciences Centre, where ESR experiments were carried out. ESR experiments were conducted on a Bruker EMX ESR spectrometer (Fig. 2.10), under the supervision of Dr. Ramaswami Sammynaiken. The spectrometer operates in the X-band, corresponding to photon frequencies of $\nu = 9.3561166 \pm 0.0000001$ GHz (3.87×10^{-5} eV). Microwave frequency bands are designated by the Radio Society of Great Britain, with the X-band being designated as 8 to 12 GHz and the Q-band as 33 to 55 GHz. X and Q-band microwaves are used extensively for ESR measurements (mainly due to the historic availability of microwave components

at these frequencies).

Figure 2.10. Bruker EMX X-band ESR spectrometer at the University of Saskatchewan's Structural Sciences Centre.

The microwave generator is coupled to the microwave cavity using a computer-controlled tunable waveguide, allowing the power inside the cavity to be adjusted. The cavity is located between two computer controlled solenoids, which generate the magnetic field. Two smaller sets of coils are used to produce an AC modulation in the overall magnetic field. A diode measures the microwave power returning along the waveguide, which is the basis for the absorbance measurement. The computer interface to the spectrometer allows the experimenter to set up the initial conditions, including the magnetic field strength, modulation, and power, before running an experiment. Experiments required tens of seconds to tens of minutes to complete, depending on the resolution and signal-to-noise ratio desired. In these experiments, the microwave frequency was held at the fixed resonant frequency of the cavity ($\nu = 9.3561166$ GHz), and the magnetic field strength was scanned from $B = 3300.62$ G to $B = 3360.62$ G.

In the ESR spectrometer, the detector diode produces a current proportional to the microwave power reflected from the cavity. A direct measurement of the current passing through the diode will detect noise at all frequencies. In order to increase the signal-to-noise ratio, a small-amplitude 100 kHz magnetic-field modulation was

employed. This field modulation superimposes an alternating current component onto the diode signal, which can then be amplified by a frequency-selective lock-in amplifier tuned to 100 kHz. Thus, for a single cycle of the modulated magnetic field, one detects the *change* in the sample absorption over the small field amplitude, which amounts to the detection of the *first derivative* of the absorption spectrum. The resulting data has a much better signal-to-noise ratio, and, as a side benefit, first-derivative spectra have more easily recognizable features than raw absorption spectra [142].

2.6.4 ESR Analysis

The ESR experiments generated first-derivative ESR spectra that were exported as text files. This data was analyzed as a part of a time-series to extract the total ESR absorption intensity as a function of PA time. Data collection from the ESR instrument was more time-consuming than the PL and FTIR data collection, so ESR absorption spectra during PA were limited to 7 different photoactivation times. A background spectrum was also collected with a standard NMR tube for comparison with FS-Si-QD samples.

Analysis of the ESR spectra began by importing the data files into Mathematica, including the background spectrum. Data files were imported into multidimensional matrices and the background ESR spectrum was point-wise subtracted from the data to eliminate the signal associated with the NMR tubes. The ESR time-series data was graphed using a rainbow colorspace to represent photoactivation time (Fig. 2.11 (a)). The Mathematica code for PL time-series analysis can be reviewed in Appendix B.

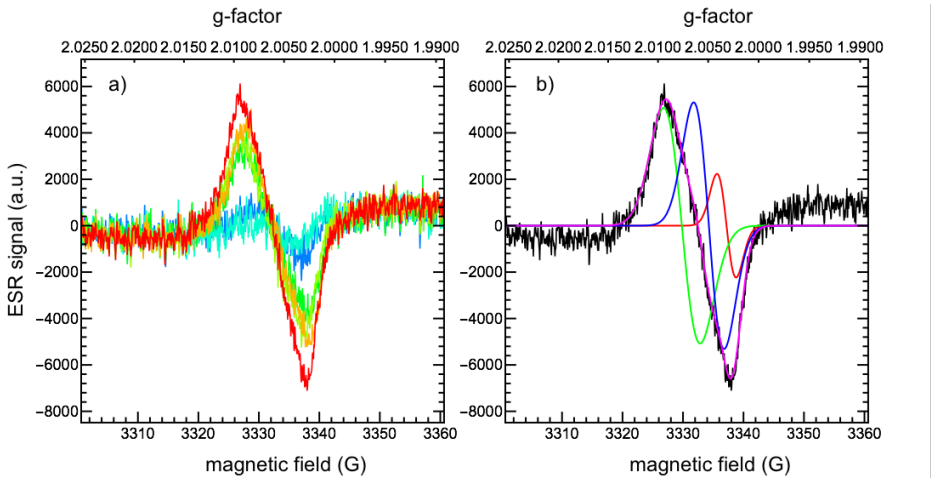

Figure 2.11. Analysis of ESR time-series data: a) ESR first-derivative spectra from a 60-minute photoactivation time-series, shown here with initial values in blue and final values in red. b) Final ESR spectrum (black), fitted with three first-derivative Gaussian functions with g-factors of approximately 2.003 (green), 2.005 (blue), and 2.007 (red), corresponding to $g_{\|}$, $g_{\perp}$, and g_D described in Sec. 1.2.3.

The absorption curve attributed to paramagnetic defects in the ESR spectra can be approximated by combinations of Gaussian and Lorentzian functions [144, 145]. To analyze the data, the first-derivative spectra were fit with first-derivatives of the Gaussian, Lorentzian, and pseudo-Voigt functions, with central values corresponding to the relevant g-factors. The g-factors were not fixed by the fitting function, and were optimized along with the spectral intensity[2] (A) and the standard deviation (σ). Mathematica simplified this process thorough the use of the NormalDistribution function (Gaussian), the CauchyDistribution function (Lorentzian), and the derivative function, D. For the pseudo-Voigt profile [145], a custom equation for the Gaussian and Lorentzian distributions took the following form:

$$y(\nu) = fL(\nu) + (1 - f)G(\nu), \tag{2.9}$$

were $L(\nu)$ and $G(\nu)$ are given as

[2]It should be noted that the spectral intensity (A) for the $g_{\|}$ and $g_{\perp}$ defects are related by the geometry of the P_b centre, where the 's' and 'p' character (corresponding roughly to the $\perp$ and $\|$ components), occur with $s/p = 0.25$ [85]. While this ultimately reduced the number of variables in the fitting function from 9 to 8, the final fits using both methods were similar.

$$L(\nu) = \frac{2A/\pi\gamma_0}{1 + 4[(\nu - \nu_0)/\gamma_0]^2}, \tag{2.10}$$

and

$$G(\nu) = \frac{A}{\gamma_0}\sqrt{\frac{4\ln 2}{\pi}} exp\left[-4\ln 2\left(\frac{\nu - \nu_0}{\gamma_0}\right)^2\right]. \tag{2.11}$$

Generally, the best fits were found to have a 100% Gaussian character. For this reason, the first-derivative Gaussian distribution was used in the fitting (Fig. 2.11 (b)). Once the time-series ESR data was fit, values for the individual integrated intensities could be deduced. However, in the final analysis, only the sum of the three defect integrated intensities was used, for reasons discussed in Chapter 5. Changes in the magnitude of the absorption signal were interpreted relative to the initial spectrum as an increase in the overall defect concentration.

We note here that pure ESR absorption lines should have a Lorentzian lineshape [140, 142]. In ESR studies, there are several factors that can cause peak broadening. These include dipolar broadening in concentrated crystals, strain broadening due to dislocations and other crystal defects, spin-lattice relaxation [144, 146, 147], and the instrument response itself [144]. The convolution of a Lorentzian absorption line with a Gaussian, can, for example, result in a Voigt lineshape with mainly Gaussian character. While the origin of ESR lineshapes is beyond the scope of this thesis, here we note simply that the observed absorption lines were dominantly Gaussian in nature.

A rough estimate of the concentration of defects in the Si-QD samples was obtained by comparison to an ESR standard called "weak pitch". The weak pitch mixture consisted of 0.00033% pitch in KCl (Sample #01012W11 from Bruker Inc.), with 1×10^{13} spins/cm^3. A sample was prepared by mixing 0.0051 g of Si-QD composite (Sec. 2.1.2) with 0.1960 g of SiO powder (2.6% composite in SiO by mass), which was thoroughly ground and mixed for one hour. This sample and the weak pitch were placed into separate NMR tubes and packed by vibration to remove air gaps. Under identical conditions, the area under the ESR spectrum for the Si-QD sample was four times that acquired for the weak pitch. Since pure stoichiometric specimens of SiO are expected to show no ESR response [148], the ESR spectrum

obtained gives an estimate of the number of defects in the Si-QD composite. The weak pitch concentration is multiplied by the ratio of the ESR intensities (4) and normalized to the mass percent of the weak pitch (2.6%/0.00033%) to obtain 3.15×10^{16} spins/cm^3 in the Si-QD composite. Estimating the number of QDs in the composite powder at 14% (by mass), and assuming ~538 Si atoms for a 2.5-nm-diameter QD [149] gives an estimate of 2.85×10^{16} QDs/cm^3, or roughly 1 defect per QD. Note, however, that after HF etching, the number of defects is expected to diminish substantially [150].

Chapter 3

Paper: Photoactivation of Silicon Quantum Dots

Abstract

We show that free-standing silicon quantum dots (QDs) can be photoactivated by blue or UV optical irradiation. The luminescence intensity increases by an order of magnitude for irradiation times of several minutes under moderate optical power. The cut-off energy for photoactivation is between 2.1 and 2.4 eV, not very different from the activation energy for hydrogen dissociation from bulk silicon surfaces. We propose that the mechanism for this effect is associated with silicon-hydride bond breaking and the subsequent oxidation of dangling bonds. This phenomenon could be used to "write" luminescent quantum dots into pre-determined arrays.

3.1 Introduction

Semiconductor quantum dots (QDs) have surface areas exceeding 1200 m^2 per cubic centimeter of material, and the interface can therefore have a profound influence on their physical and optoelectronic properties. Fluorescent QDs, in particular, are finding new applications in areas ranging from biomedical imaging [105, 108] to microphotonics [151, 152]; however, even low abundances of surface defects or the presence of charge trapping species can modify or quench the luminescence. This is one reason commercially available QDs are generally protected with an epitaxial shell consisting of a second, larger-bandgap semiconductor [153]. This structure ensures a high-crystal-quality interface, maintains strong confinement in the core, and prevents unwanted interactions between the dot surfaces and the surroundings.

Silicon QDs (Si-QDs) are attractive because of their low toxicity [108], compatibility with microelectronic fabrication methods, high quantum efficiency [154], and ease of fabrication. Unfortunately, epitaxial core-shell structures similar in quality to those achievable in the II–VI compound QDs are not yet known; therefore, the Si-QD interface can have a substantial influence on the luminescent properties [67,155–157]. In particular, the nature of the Si/SiO_2 interface is thought to play an important role in producing the typical red luminescence demonstrated by oxide-embedded Si-QD nanocomposites [68, 153, 155].

For oxide-embedded Si-QDs, the following surface structures are thought to influence the luminescence spectrum and intensity: (i) the Si=O bond [62,67], (ii) the silicon dangling bond, or neutral P_b center [83], (iii) the silicon-hydride bond [132], and (iv) the Si–O–H surface termination [158–160]. Structures (i) and (iv) are thought to produce sub-gap radiative states associated with the typical red luminescence of oxide-embedded Si-QDs [62,67,160]. Structure (ii) produces a fast non-radiative trap that can be passivated by hydrogen, leading to structure (iii). Hydride (as well as oxygen) passivation effectively removes non-radiative trapping processes associated with unsatisfied silicon bonds, thereby increasing the luminescence efficiency [132].

There is evidence that interface defects in Si-QDs can evolve upon exposure to UV irradiation. For example, irradiation of hydride-passivated, oxide-embedded Si-QDs causes a red-shift of the photoluminescence (PL) spectrum, along with a temporary

increase in the PL intensity [132]. This behavior was attributed to the introduction of oxide-related interface states during irradiation in air. Continued irradiation resulted in a subsequent decrease in the PL intensity, an effect hypothesized to arise from a re-introduction of P_b centers. In another work, UV irradiation also caused a minor increase in PL intensity that was attributed to the oxidation of P_b centers on the surface of Si-QDs [74].

The majority of previous investigations have focused on silicon QDs embedded in an oxide matrix. Unfortunately, these materials provide fairly limited physical access to the interface structures, which, *e.g.*, can be controlled to a limited degree by thermal processing at elevated temperatures (by hydride or deuterium passivation and cycling [161]) and by UV irradiation. The irradiation-induced changes in the luminescence intensity were also quite small, on the order of 10%. In the present work, we used samples in which Si-QDs embedded in a silica matrix were liberated using HF etching to yield free-standing hydride terminated nanocrystals. These particles were initially in a suspension, in order to enable a more direct manipulation and control of surface chemistry, and to ensure that minimally-oxidized structures were used [30, 31, 157].

3.2 Materials and Methods

3.2.1 Preparation of Free-Standing Si-QDs

Silicon QDs were prepared using hydrogen silsesquioxane (HSQ: chemical formula $H_{12}Si_8O_{12}$) dissolved in methyl isobutyl ketone (MIBK). HSQ was heated to 1100 °C under a 95% Ar + 5% H_2 atmosphere to produce nanocrystal QDs embedded in a silica matrix. Full details of the present QD synthesis and characterization may be found in Ref. [30]. The process provides gram quantities of Si-QDs embedded in a silica matrix.

The Si-QDs were liberated by HF etching of the matrix using a 1:1:1 mixture of ethanol, water, and hydrofluoric acid (49% HF) (by volume) for 50 min while stirring under ambient conditions. This process removes the SiO_2 matrix and yields hydride terminated Si-QDs. The suspended QDs were then extracted into toluene [111], and subsequently dropped onto silicon wafers. To prevent excessive agglomeration, the

toluene suspension was evaporated drop-by-drop by gently blowing dry N_2(g) over the surface of the wafer in a circular motion until the solvent was evaporated. This method yielded a discontinuous coating of free-standing Si-QDs on the surface of the wafer.

3.2.2 Optical Characterization and Irradiation

Si-QD luminescence was obtained by pumping the sample with 325 nm light from a HeCd laser operated at a continuous wave power of 13.8 mW. The PL spectra were collected using a fiber optic spectrometer that was calibrated with a standard black-body source (for intensity) and an HgAr lamp (for wavelength). The luminescence emitted by the Si-QDs was passed through a long-pass filter to minimize the amount of scattered laser light when collecting PL spectra.

A series of PL experiments were performed. These included:

1. The effect of irradiation wavelength was investigated using a single-line ArKr ion laser operated at 457, 514, 568, or 647 nm with a continuous-wave power of 50 mW. Irradiations were also performed using the 325 nm line from the HeCd laser.

2. Time-resolved PL experiments were performed by "chopping" the ArKr laser beam with an acousto-optic modulator (using a wavelength of 476 nm and power of 22 mW). The resulting PL dynamics were measured with a single-photon-counting photomultiplier system with a multiscaler set to 200 ns time bins.

3. Si-QD films were heated in ambient atmosphere to temperatures up to 300 °C, before and after which PL spectroscopy and laser irradiation were performed.

4. The PL spectrum was measured on samples irradiated in vacuum (10^{-6} Torr) and the results compared to those from air-irradiated samples. For consistency, all PL spectra were collected using the 325 nm excitation source. When irradiating the samples with other wavelengths, precautions were taken to minimize the influence of the 325 nm laser needed to excite the PL. This was achieved by using a programmable servo to switch between the 325 nm excitation source

and the irradiation source. The 325 nm source excited the sample for PL data collection at intervals of 4 s every minute, while for the remaining 56 s the sample was exposed only to the ArKr laser. Control samples were only exposed to the 4 s data collection intervals.

3.2.3 TEM Characterization

Samples were prepared for transmission electron microscopy (TEM) by dropping a small fraction of the toluene suspension containing the Si-QDs onto a 400 mesh copper grid with a 16 nm-thick carbon film. Bright field imaging and electron diffraction were performed on a JEOL 2010 TEM with a LaB_6 filament. High-resolution imaging and energy-filtered scanning transmission electron microscopy (EFSTEM) employed a JEOL field emission 2200FS TEM equipped with an Ω-filter. EFSTEM imaging was accomplished by centering an energy-filtering slit at an energy loss of 99 eV, corresponding to the L23 absorption line of silicon. The slit width corresponded to a 10 eV energy window. Using these values, silicon QDs will appear bright against a darker background.

3.2.4 FTIR Characterization

Samples were prepared for Fourier transform infrared spectroscopy (FTIR) analysis by casting the suspension containing the Si-QDs onto a potassium bromide plate and allowing the toluene to evaporate. For each experiment, two samples were prepared; a control sample that was not irradiated, and one that was irradiated in air for 1 h using the 325 nm HeCd laser. An additional pair of samples was prepared to examine the effect of temperature; one was heated but not irradiated, and the other was heated and subsequently irradiated with the HeCd laser for 1 h. Spectra were acquired using a Thermo Nicolet Nic-Plan FTIR microscope attached to a Magna 750 main bench with a wavelength resolution of 4 cm^{-1} and a spectral range of 4000-650 cm^{-1}. Thirty-two scans were taken per spectrum and averaged in order to reduce noise.

3.3 Results

3.3.1 Microstructure

Low magnification bright-field TEM imaging (Fig. 3.1a) revealed the presence of Si-QDs, as confirmed by electron diffraction (Fig. 3.1b) and HRTEM (Fig. 3.1c). Most QDs were aggregated into small clusters clearly observable in Fig. 3.1a. Fig. 3.1d shows an EFTEM image of a small cluster of nanoparticles that indicates the presence of Si in this imaging region. The size distribution obtained from the bright field imaging was fit with a lognormal function, resulting in a mean QD diameter of 3.1 nm and a geometric standard deviation of 0.55 nm.

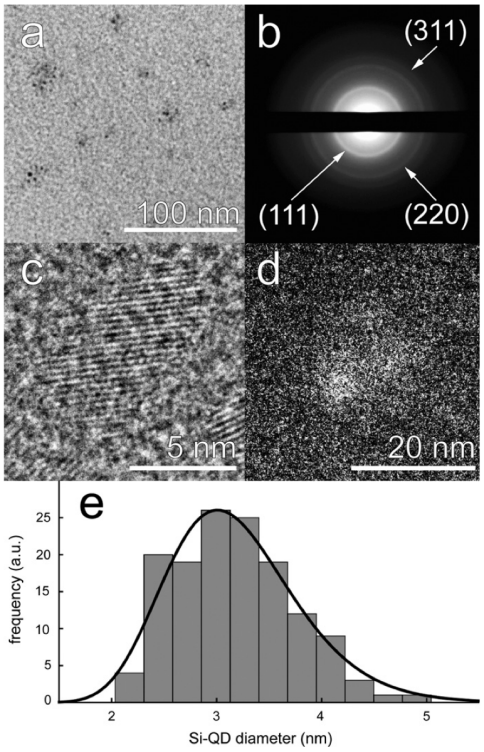

Figure 3.1. (a) Bright field image showing that the QDs (small black dots) are grouped into clusters containing typically 5-10 particles; (b) contrast-enhanced electron diffraction pattern exhibiting rings characteristic of the lattice spacings of crystalline silicon; (c) high-resolution image showing individual Si-QDs with fringe spacings corresponding to the (111) lattice planes of silicon; (d) contrast enhanced energy-filtered high-resolution image using an energy loss window centered at 99 eV. A small group of Si-QDs appears as bright "blobs" near the center of the image; (e) a size distribution histogram taken by visual measurement of the particles observed in bright field imaging. The lognormal fit is superimposed.

3.3.2 Irradiation in Air

Initially, the drop coated hydride terminated Si-QDs showed a weak luminescence centered at approximately 800 nm. Following exposure to 325 nm laser irradiation (13.8 mW, beam diameter $\sim$ 2 mm; flux $\sim 2.2 \times 10^{16}$ m^{-2} s^{-1}), the integrated PL intensity initially decreased and blue-shifted to 675 nm. Upon extended exposure (*i.e.*, 60 min), the PL emission intensity increased markedly, and red-shifted slightly (Fig. 3.2). The PL intensity and shift in peak wavelength approached, but did not reach saturation after a 60 min irradiation. We refer herein to the observed increase in luminescence intensity under optical irradiation as *photoactivation*. The magnitude of this effect suggests that the hydride surface terminated Si-QDs can be effectively "turned on" in a controlled manner using UV irradiation.

The influence of the irradiation wavelength on the photoactivation was also evaluated. We found that photoactivation occurs for irradiating wavelengths up to 514 nm, but that it required a higher total photon fluence to achieve an equivalent integrated luminescence intensity (Fig. 3.3). The magnitude of the photoactivation effect at an equivalent fluence decreased going from irradiation wavelengths of 325–514 nm. Irradiation wavelengths of 568 and 647 nm produced no detectable photoactivation beyond that of the control sample (the control sample was irradiated only with the 325 nm PL excitation beam for 4 s intervals, every minute).

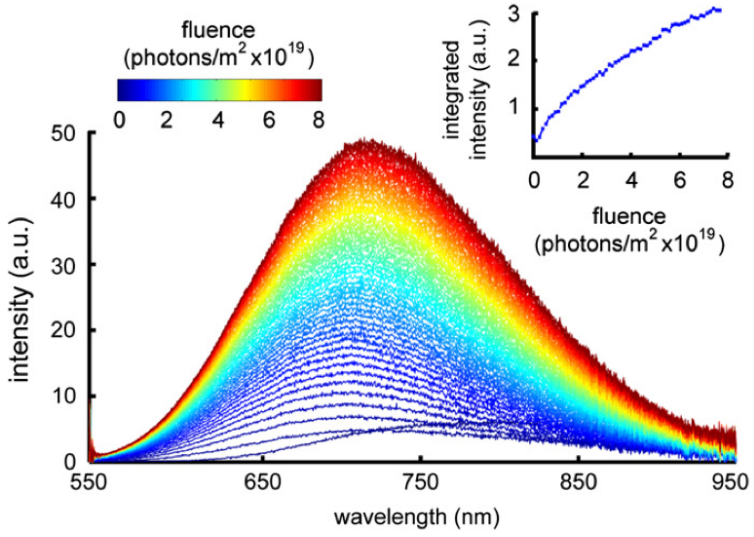

Figure 3.2. PL spectra as a function of irradiation fluence. The inset shows the integrated PL intensity as a function of fluence.

The photoluminescence lifetime of samples with various 325 nm irradiation fluences were evaluated. During pulsed excitation the PL decay followed the stretched exponential function given by$I_t = I_0 exp(-(t/\tau)^{\beta})$, which typically reflects a distribution of lifetimes [162]. Here, τ is the effective lifetime and β is a stretching parameter that can be between 0 and 1 and takes on smaller values for broader lifetime distributions [136]. As shown in Fig. 3.4, the PL lifetime of the QDs increased from 10 to 30 μs over the course of 55 min under 476 nm laser irradiation (total fluence = 1.58×10^{20} photons/m^2). The increase in β reflected by the smaller curvature of the decay curves for the irradiated samples ($\beta = 1$ corresponds to a single exponential and would be a straight line in Fig. 3.4).

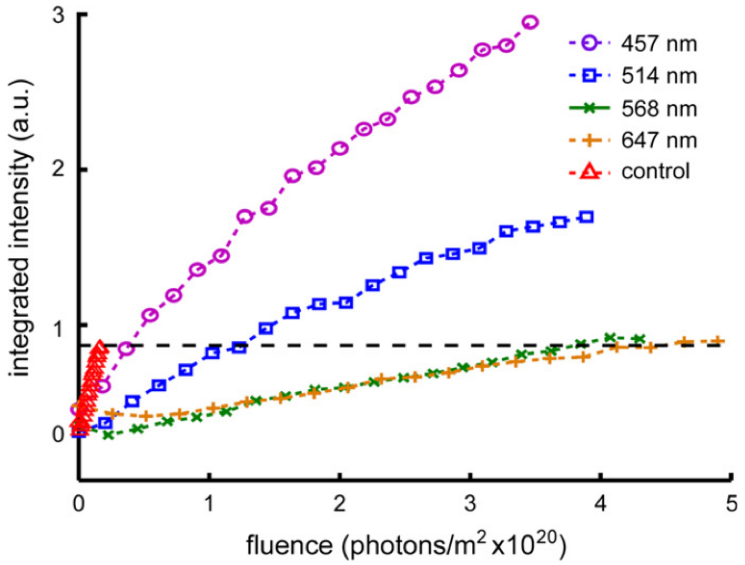

Figure 3.3. Integrated intensity of the Si-QD PL as a function of fluence for various irradiation wavelengths. The control (red points) was exposed only to the data collection beam (at a wavelength of 325 nm) so it does not reach the same high fluences as the other curves. The integrated intensity of the samples irradiated at wavelengths of 568 and 647 nm shows no increase beyond that of the control sample (dashed line), indicating that the photoactivation effect does not occur for these longer wavelengths.

Based upon the TEM analysis shown in Fig. 3.1, the QDs are not as closely packed as in thin film composites [163], therefore QD–QD interactions are unlikely to account for the stretched exponential decay (assuming that the nanoscale dispersions are not dramatically different on the TEM grid compared to the Si wafer) [164].

Furthermore, particle–particle interactions would not account for the decay curve evolution under optical irradiation, since the QD separation distances should not be affected by exposure to light. Therefore, the increases in τ and β suggest that the lifetimes are becoming both longer and more narrowly distributed around a central value. Similar to the PL spectral intensity, both variables appear to approach but do not reach saturation after a fluence of $\sim 1.7 \times 10^{20}$ photons/m^2 (Fig. 3.4).

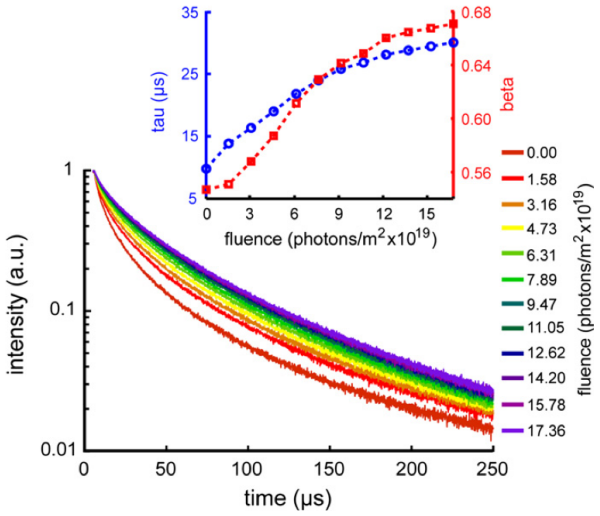

Figure 3.4. Photoluminescence decays as a function of fluence for Si-QDs irradiated at 476 nm. The inset summarizes the changes in τ and β as a function of fluence.

3.3.3 Other Influences: Ambient Temperature and Atmosphere

Samples drop-coated onto silicon wafers showed relatively weak PL intensity prior to photoactivation. One sample (a control) was irradiated at room temperature with 325 nm laser light to a fluence of 5.4×10^{18} photons/m^2. It showed an increase in PL intensity and a peak blue-shift, consistent with previous experiments. The irradiation was then stopped and the control sample was heated to 300 °C for 1 h in air. After cooling, the room temperature PL remained approximately at the same intensity as observed after photoactivation – *i.e.*, the heating and cooling cycle produced no significant change in the PL intensity. However, no further photoactivation could be produced with this sample, although the photoactivation had not saturated prior to heating. Heating to 300 °C in air had the effect of "locking in" the PL spectrum.

Another sample was heated to 300 °C for 1 h before irradiation, and allowed to

cool to room temperature. After the heating and cooling cycle, the PL spectrum was slightly blue-shifted, but exposure to UV irradiation produced no measurable photoactivation. Once again, the PL intensity was effectively locked in – but this time at a low value.

In an attempt to isolate the role of oxidation in the observed photoactivation of Si-NC PL, we performed a series of photoactivation experiments in vacuum ($\sim 1 \times 10^{-6}$ Torr). A sample of hydride-terminated Si-QDs was drop coated onto a silicon wafer and irradiated at $\lambda = 476$ nm while in a vacuum chamber maintained at $\sim 10^{-6}$ Torr. A spectral blue-shift and gradual decrease in PL intensity was noted; however, there was no photoactivation after a total fluence of 1.15×10^{20} photons/m^2. Thus, free-standing Si-QDs irradiated in vacuum do not photoactivate.

3.3.4 FTIR Characterization

FTIR spectra show several clear changes after irradiation (Fig. 3.5). The spectrum of as prepared hydride-surface-terminated Si-QDs (*i.e.*, Fig. 3.5a) shows three spectral regions (*i.e.*, Si–H stretching, Si–O–Si bending, and Si–H wagging) that evolve upon photoactivation (*i.e.*, Fig. 3.5b and c). A strong absorption with maxima at 2080 and 2100 cm^{-1} is observed, with a shoulder near 2110 cm^{-1}. These features are typically assigned to SiH, SiH_2, and SiH_3 stretching, respectively [94]. After irradiation in air, this silicon hydride spectral region decreases in intensity and new absorptions at 2190 and 2240 cm^{-1} arise that may be assigned to O-Si–H structures [165]. The Si–O–Si spectral region shows a broad feature at 1150 cm^{-1} prior to photoactivation. Upon exposure to incident 325 nm light, this oxide feature narrows and increases in intensity. Additional weak absorptions at $\sim$950 cm^{-1} also appear after irradiation in air, consistent with surface oxidation [165]. Finally, a strong narrow absorption at $\sim$905 cm^{-1} assigned to the SiH_2 wag in the as-prepared sample decreases in intensity and broadens. All of these observations and the appearance after extended irradiation of a broad, weak absorption at 3300 cm^{-1} arising from Si–OH surface moieties [165], are consistent with photo-induced QD surface oxidation and a decrease in the concentration of silicon-hydride bonds.

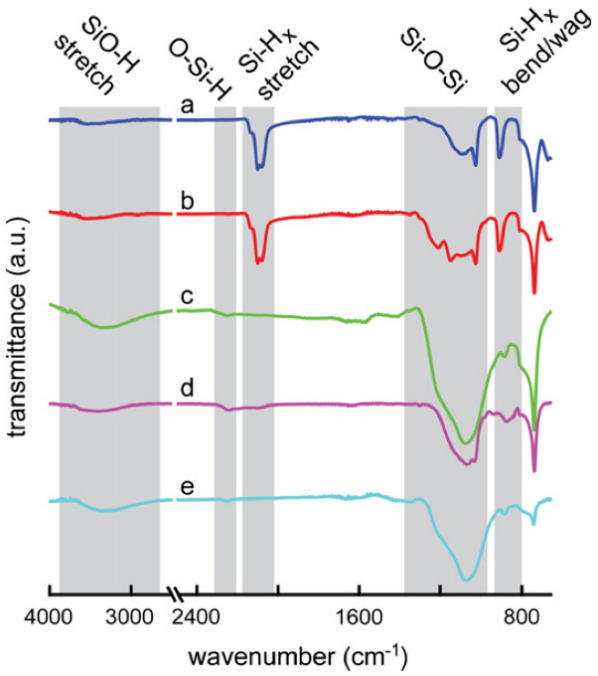

Figure 3.5. FTIR transmittance spectra of as prepared Si-QDs (a) immediately after toluene evaporation, (b) after 1 h in ambient conditions, (c) after 1 h in ambient conditions and a heating cycle to 300 °C, (d) after 1 h irradiation by a 325 nm laser (equivalent to 8×10^{19} photons/m^2), and (e) after 1 h irradiation by a 325 nm laser and a heating cycle to 300 °C. Data offset for clarity.

3.4 Discussion

In previous work [166], oxide-embedded Si-QD thin films were irradiated under similar conditions to those presented here and a 20% decrease in the PL intensity resulted; whereas we observe a ∼10-fold increase. Using a combination of FTIR and electron spin resonance (ESR) spectroscopic data Lee *et al.* [166] drew the conclusion that laser irradiation breaks any silicon-hydride bonds present on the Si surface, causing the formation of neutral P_b centers [167]. No evidence for the formation of Si–O surface bonding was presented. It is reasonable that the formation of irradiation-induced non-radiative P_b centers would decrease the luminescence intensity.

Our results are consistent with the proposal that irradiation with 325 nm light induces Si–H bond cleavage and the formation of non-radiative P_b centers. Although we do not have access to electron spin resonance apparatus to measure the P_b center concentration more directly, its effects manifest in PL lifetime data. Upon irradia-

tion in vacuum (not shown), we found the PL lifetimes decreased as a function of irradiation time, while the stretching parameter β also decreased. At the same time, the overall PL intensity (I_{PL}) decreased as well. These data are consistent with the proposal that 325 nm irradiation produces non-radiative traps. Although we do not have direct evidence that these traps are neutral dangling bonds, the formation of P_b centers would be consistent with the previous work [166]. In the absence of atmospheric oxygen and water vapor, there is no further evolution of the luminescence, other than a gradual decrease in τ, β, and I_{PL}.

Irradiation in air, however, produces quite a different result. We initially observed a rapid decrease in I_{PL} in the first few minutes, followed in this case by the very pronounced photoactivation effect. During continued irradiation in air, there was a monotonic increase in τ, β, and I_{PL}. The increase in τ with increasing irradiation fluence in air is consistent with a net decrease in P_b center concentration. At the same time, we also found a pronounced increase in Si–O related vibrations in the FTIR spectrum. These data are uniformly consistent with oxide passivation of surface non-radiative centers, resulting from air exposure during short-wavelength irradiation. Thus, we propose a two-step process that we will explore further in the following paragraphs: first, the silicon-hydride bonds are cleaved, and then the resulting dangling bonds are oxidized.

Silicon-hydride bond breaking on bulk silicon surfaces has been well characterized, and leads to some interesting comparisons with the present results. In the case of bulk silicon surfaces, cleaving the Si–H bond under ultra-high vacuum requires an activation energy of ∼2.48 eV [168], which is close to the lowest photon energy that we found would drive the photoactivation process in free-standing QDs (Fig. 3.3). However, the activation energy for hydride dissociation from bulk silicon can decrease in the presence of water vapor; this process results in a Si–O–H surface termination instead of a dangling bond. The energy barrier for hydrogen dissociation in the presence of water may be as low as ∼2.2 eV [169]. Consistent with this picture, hydride desorption and hydration of the bulk silicon surface under optical irradiation was attributed to a photochemical oxidation assisted by water molecules in air [131]. In the present work, we found that photoactivation occurred for a 2.41 eV photon energy but not for 2.18 eV; quite similar to the values reported for hydride bond

cleaving in bulk silicon. Although the FTIR results point towards cleaving of the Si–H moiety we cannot fully discard silicon-silicon bond breaking at energies close to 2.8 eV [111].

The FTIR and PL lifetime data imply that the P_b centers initially present as a result of HF etching or created by the dissociation of hydride can be oxidized during irradiation in air. Analysis of the bulk system can be informative here as well. In the presence of O_2, the neutral dangling bond on bulk silicon surfaces can be oxidized in air, leading to various surface bond rearrangements (either in dry air or assisted by water vapor) [81, 170, 171]. The activation energy for incorporation of oxygen into silicon is ∼1.7 eV, presumably *via* oxidation of dangling bonds [81]. For example, hydride-terminated silicon can be oxidized in the presence of P_b centers by dissociation of oxygen at unpaired dangling bond sites [172]. Oxidation of dangling bonds involves the bonding of one oxygen atom (or an oxygen dimer) to two adjacent silicon dangling bonds on the surface, possibly followed by migration into a more energetically favorable back-bonding configuration, with an apparently low activation energy [173]. Therefore, if the irradiation energy is high enough for hydride dissociation, it is almost certainly high enough to initiate subsequent oxidation of the dangling bonds created in the first step, either directly *via* dissociation of O_2 or assisted by water vapor.

Other effects can modify the activation energies and probabilities of surface bonding and rearrangement. For example, recent calculations suggest the activation energies for oxygen migration in Si-QDs are somewhat greater than that in bulk, due to a lack of available low-energy surface configurations [174]. However, from the present work, we can see that the activation energies for Si–H bond breaking and oxidation are probably not very different from the range of values reported for bulk silicon under various oxidation/hydration conditions. Another effect that could influence the photoactivation reactions is the well-known Staebler-Wronski effect [175]. Here, electron-hole pair formation stimulates Si–H bond breaking or oxidation in amorphous silicon under optical irradiation (sometimes called "light soaking"). If similar processes occur in nanocrystals, in which the charge carriers are highly confined and are never far from the surfaces, one might expect that the Si–H bond breaking would occur at somewhat lower irradiation energies than expected in bulk silicon.

The origin of the small shifts in the peak of the PL spectrum during the photoactivation process is not straightforward to determine, although we can speculate as to the cause. Hydride passivation has been reported to cause a PL red-shift, which was attributed to the likelihood that larger particles contain more defects and, thus, their luminescence will be more strongly affected by passivation [128]. Since in the present case the process occurs in reverse (*i.e.*, larger particles are statistically more likely to be "depassivated" through hydrogen desorption upon irradiation), an initial intensity decrease and spectral blue-shift would be expected. The next stage involves the oxidation of the dangling bonds, which is the main photoactivation mechanism. The slight spectral red-shift that occurs here can be explained by essentially the same argument: during oxidation, the larger particles have more surface area and are proportionally more likely to have dangling bonds. Thus, the larger particles would be more strongly affected by oxidation, red-shifting the PL peak as the sample is photoactivated. The more difficult issue to explain is why the peak of the PL spectrum is blue-shifted after photoactivation, compared to the initial spectrum (Fig. 3.2). In some cases, an oxidation-induced blue-shift was attributed to the shrinking of the QD size during oxidation of the outer layers [68]. Oxidation of a single surface layer of, *e.g.*, a 3 nm particle could decrease the Si core size by 10% or more [62], possibly enough to account for the present observations.

The observed PL "locking in" effect caused by heating the QDs to 300 °C is more complex. Regardless of whether photoactivation had occurred, negligible additional evolution of the PL spectrum was manifested under irradiation after the sample had been heated to 300 °C. At the same time, the FTIR peak associated with the Si–O–Si stretch became strong and broad (Fig. 3.5). A similar effect was recently observed after heating 100 nm-diameter silicon particles to temperatures of 300-600 °C, which was interpreted as being due to the reorganization of the Si–O surface structures into more energetically favorable oxide configurations [176]. In order to explain the PL lock-in effect, a similar structural reorganization on the QD surfaces may occur that prevents further evolution of the surface bonding during irradiation.

Photoactivation in QDs may represent an opportunity for optical data storage [177–179], especially if one could perform read/write operations using near-field optics. In the case of CdSe QDs, photoactivation experiments showed an order-of-

magnitude increase in the PL intensity and an ability to write the activated dots into "letters" [177,178]. For Si-QDs, previous efforts toward luminescence patterning used a high-intensity laser to locally anneal an SiO_x film [167]. Here, we demonstrate that similar potential exists for free-standing Si QDs, using photoactivation. Proof-of-concept fluorescence patterning was performed by using a 400 mesh grid with 37 mm wide holes as a shadow-mask, through which a sample was irradiated. The results of these efforts are shown in Fig. 3.6. After the shadow-mask was removed photo-induced patterning of Si-QDs was clearly visible, although limited at this stage by agglomeration problems. Regions blocked by the supporting mesh are highly contrasted by regions that were photoactivated, although low level luminescence is visible throughout the sample. The QDs tend to clump into regions ranging from a few microns to a few tens of microns across, and this currently limits the quality of the photoactivated QD patterns. Photoactivation writing in Si-QDs will require better means of dispersing the QDs onto the wafer surface in order to produce smoother structures.

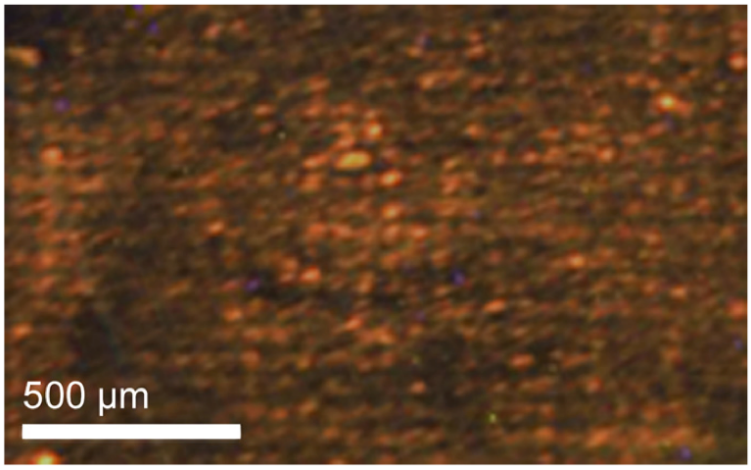

Figure 3.6. Fluorescence image showing a photoactivated pattern on Si-QDs. This sample was irradiated by the 325 nm laser with a total fluence of $\sim 8 \times 10^{19}$ photons/m^2.

3.5 Conclusion

Hydride-terminated free-standing Si-QDs can be photoactivated by laser irradiation at wavelengths of 514 nm or shorter in air. Photoactivation is likely caused by

the removal of hydride surface termination to form surface dangling-bonds on the QD surfaces that are passivated upon oxidation and facilitated by the presence of humidity in air. This process is characterized by an order-of-magnitude increase in the PL intensity. The luminescence produced by this mechanism is stable and long-lasting. The luminescence intensity can be "locked-in" at any point by heating the QDs to 300 °C. Si-QDs could be used for luminescence patterning or writing in a quick irradiation process, although more evenly dispersed QD films would need to be developed.

Acknowledgements

The authors thank NSERC, CIPI, and Alberta Ingenuity for funding this research.

Chapter 4

Paper: Sensing Water and Alcohol Vapors with Free-Standing Si Quantum Dots

---

Abstract

An all-optical silicon-quantum-dot-based vapor sensing method was demonstrated for the cases of atmospheric water and alcohols. The sensing mechanism employs the luminescence of freestanding silicon quantum dots prepared using a solution-state chemical etch followed by drop-casting onto a clean silicon wafer. When the sample was exposed to the vapors of water, ethanol, methanol, isopropanol, butanol or butanediol in an oxygen carrier gas, the luminescence spectra of the silicon quantum dots evolved on the order of seconds to hours. An orders-of-magnitude increase in the luminescence intensity was observed, with the rate of increase depending on the analyte vapor. The increase in the luminescence intensity is coincident with the formation of Si–O and Si–OH bonds on the surface of the hydride terminated Si quan-

tum dots, as determined by Fourier transform infrared spectroscopy and consistent with photoluminescence lifetime spectroscopy.

4.1 Introduction

Atmospheric vapor sensing with silicon quantum dots has largely been limited to devices based on porous silicon (PSi) platforms. PSi was first discovered at Bell Laboratories in the mid-1950s [38], but it wasn't until thirty years later that its sensing properties were discovered by Tobias and coworkers [12]. Tobias' sensor measured atmospheric humidity by monitoring changes in the capacitance of the PSi layer when water molecules were adsorbed into the porous matrix. Other transduction mechanisms for sensing in PSi include changes in resistance [21, 23, 24], optical reflectivity [20, 22], and luminescence [13–18, 27, 28]. These changes are due mainly to modifications in the surface chemistry [27]; they often arise from adsorption, oxidation, or other chemical reactions with elements in the atmosphere. PSi is now considered an attractive material for vapor sensing applications because of its rich chemistry [111] and large surface area. The detection of many different analytes, including water vapor [23], alcohols [180], volatile organic compounds [14, 181, 182], polycyclic aromatic hydrocarbons [130], explosives [183], DNA [184, 185], and proteins [186] have been demonstrated. Luminescence-based sensing, in particular, is attractive because it is commonly employed in biological systems as a non-destructive, in-situ, and analyte-specific method for assaying the location and concentrations of the chemical species of interest [105].

While the sensing properties of luminescent PSi are well-established, some fundamental challenges hinder the development of sensor packages. One obstacle is that PSi must be etched from a silicon wafer; this imposes topological constraints owing to the planar geometry. PSi also suffers from short-term oxidative effects and chemical degradation in air, which lead to eventual quenching of the luminescence [62]. Additionally, PSi is mechanically fragile [187] and can require special treatments (*e.g.*, protective coatings [188]) to increase its mechanical strength.

Freestanding Si-QDs (FS-Si-QDs), *i.e.*, Si-QDs that are physically separated from a supporting matrix, are a potential alternative that offers many of the advantageous

properties of PSi while addressing some of the deficiencies. FS-Si-QDs can be processed and functionalized in a separate solution-based process, then deposited onto the desired region of a sensing device [31]. They have large surface areas and the surface chemistry should, in principle, be similar to that of PSi. Unlike the case for PSi, the FS-Si-QDs can be supported on robust and even flexible platforms; as well, they can be used on non-planar optical components, such as optical fibers and microcavities. In this work, we develop FS-Si-QDs for sensing of alcohols and water vapor. The method is based on an orders-of-magnitude increase in the photoluminescence intensity when these QDs are exposed to various atmospheres while irradiated with blue light from an LED or diode laser. This process can be termed "photoactivation" [125]. The effects of different vapor compounds and the specificity of the sensing method will be described herein.

4.2 Experimental

4.2.1 Preparation of the FS-Si-QDs

FS-Si-QDs were prepared using a fast-etching variation of a previously reported synthesis technique [30, 125]. In this method, hydrogen silsesquioxane (HSQ: chemical formula $H_{12}Si_8O_{12}$) is heated to 1100 °C under a 95% Ar + 5% H_2 atmosphere to produce a powder of Si-QDs embedded in a silica matrix. The annealed powder was mechanically pulverized using a mortar and pestle. The Si-QDs were subsequently freed from the silica matrix by HF etching. Approximately 0.25 g of composite was mixed with 0.2 mL of HCl (36.5% HCl) and 7.5 mL of HF (49% HF) for 10 minutes. Finally, a further 5 minute etch was performed in the same solution with the addition of 5.0 mL of ethanol (95% EtOH). This process removes the SiO_2 matrix and yields hydride terminated FS-Si-QDs. The suspended QDs were then extracted into 30 mL of toluene [111], and stored in an Argon glove box. FS-Si-QDs were subsequently cast onto silicon wafers, and the toluene was evaporated. This method yielded a coating of FS-Si-QDs on the surface of the Si wafer.

4.2.2 TEM Characterization

TEM characterization was performed in order to estimate the particle size distribution. Samples were prepared for transmission electron microscopy (TEM) by dropping a small fraction of the toluene solution containing the FS-Si-QDs onto a 400 mesh copper grid with a 16-nm-thick carbon support film. Bright-field imaging and electron diffraction were performed on a JEOL 2010 TEM with a LaB_6 filament. High-resolution imaging employed a JEOL field emission 2200FS TEM. TEM characterization was employed to verify the size, shape and composition of the FS-Si-QDs.

4.2.3 Photoluminescence

The FS-Si-QD photoluminescence (PL) was obtained by pumping the sample with 445 nm light from a solid-state GaN laser operated at a continuous wave power of ∼650 mW. This also supplied the radiant energy necessary for photoactivation. The PL experiments were performed in a sealed gas chamber, with the laser light entering through a quartz window and the PL collected *via* an optical fiber threaded into the chamber. The luminescence was analyzed with a CCD spectrometer calibrated with a standard blackbody source (for intensity) and an HgAr source (for wavelength).

Photoactivation experiments were performed by pumping the QDs using the 445-nm laser, in the presence of various gas vapors. The PL spectra were collected at 10-second intervals over a period of 60 minutes. The chamber was supplied with analyte vapors by passing pressurized O_2 (g) (99.993% purity) through a standard bubbler and then into the sample chamber. Experiments were conducted using water, ethanol (CH_3CH_2OH), methanol (CH_3OH), isopropanol ($(CH_3)_2CHOH$), butanol (*n*-butanol: $(CH_3)CH_2CH_2CH_2OH$), or butanediol (1,4-butanediol: $HOCH_2CH_2CH_2CH_2CH_2OH$) in the bubbler. Since we have no direct way to measure the vapor concentrations for all examples except water, we assumed that the vapor concentration from the bubbler was at the room-temperature saturation level.

Photoluminescence lifetime experiments were conducted using the same gas chamber, using water vapor in the bubbler. The 488-nm line of an Ar-ion laser was "chopped" using an acousto-optic modulator (system response time ∼1 ns) at a duty

cycle and repetition rate of 50% and 1 kHz, respectively. The average power on the sample was ∼40 mW. While the Si-QDs photoactivate under blue-light irradiation (as discussed further below) the use of a longer wavelength and low powers minimizes the level of photoactivation that occurs over the ∼5-minute collection time needed to generate a lifetime curve. Between measurements, the QDs were photoactivated for 5 minutes using the 445-nm line of the diode laser, at an incident power of ∼650 mW.

4.2.4 FTIR Characterization

FTIR spectra were acquired using a Thermo Nicolet Nic-Plan FTIR microscope attached to a Magna 750 main bench with a wavelength resolution of 4 cm^{-1} and a spectral range of 4000–650 cm^{-1}. The FS-Si-QDs were cast onto a low-background potassium bromide plate for analysis. Thirty-two scans were taken per spectrum and averaged to improve the signal-to-noise ratio. Several samples were analyzed: (i) a control sample without photoactivation; (ii) a sample activated in room air at ∼40% relative humidity; (iii) a sample activated in 100% relative humidity; and (iv) a sample activated in ethanol vapor.

4.3 Results and Discussion

4.3.1 Microstructure

The synthetic method outlined in Sec. 4.2 produces silicon quantum dots with a lognormally distributed mean diameter and standard deviation of 3.3 and 1.2 nm, respectively (Fig. 4.1). The QDs tended to coagulate upon drying on the carbon film of the TEM copper grid, but in several areas well isolated QDs were found. In fact, clustering has been cited as one of the most serious challenges in obtaining uniform dispersions of quantum dots [189]; in some cases methods to better disperse the QDs have been developed. Here no efforts were made to reduce agglomeration.

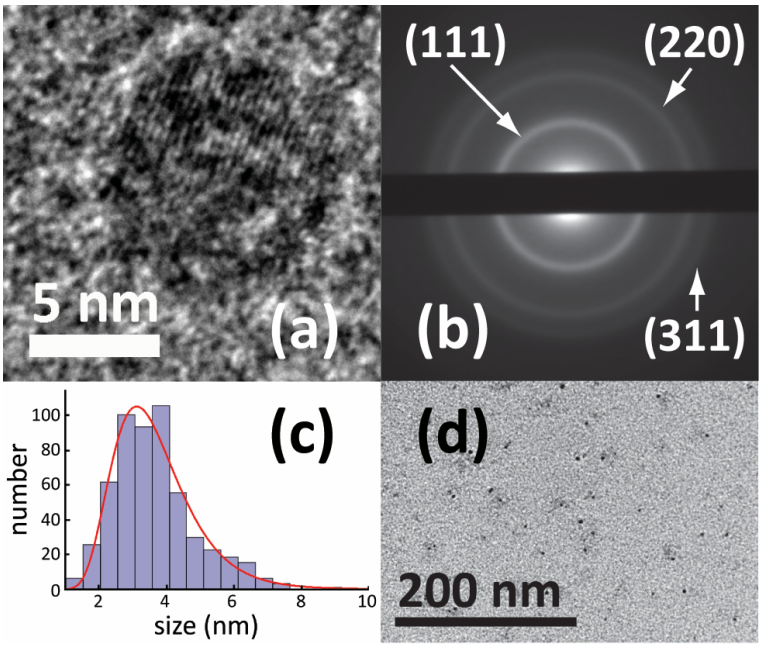

Figure 4.1. (a) HRTEM image showing an individual FS-Si-QD with Si lattice fringes visible; (b) Diffraction pattern indicative of crystalline silicon (c) Size distribution (obtained by visual measurements using image processing software) of FS-Si-QDs prepared by the fast-etch method (d) Low-magnification TEM image showing distribution of FS-Si-QDs on a thin carbon film.

4.3.2 Fourier Transform Infrared Spectroscopy

FTIR spectroscopy can be used to determine the nature of the silicon surface species [94, 139, 189]. We observed several clear changes in the FTIR spectra upon exposure to water and ethanol vapors. Initially, the spectrum has a large Si–H_x stretch at 2080 and 2100 cm^{-1} and Si–H_x bend-wag vibrations at 905 cm^{-1} (Fig. 4.2), implying that the surface is mainly hydride terminated [94]. After photoactivation in water or ethanol vapor by irradiation for 60 minutes in 100% humidity, the Si–H-related vibrations decreased in intensity, while an Si–O–Si signature at 1150 cm^{-1} and Si–O–H signatures at 2240 cm^{-1} and 3300 cm^{-1} increased in intensity [165]; eventually dominating the FTIR spectrum. While the absolute magnitude of the absorption bands cannot be directly compared owing to sample non-uniformities (QD layer thickness, *etc.*), in the FTIR spectrum acquired from samples activated in ethanol the Si–O–Si signal was especially large relative to the other features in the spectrum.

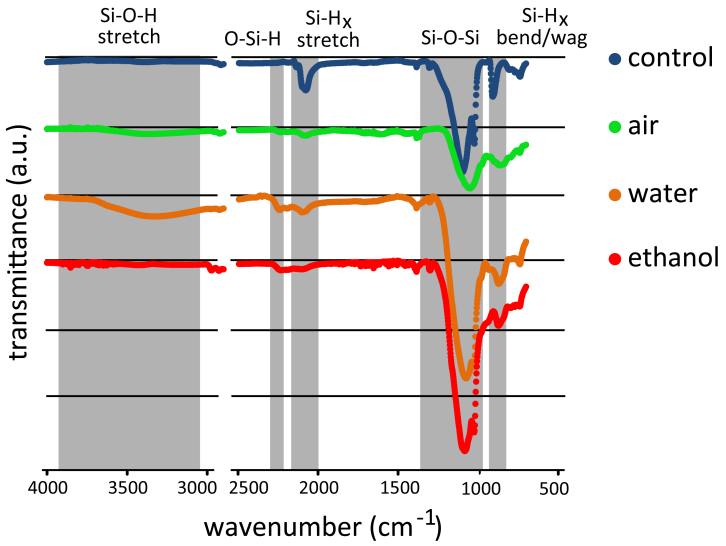

Figure 4.2. FTIR spectra for four samples: a control (as deposited, and not photoactivated), a sample partially photoactivated in air, a sample "completely" photoactivated in water vapor (*i.e.*, this sample reached maximum luminescence intensity), and a sample completely photoactivated in ethanol vapor.

4.3.3 Photoluminescence Lifetimes

The luminescence lifetimes evolved during photoactivation in oxygen carrying 100% water humidity at 300 K (Fig. 4.3). The decays were of the stretched exponential form $I = I_0 * exp[-(t/\tau)^{\beta}]$ typical of emissive centers with a distribution of lifetimes. With increasing photoactivation time, the values of τ and β increased monotonically, with the lifetime gradually changing from 320 ns to 47 μs. These latter values are somewhat larger than we reported previously, again likely owing to the differences in the preparation methods (*i.e.*, fast etch vs. slow etch). The exponent β also increases monotonically, suggesting an overall narrowing of the lifetime distribution [136].

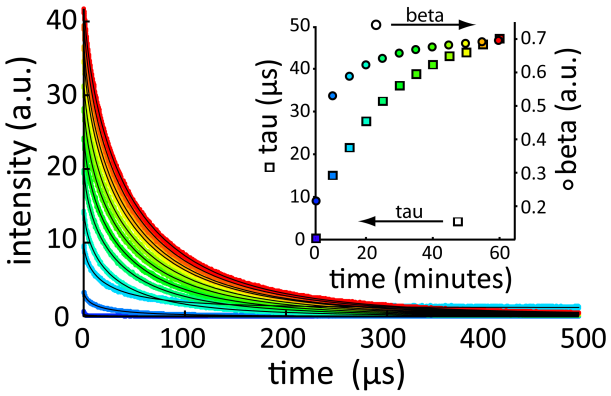

Figure 4.3. Photoluminescence decays of the FS-Si-QDs for different photoactivation times at 99.9% relative humidity (blue to red in 5 minute irradiation increments). Inset shows the corresponding changes in tau (τ) and beta (β). The time constant τ is shown on the left-hand axis, and β is on the right-hand axis.

4.3.4 Photoluminescence Spectroscopy

The luminescence intensity increased under exposure to all of the following compounds in an oxygen carrier gas: water, ethanol, methanol, isopropanol, butanol and butanediol. For all compounds tested, the luminescence intensity increased strongly under irradiation for 60 minutes (flux $\sim 65\ W \bullet cm^{-2}$). Example spectra are shown for ethanol and water in Fig. 4.4(a,b). The peak wavelength (as determined by Gaussian fits to the PL spectra) shifted monotonically to shorter wavelengths; initially the shift was relatively fast but it gradually slowed over time as the intensity approached saturation. Whereas the overall intensity for water vapor increased toward saturation, for the case of ethanol there was a subsequent bleaching effect after the peak intensity had been reached.

This behavior is different from a previous investigation performed when we first observed these effects, in which a smaller photoactivation magnitude and a slightly different spectral shifting behavior were observed [163]. The main difference between this and the previous synthesis process is the fast etch used here, and the much higher excitation power used to pump the QDs. In the present case, the resulting size distribution has a somewhat larger lognormal mean, and the overall emission wavelengths are also slightly longer. This is generally consistent with the quantum size effect, except of course in the present case the emission wavelength is coincident

with the formation of a surface oxide, as observed in the FTIR results. Even if the origin of the emission is not purely quantum confinement, the radiative emission sub-gap centers can track the size dependence of the overall bandgap [62]. Another effect we observed that could cause the differences between this and the previous work is that the response can be highly dependent on the thickness of the QD film. At this stage, we found significant sample-to-sample variability. We think this issue could be rectified if thinner, more consistent films could be produced.

The photoactivation rate is clearly different for ethanol, as compared to water. For these high excitation powers, the process occurs more quickly in the ethanol atmosphere, as can be observed in Fig. 4.4(a-c), in which the spectra are color-coordinated to indicate photoactivation time. Although not observable on the timescale in Fig. 4.4c, over the initial few minutes the intensity increase followed a sigmoidal-like rise for the ethanol exposure. The overall activation behavior depends on the excitation power used to pump the QDs, so all experiments presented here were performed under similar conditions. Absolute final intensities cannot easily be compared because of sample non-uniformities (*i.e.*, number of QDs exposed to the laser beam, thickness of the QD film). We are working on new deposition methods to try to get more consistent uniformity between different samples.

The results summarized in Fig. 4.4c show the integrated normalized spectral intensity as a function of time for both atmospheres, as well as for dry O_2. If we assume the activation mechanism is governed by a single rate constant, it can be modeled to a first approximation as an exponential (Fig. 4.4c). The rise time in ethanol was found to be $\sim$41 seconds; while for water it was over ten times longer, at $\sim$558 seconds. For comparison, Fig. 4.4c also shows the effect for a sample activated in O_2; in this case there is little change in the PL intensity. As expected, the fits were better if a stretched exponential model was employed; however, at this point we felt that a more direct comparison can be obtained using the simpler single-exponential fit. At this point, we stress that the activation times depend on the excitation power density, so the values found here can not directly be applied to different pump powers, spot sizes, and pump wavelengths.

Finally, in Fig. 4.4d we present the photoactivation rise time constants for methanol, ethanol, isopropanol, butanol, butandiol, and water, plotted vs. the saturation va-

por concentration. There was a general trend toward decreasing activation time as a function of vapor concentration. If the trend were perfectly linear, then the sensor response would lack chemical sensitivity to the vapor species, and only measure vapor concentration. However, as there is considerable variation, the photoactivation rate does depend on the chemical species also. This interpretation is consistent with the FTIR data for water and ethanol, which are clearly not identical. In the case of PSi, others have found that the vapor sensitivity (measured as a small luminescence decrease) increases as the length of the carbon chain decreases [180]. We observe a roughly similar trend but with some exceptions: for example, the rise time is faster for ethanol than for the smaller methanol molecule. Nevertheless, we think that at this point, sample-to-sample QD film thickness variations could cause significant scatter in the data; this is probably the most important issue that needs to be solved before these particles could be used as a more reliable and specific gas sensor.

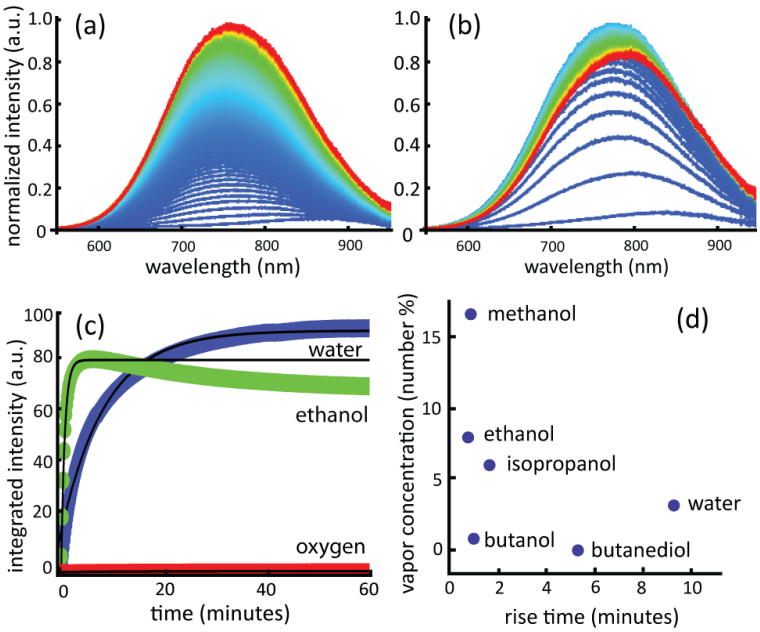

Figure 4.4. Time evolution of the photoluminescence spectra from FS-Si-QDs in saturated water (a) and ethanol (b) at 300 K, with an O_2 carrier gas. The spectra are color coded from blue to red in 30 s intervals. The intensities are normalized for comparative purposes. (c) Intensity as a function of time, shown with fits to an exponential function. Activation in dry oxygen is included as a baseline for comparison. (d) Photoactivation rise times as a function of vapor concentration for various alcohols.

4.3.5 Mechanisms

A two-step physical process is generally consistent with the observed FTIR, luminescence lifetime, and photoactivation results. In the first step, the initially hydride-terminated surface bonds on the Si-QDs are removed. This process is enhanced by irradiation and the presence of OH-bearing vapors in the atmosphere. The experimental evidence in favor of this initial step includes: (i) the Si–H bond vibration energies decrease after only a short irradiation time; (ii) there is a short-term and sudden decrease in the luminescence intensity immediately after exposure to blue light prior to the main photoactivation effect. This feature is consistent with the formation of a fast non-radiative trap such as the dangling bond left behind upon removal of hydrogen; and (iii) our previous observation that the luminescence lifetimes decrease over the interval corresponding to the initial short-term decrease in the intensity [163]. Thus, the first step may be Si–H bond breaking, leaving behind non-radiative dangling bonds (*i.e.*, the so-called P_b centers) [166].

The second step in the photoactivation process is surface oxidation and hydration. Direct oxidation without requiring an initial P_b-center formation is also possible, but in bulk silicon the availability of an OH-terminated species (*i.e.*, water vapor and alcohols) in the atmosphere increases the rate of the surface oxidation process [17]. The result is the development of Si–O and Si–OH surface bonding configurations. This interpretation is consistent with the FTIR results that show an increasing concentration of both types of bonds as the photoactivation proceeds. This removes any non-radiative centers from the Si-QD surfaces, thereby increasing the overall luminescence intensity.

Next, we comment briefly on the activation rates. Generally, an exponential behavior is consistent with the oxidation rate for silicon surfaces, at least to a depth of about 4 nm [190,191]. According to the FTIR results, the photoactivation mechanism is coincident with the formation of an oxide, so the exponential nature of the PL intensity increase may not be surprising. A preference toward a stretched exponential fitting function could occur due to the size distribution and sample preparation issues (*e.g.*, if some QDs are buried underneath others, thus lengthening the photoactivation time).

During the photoactivation process, there was also a gradual spectral blue-shifting of the luminescence peak wavelength. While the reason for this behavior cannot be determined unambiguously from these results, one hypothesis is that the surface oxidation and hydration slightly decrease the particle size and correspondingly increase the bandgap. If the emissive site is indeed a surface state, its energy could correspondingly increase slightly, as in the model for PSi [62]. While this two-step process (hydride bond-breaking followed by oxidation and hydration of dangling bonds) is consistent with all the present observations, future work, for example using electron spin resonance spectroscopy, may give additional information on the atomic-scale nature of the photoactivation mechanism.

Finally, we comment briefly on the reproducibility of these results. By repeating the experiments numerous times, we found that there are significant variations in the photoactivation behavior if the QDs are deposited in thick layers, compared to better-dispersed thin layers. One common characteristic of thicker samples is a failure to achieve saturation in the PL intensity; instead it continues to increase sublinearly. We hypothesize that this could be a result of "buried" QDs not receiving efficient exposure to the analyte vapor. In order to achieve good reproducibility, effort must be made to ensure that the deposited layers are as thin and dispersed as possible, while still giving sufficient overall PL intensity, and the excitation power density must remain constant.

4.4 Conclusions

Photoactivation is a surface effect in which the luminescence of freestanding silicon quantum dots evolves during irradiation in atmosphere containing water vapor or other alcohols. The mechanism is associated with hydride bond breaking, followed by oxidation and hydration of the quantum dot surface. The integrated luminescence intensity associated with the QDs can increase by orders of magnitude after the sample has been "fully" activated over a period of minutes to hours. The evolution of the luminescence and surface structure of the QDs was measured as a function of activation time in a variety of vapors. The rates associated with these processes depend on the concentration and type of analyte vapor in the surrounding atmosphere.

Currently, one requirement is that OH-terminated species must be present in order for the photoactivation rates to be appreciable.

While there have been numerous related investigations in PSi materials [180], the activation seen here is one of the strongest known; also, since it is based on freestanding particles that can be deposited on any surface the method may help to solve some of the mechanical issues facing the development of PSi sensor devices. However, some issues remain for further study. Currently, for example, while we have demonstrated that the photoactivation rate depends on the analyte vapor, we cannot claim specificity. Mixtures of different OH-terminated species would not, at this point, be determined unambiguously. The second issue concerns sample uniformity. We always see some degree of agglomeration when the QDs are dried on the wafer surface. This can lead to artifacts in the rise times, since QDs buried deeper within a "clump" would not necessarily see the same light intensity or local vapor concentration. In this work, we diluted the samples in order to minimize agglomeration and clumping; in future, chemical methods may also be explored.

4.5 Acknowledgements

The authors thank the National Science and Engineering Research Council and Alberta Innovates Technology Futures for funding this research. Kevin Van Der Meij and Teresa Sokolowski assisted with the data collection.

Chapter 5

Paper: Light-Induced Evolution of Silicon Quantum Dot Surface Chemistry – Implications for Photoluminescence, Sensing, and Reactivity

---

Abstract

The photoluminescence of freestanding silicon quantum dots (QDs) responds rapidly to various gases in the atmosphere. Under short wavelength irradiation, the luminescence can change over a timeframe of seconds to minutes, and can feature orders-of-magnitude shifts in the luminescence intensity and rapid "jumps" in the peak wavelength. Starting with hydride-terminated Si QDs, the luminescence can be reversibly quenched or strongly activated, leading to a partly reversible, three-state

luminescence condition consisting of regular, quenched, and activated states. These changes were characterized using photoluminescence spectroscopy, Fourier transform infrared spectroscopy, and electron spin resonance. The response is a multi-step process involving several stages, including energy transfer, abstraction of hydrogen, and rapid optical-irradiation-assisted oxidation. These properties make freestanding Si QDs a potentially attractive material for optical sensor applications.

5.1 Introduction

The photoluminescence of porous silicon (PSi) can be modified upon exposure to different of atmospheric vapors [7]. For example, when exposed to alcohols [17, 27, 127, 192], hydrocarbons [180], a variety of aromatic compounds [130], explosives [183], or water vapor [127], the luminescence of PSi reversibly quenches and can be recovered after the adsorbed species has been removed. The quenching mechanism can occur either as a result of energy transfer to adsorbed molecules, or *via* the enhanced effects of interface traps in the presence of the adsorbed species [193]. This reversible quenching property could potentially serve as a basis for new solid-state gas sensor platforms [14–17, 20, 27], although questions of specificity and detection limits are still being explored.

In contrast to these effects, slow oxidation can lead to a gradual (*i.e.*, weeks to months) evolution in the luminescence intensity and wavelength [15, 87, 129, 138, 194, 195]. The effect of oxidation seems to vary considerably depending on the PSi substructure. Several authors report that the luminescence intensity of hydrogen-terminated PSi gradually decreases upon oxidation [16,18,19,130]. Conversely, others find a slow increase in peak PL intensity upon long-term exposure to air [196,197] or deionized water [198]. Oxidation-induced shifting of the PL spectral maximum is also common. Much work has aimed to elucidate the mechanisms responsible for these changes, and various oxide structures including Si=O double bonds (although the existence of a stable form of this structure has not been proven [79]) and ≡Si–O–Si≡ bridges are generally thought to produce radiative sub-gap energy levels in the 700-800 nm spectral region [62]. Conversely, the silicon dangling bond, or "P_b center" (≡Si$^\bullet$) is widely accepted to be the most common non-radiative trap [82, 85].

Freestanding silicon quantum dots (Si-QDs) are broadly similar to PSi but lack the extensive crystalline backbone. Like PSi, freestanding Si-QDs have a chemically available surface suitable for functionalization [112, 141, 199, 200]. We recently showed that hydrogen-terminated Si-QDs [30, 133], can demonstrate a strong photoactivation (PA) effect, (*i.e.*, rapid increase in the luminescence intensity that occurs upon exposure to short wavelength light) in ambient air [125]. This characteristic could make Si-QDs appealing as active materials in fiber-optic sensors for water or alcohol vapors [127]. If practical sensors are to be realized, however, the surface mechanisms responsible for the PA effect should be elucidated. The requirement for short-wavelength blue or UV light irradiation suggests an activated process beginning with Si–H bond cleavage, but the origin of the unusually strong increase in the reported PL intensity, which can occur within a timeframe as short as a few seconds, is not well understood.

The objective of the present work is to investigate the evolution of the Si-QD surface structure at various stages of the PA process. This permits the development of the surface structures to be measured as the PL intensity changes over a single experiment. The primary methods employed are PL spectroscopy, electron spin resonance (ESR), and Fourier transform infrared spectroscopy (FTIR). The latter two methods have been widely used for studying the surface of bulk Si-SiO_2 interfaces [84,91,92,147] as well as PSi, and Si-QDs [85–89,94,95,111,139,140,201,202]. Thus, the origin of the FTIR and ESR signals in different parts of the corresponding spectra are reasonably well understood and can provide valuable information regarding the overall PA process.

5.2 Experimental Section

Freestanding hydrogen-terminated Si-QDs were obtained by chemically etching the product of a reductive thermal treatment of hydrogen silsesquioxane (HSQ) [199]. Briefly, HSQ was heated at 1100 °C for 1 hour under a slightly reducing atmosphere (*i.e.*, 95% N_2 + 5% H_2) yielding an amber solid consisting of a composite of Si-QDs embedded in a silicon oxide matrix. This composite was mechanically pulverized with a mortar and pestle to produce a fine red-brown powder that was etched in two

steps: i) an initial 10 minute etch in 0.2 mL HCl (36.5% aqueous HCl) and 7.5 mL HF (49% aqueous HF), ii) an additional 5 minute etch after adding 5.0 mL of ethanol (95% aqueous EtOH) to the original etching solution. The solution was mechanically stirred at a constant rate using a Teflon coated magnetic stir bar. Following etching, the resulting hydrogen-terminated Si-QDs were extracted into 30 mL of toluene and stored in an argon glovebox. Samples were prepared by drop coating the toluene QD solution onto silicon wafers (p-type, test grade) and allowing the solvent to evaporate slowly at room temperature. For FTIR experiments, KBr plates were used in place of the silicon wafers.

Photoactivation experiments were performed by exposing the Si-QDs to a 445 nm diode laser operated at a continuous wave power of ca. 900 mW, with the beam expanded to cover the $\sim$1 cm^2 surface of the sample ($\sim$9 mW/mm^2). During photoactivation, the QDs were maintained in a sealed chamber that facilitated controlled exposure to flowing gases. Ethanol exposure was accomplished by flowing a carrier gas (O_2 or Ar) through a liquid bubbler containing pure ethanol. The Si-QD photoluminescence was collected using an optical fiber coupled directly into the sample chamber and analyzed using an Ocean-Optics miniature spectrometer. The spectral efficiency was calibrated using an LS1 blackbody radiator from Ocean Optics.

Transmission electron microscopy was performed to characterize the particle size and shape. Bright field images and electron diffraction were done on free-standing Si-QDs deposited onto a home-made ($<$10 nm-thick) carbon-coated TEM grid, using a JEOL 2010 microscope with a LaB_6 filament. Electron diffraction had to be done in regions showing a dense agglomeration of particles in order to obtain diffraction "rings" of sufficient intensity for indexing. High-resolution and EELS imaging (centering the slit on the 99 eV Si L-3,2 edge) was done on a Hitachi HF 3000 STEM in order to further confirm the characteristic size and shape of the Si-QDs.

FTIR analyses were performed using a Thermo Nicolet Nic-Plan FTIR microscope attached to a Magna 750 main bench with a wavenumber resolution of 4 cm^{-1} over a range of 4000 to 650 cm^{-1}. Thirty-two scans were averaged per spectrum to reduce noise. ESR experiments were conducted on a Bruker EMX ESR spectrometer operating in the X-band (*i.e.*, at a frequency of 9.356116 $\pm$ 0.000001 GHz). The magnetic field strength was scanned from B =3300.62 G to 3360.62 G, using

a small-amplitude 100 kHz magnetic-field modulation to produce a first-derivative absorption spectrum.

Blank samples (as distinguished from the control sample to be described later) were subjected only to ambient atmosphere to quantify changes that might arise during the short periods needed to transport the QDs from the photoactivation setup to either the ESR or the FTIR apparatus, and to perform the analysis. The blanks (one for ESR and one for FTIR) were never photoactivated: the emitted PL was simply checked each time the FTIR/ESR sample came out of the apparatus and was used only to determine whether any changes had occurred during the time required to collect the ESR or FTIR data. Only minimal changes (*i.e.*, less than 1% PL intensity) were observed, so we conclude that the "extra" time in which the samples had to sit in ambient conditions for FTIR or ESR experiments did not appreciably affect the data.

An approximate method to calculate the number of spins in the Si-QDs was undertaken, in order to estimate the defect concentration. The "weak pitch" standard consisted of a mixture of 0.00033% standard pitch (nominally 10^{13} spins per cm^3; sample # 01012W111 from Bruker Inc.) in KCl packed in an ESR tube. A dilute mixture of Si-QDs and silicon monoxide (SiO) was prepared by mixing 0.0051 g of Si-QDs embedded in SiO_2 (*i.e.*, the un-etched powder) and 0.1960 g of SiO which was thoroughly ground and mixed for an hour. The mixture was filled into a tube identical to that containing weak pitch and packed by vibration until all air gaps were removed. The final length of the sample was 3.2 cm. The ESR spectra for both weak pitch and the Si-QDs/SiO mixture were measured under identical conditions. This provides a baseline for an approximate spin quantification of the present samples.

5.3 Results and Discussion

5.3.1 Basic Characterization: TEM and Photoluminescence

TEM analysis and electron diffraction confirmed the presence of Si QDs from solutions drop-coated onto TEM grids (Fig. 5.1). All particles observed were between 2 and 7 nm in diameter and appeared roughly circular in shape although facets and occasional twinning could be observed in some particles. A count of 100 particles

yielded a mean diameter of 3.2 nm, which, despite the uncertainties in ascertaining the exact "edge" of the particles, is reasonably close to the value of 3.1 nm reported previously for similarly-prepared Si-QDs [125].

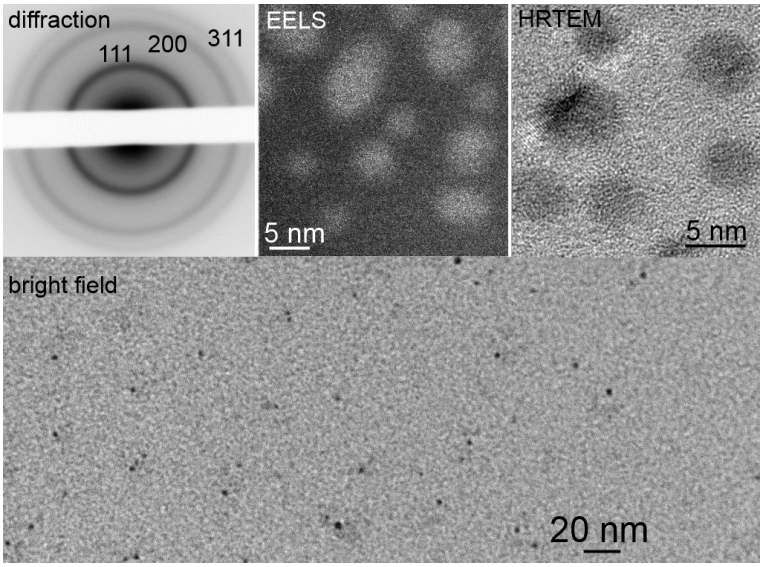

Figure 5.1. TEM characterization of the Si-QDs. The main (lower) panel is a bright field image, in which the QDs appear as dark dots. The panels across the top show, in order: Left: an electron diffraction pattern characteristic of randomly-oriented silicon nanoparticles with the three strongest lines indexed; Center: an EELS image taken with the slit centered at the characteristic 99 eV energy loss Si L-3,2 edge, in which the QDs have light contrast; Right: a high-resolution image in which the 3.4 eV lattice spacing characteristic of the silicon (111) plane could be measured.

The PL was initially weak and the spectrum was asymmetric and skewed toward shorter wavelengths. The low-intensity spectrum shown in Fig. 5.2 is already after 100 s photoactivation time; initial spectra were even weaker. Previous studies of ensembles of Si-QDs showed that a skew-normal function can optimally fit the spectra [73], and can arise naturally due to volume diffusion processes occurring as the particles ripen and grow during the annealing stage [203]. Of course, in the present case the spectrum cannot be expected to exactly follow the size distribution (clearly it does not, since it strongly evolves over time while the particles showed no change evident in the TEM images before and after irradiation). Nevertheless, the skew-normal distribution provides an excellent visual fit and can readily handle the observed skewing, so we proceed with this function. After photoactivation for 50

minutes in flowing O_2 with saturated ethanol vapor, the intensity grew by a factor of ∼100, the peak shifted towards slightly shorter wavelength, and the spectrum became more symmetrical (Fig. 5.2).

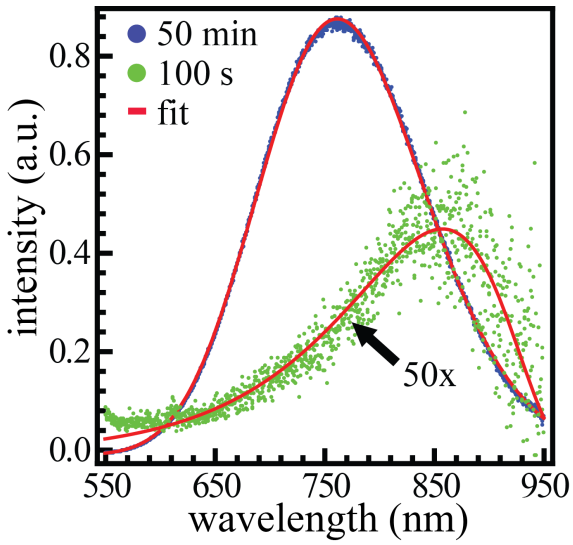

Figure 5.2. Photoluminescence spectra of a sample of Si-QDs, taken after 100 seconds and 50 minutes of irradiation using a 445-nm laser, while the sample was exposed to ethanol + O_2. The data are fit with a skew-normal distribution (red lines). Intensities were extracted from the corresponding fitting parameters.

A more complete set of spectra taken every 5 seconds during the photoactivation process is shown in Fig. 5.3a. Under 445 nm laser irradiation in a saturated atmosphere consisting of ∼130 mg/L ethanol in flowing O_2 (using a liquid bubbler), the PL intensity increased by 2-3 orders of magnitude after a one-hour exposure. We term this the "photoactivation" process – a rapid and large increase in the PL intensity under O_2 + ethanol vapor during irradiation with blue light. The peak of the luminescence spectrum gradually shifted from ca. 890 to 770 nm during this period. The corresponding evolution of the integrated intensity and peak wavelength is shown by the solid blue line in Figures 5.3b and 5.3c, respectively.

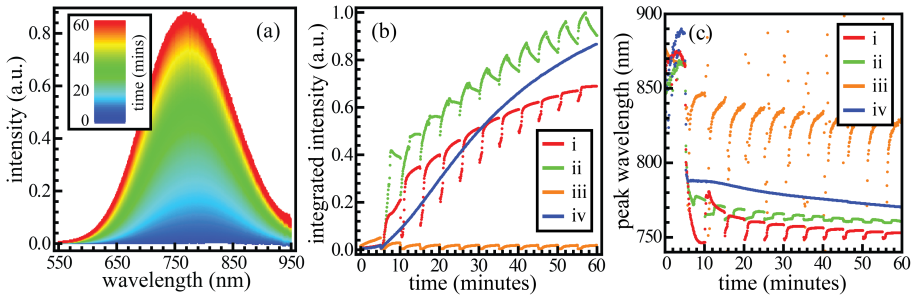

Figure 5.3. PL spectra of Si-QDs in 5-second sequential photoactivation steps. (a) Si-QD PL progression over one hour in an O_2 carrier gas saturated with ethanol. (b) Integrated intensity and (c) peak wavelength of Si-QD PL over one hour in (i) O_2 carrier gas with saturated ethanol vapor flowing every 5 minutes for 30 seconds, (ii) O_2 carrier gas with saturated ethanol vapor flowing every 5 minutes for 120 seconds, (iii) Ar carrier gas with saturated ethanol vapor flowing every 5 minutes for 30 seconds, and (iv) O_2 carrier gas with saturated ethanol vapor flowing continuously.

Some samples were exposed to either flowing O_2 or Ar with periodic "puffs" of ethanol vapor. When the QDs were exposed to 30-second ethanol vapor puff in an argon carrier gas, the intensity at first dropped rapidly as the ethanol vapor entered the chamber, only to recover to its original value a few minutes after the ethanol had been switched off (Fig. 5.3b). The response to ethanol vapor pulses was different when O_2 was used as the carrier gas. For 30-second pulses, the PL intensity initially dropped but quickly recovered to its original intensity and continued to increase considerably above the original value. For longer (*i.e.*, 120 second) ethanol pulses, the behavior was broadly similar (a momentary decrease, followed by a rapid recovery to higher intensities). However, after the first few pulses, the intensity showed additional evolution that involved a slight drop in PL intensity during the dry O_2 flow period. These effects are summarized in Fig. 5.3 b.

The location of the peak wavelength was monitored by fitting skew-normal curves to the PL spectra, as described above. The resulting peak locations are shown in Figure 5.1c. For reasons of clarity the fitting errors are not shown, but they are comparable to the point sizes after the first few minutes of irradiation. Initially when the PL intensity was low, the fitting tended to be relatively unstable and the resulting peak positions tended to fluctuate from measurement to measurement. However, as the PL intensity increased the fitting became more robust and the peak

wavelength evolution settled into a reproducible pattern, showing a sudden blue-shift each time ethanol vapors were introduced into the chamber, followed by a subsequent partial "recovery" during the oxidation stage. For all samples tested, there was also a slower irreversible blue-shift as the process continued.

5.3.2 FTIR Spectroscopy

The FTIR spectra of the as-prepared QDs show many characteristic features associated with the Si–H [204, 205], Si–O and Si–OH [138] -related vibrational modes (Fig. 5.4). During photoactivation in O_2 + ethanol, the Si–H_n scissoring mode at ca. 910 cm^{-1} and the Si–H wagging mode at ca. 650 cm^{-1} both disappeared (Fig. 5.4b). The Si–H_n stretching doublet at 2080-2120 cm^{-1} also decayed (Fig. 5.2f) and was eventually overwhelmed by the nearby Si–O–Si and H–Si–Si_{3-n}–O_n (n=1, 2, 3) features in the range of 2100-2300 cm^{-1} [206]. At the same time, the oxide-related vibrational mode signals increased considerably during photoactivation. The Si–OH absorption around 3300 cm^{-1} also increased nearly monotonically as the photoactivation process proceeded.

Some additional features are notable in the FTIR spectrum of the ethanol photoactivated sample. First, the features near 2900 cm^{-1} have been attributed to –CH_2/CH_3 modes arising from surface adsorbed ethanol [141]. While it isn't directly possible in the present experiments to distinguish between physisorbed [207, 208] vs. chemisorbed ethanol, the latter process is consistent with a photo-assisted hydrosilylation reaction proposed for PSi [209]. Similar chemisorption-related reactions in which alkenes and aldehyde groups chemisorb to PSi at elevated temperatures have also been previously characterized [210]. Second, the characteristic Si–O–Si stretching mode [211] at ca. 1100 cm^{-1} was present even in the as-prepared samples. This likely arises from a small quantity of oxide remaining after matrix liberation, consistent with some TEM images that occasionally showed an agglomeration of particles contained within remaining matrix material, and with the ESR results discussed below.

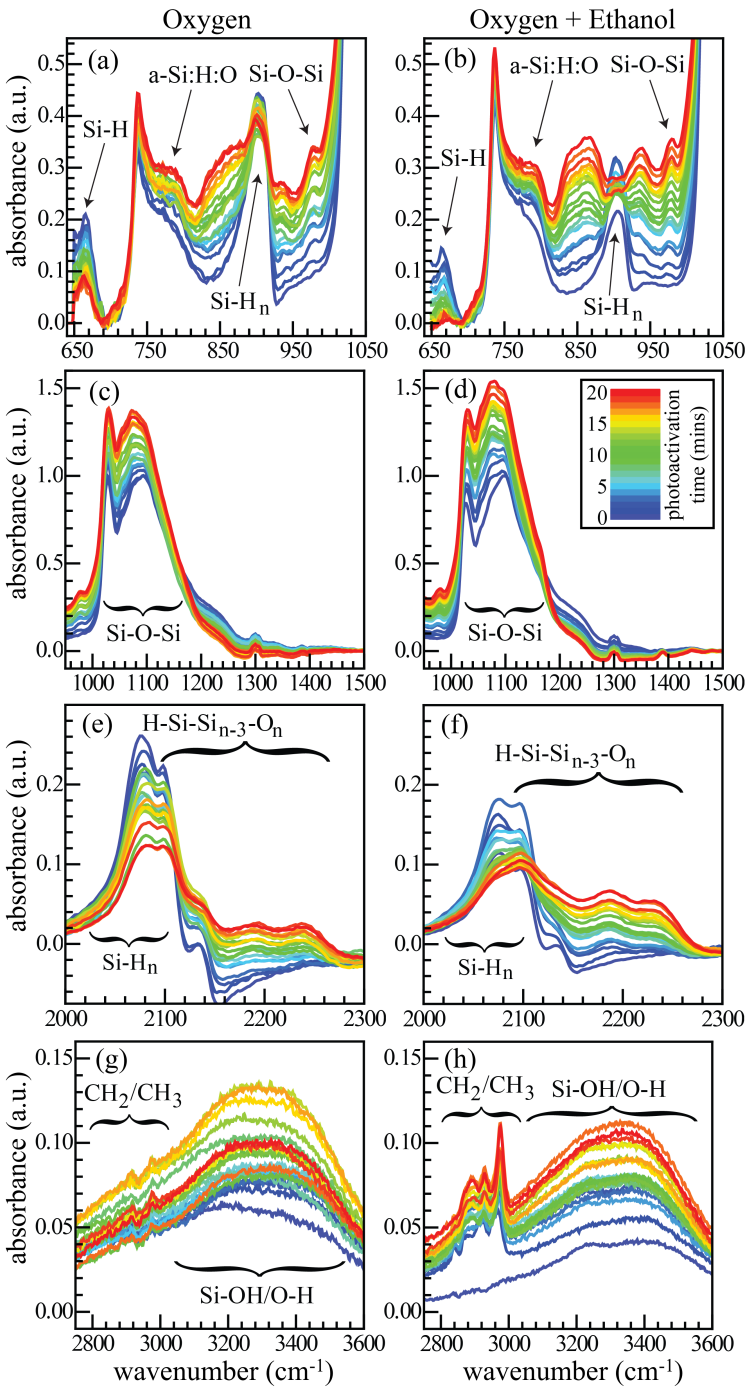

Figure 5.4. FTIR absorption spectra for Si-QDs in 1-minute sequential photoactivation steps in an oxygen (left column: a,c,e,g) and ethanol vapor (right column: b,d,f,h) environments. Relevant features are marked. Inset shows a color timescale.

For the FTIR data, we used a control sample to compare the effects of irradiation in ethanol vs. without ethanol. Analysis of the control sample (which was irradiated

in O_2 only) showed several key spectroscopic differences. First, the Si–H-related features decayed much more slowly under irradiation in O_2 (Fig. 5.4e), when compared to the case for ethanol + O_2, and they never completely disappeared. The absorption arising from the Si–H_n scissoring mode remained strong, although it began to overlap a nearby peak at ca. 850 cm^{-1}, which may be part of the growing Si–O–Si rocking mode [212] near 832 cm^{-1}. Second, while the oxide-related features increased in intensity, they did so more slowly for the control (O_2 only), as compared to the ethanol-photoactivated sample. Finally, there are no CH_n-related features observable for the control sample; whereas they are clearly present for the case of ethanol, as discussed above. The Si–OH related band [138] around 3350 cm^{-1} developed in both cases, but remained relatively weak and did not well differentiate the ethanol photoactivated sample from the control.

5.3.3 ESR Spectroscopy

A representative ESR derivative spectrum for a sample photoactivated in O_2 + ethanol shows a strong absorption in the g =2.005 region (Fig. 5.5), which is characteristic of the P_b defects [85,87,92,139]. In previous work [140], these defects were divided into three main sub-types: i) a P_b defect oriented parallel to a 111 surface normal ($g_{\|}$ ≈2.0015-2.0020); a P_b defect oriented perpendicular to a 111 surface normal ($g_{\perp}$ ≈ 2.0080-2.0090); and an isotropic D-center with g_D ≈2.0053. The "D-center" is attributed to the silicon dangling bond in a disordered environment, such as amorphous silicon-rich oxide [85,140,213]. It appears nontrivial to mathematically "fit" axially symmetric powder patterns, however, and the meaning of such fits would be difficult to ascertain without an error analysis associated with the various fitting parameters. For the purpose of the present investigation, we are mainly interested in what happens to the overall defect concentration as the photoactivation proceeds and less with the relative magnitudes of the individual Pb defect components. However, individual Gaussian or Lorentzian peak fitting did show a similar trend for both defects subtypes: a rapid rise in the first 20 min followed by a more gradual increase as the photoactivation proceeded.

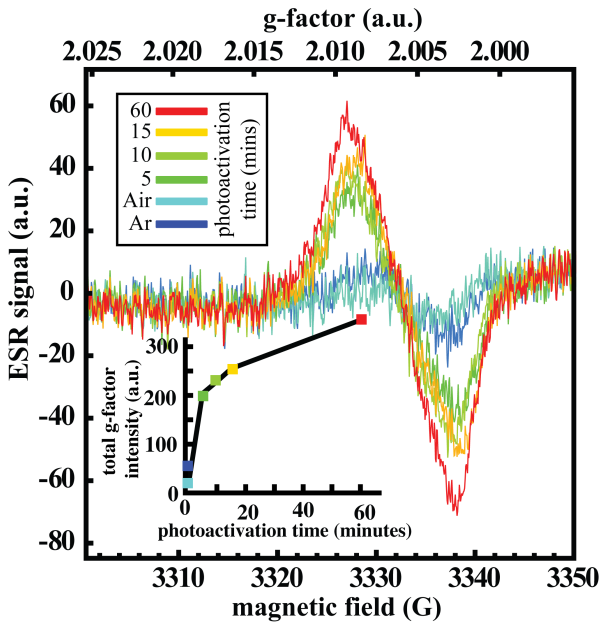

Figure 5.5. ESR spectra recorded with Si-QDs after 60 min of laser irradiation in an oxygen and ethanol vapor environment. The raw defect-related ESR intensity is shown in the inset, where "Air" and "Ar" refer to samples stored in air or argon, respectively, prior to photoactivation.

In the "as-etched" material, the ESR signal was low (and the Si–H-related FTIR features were prominent), suggesting that the surface of the QDs are initially passivated with hydrogen and have a relatively low defect concentration. The composites showed quite weak P_b defect signals prior to etching. Indeed, annealing at 1100 °C (*i.e.*, to produce the composites, as described earlier) is known to passivate oxide-related surface defects [92]; furthermore, HF etching ensures a reasonably well-passivated QD surface [214]. After 5 minutes air exposure (no irradiation), a small decrease in the ESR response was observed; this seems generally consistent with the results of Ref. [140], in which the P_b signals gradually decreased over a period of about a day. This was attributed to an ambient-oxidation-related decrease in the dangling bond concentration (*i.e.*, oxidation of pre-existing P_b centers). At this point, the intensity of the PL emission remained low.

Spectroscopic analysis of photoactivated QDs show several differences compared to that for the air-oxidized systems reported previously [140]. First, the ESR response increased strongly over the 1-hour photoactivation process (Fig. 5.5, inset). The same general effects were noted for the control sample (irradiated in O_2 only, as

described above); however, the magnitude of the ESR response was approximately 30% smaller. The increase in ESR signals happen orders of magnitude more quickly than for atmospheric oxidation (1 hour in our experiments versus 1000+ hours in Ref. [140]). Second, the ESR signal changed monotonically, initially quickly and then more slowly as the photoactivation proceeded, somewhat differently from the decreasing → increasing → decreasing cycle reported in Ref. [140]. Gradual monotonic shifts in $g_{\parallel}$ and $g_{\perp}$, the principal g-values for the P_b defect, were not observed, within the fitting error. Finally, the strength of the g_D signal is considerably stronger in the photoactivated samples (irradiation in O_2 + ethanol) than in the oxidized control (irradiation in O_2 only).

The number of defects per QD can be estimated by comparing the strength of the signals to the weak pitch standard described in the experimental section. In the initial un-etched (annealed and mechanically pulverized) sample (*i.e.*, Si-QDs still embedded in the glass matrix), the area under the absorption lines was four times that for the weak pitch standard. This yielded approximately 10^{15} spins per cm^3 in the sample, which is quite close to the estimated particle density assuming that the HSQ completely decomposed into Si-QDs and SiO_2 (yielding 33% Si-QDs by mole). Thus, we estimate roughly one defect per QD on average in the initial un-etched material. We cannot directly compare the magnitudes of the ESR absorption data for the freestanding Si-QDs to those for the un-etched sample since the data were taken at different times under different conditions; however, HF etching can passivate dangling bond defects [150]. Combined with the large increase in the ESR signal during the PA process, it seems likely that the defect concentration starts out at less than one per QD, and grows to a much larger value.

5.4 Discussion and Modeling

These results imply that hydride terminated freestanding Si-QDs have at least three different luminescence conditions, which one can call "normal" (as-prepared hydride terminated), quenched (after initial injection of ethanol vapor), and activated (after exposure to ethanol + oxygen). The normal-to-quenched transition is completely reversible, but the transition to the activated condition is not (the "cyclability" ob-

servable in the 2-minute O_2 + ethanol exposures (Fig. 5.1) will be discussed below; it does not continue indefinitely and is likely related to ongoing hydrogen loss). The activated condition is coincident with the development of strong surface-oxidation-related defect signals in the ESR data. Since the luminescence intensity increases concomitantly, the possible quenching effect associated with dangling bond defects is overwhelmed by the luminescence enhancement caused by surface oxidation of the Si-QDs.

The first response after introduction of ethanol vapor into the chamber is a quenching of PL over a period of a few seconds. This is similar to the quenching effect associated with liquid ethanol on a porous silicon surface [17], which was attributed to the trapping of charge carriers at the particle surface due to adsorbed polar molecules, followed by subsequent non-radiative decay. If Ar is the carrier gas, once the ethanol pulse stops, most of the adsorbed ethanol eventually desorbs from the surface. However, if oxygen is the carrier, the result is different. Ethanol + O_2 + blue light irradiation causes a rapid oxidation of the QD surfaces that starts just after the initial ethanol-related quench.

While the exact mechanism for the peak wavelength shifts under ethanol exposure is not unambiguously identifiable, the blue-shift that occurs simultaneously with the ethanol-related quenching could be a particle size effect. Larger QDs in the overall size distribution are more likely to be quenched, as a result of their greater surface area (per particle) and correspondingly greater chance to incorporate adsorbed ethanol. This would be similar to the blue-shift predicted [82] and found experimentally [215] and *via* simulation [163], for non-radiative defects in ensembles of particles. When the ethanol desorbs, the emission recovers its original characteristics. During the oxidation-related PA process, however, there is a gradual, irreversible evolution toward shorter wavelengths. This gradual blue-shift could relate to a "shrinking" of the core of the particle [74]. It may be also due to the formation of siloxene groups and related surface oxides that have been reported to luminesce strongly in the 750-nm range [56], although (in porous silicon) synchrotron studies suggest that luminescence may not derive from siloxene [78].

FS-Si-QDs exposed to a dry O_2 environment during irradiation (*i.e.*, the control sample) produced a small, gradual rise in the luminescence intensity. In contrast,

no detectable effects on the luminescence were observed under blue-light irradiation while the sample was exposed only to an inert environment (argon). Thus, it is likely that simultaneous irradiation and exposure to dry O_2 induces some hydrogen loss and surface oxidation, but evidently to a state with weaker luminescence intensity than the one formed during photoactivation with ethanol vapor.

Short-wavelength irradiation has been known for many years to accelerate hydrogen loss and oxidation of bulk silicon, which has been attributed in part to the electric field gradients caused by an irradiation-induced charge redistribution within the silicon near-surface region [216, 217]. Irradiation of PSi has also been found to cleave hydrogen from the particle surfaces, particularly for shorter irradiation wavelengths [129]. Although (bulk) Si–H bond energies are in the range of 2.8 to 3.9 eV [218], which is slightly larger than the photon energy used here, the presence of O_2 could assist the hydrogen abstraction process [131]. Energy transfer to adsorbed O_2 molecules in PSi has also been reported to produce the reactive singlet oxygen, which can enhance the oxidation rate during laser irradiation [219]. Many of the same basic mechanisms as those mentioned above probably happen to some degree in the photoactivation process reported in this work, and can provide a method for either strongly quenching or activating the QD luminescence.

The cyclability in the luminescence intensity found after a sufficiently long photoactivation in ethanol vapor is potentially interesting for sensing applications. This is most clearly noted in Fig. 5.3b(ii), where a decreasing PL intensity is apparent after the ethanol pulse is turned off. In order to further study this effect, a sample was photoactivated for 30 minutes in ethanol + O_2, and then the ethanol source was turned off. Consistent with the results in Fig. 5.3b, the intensity dropped by about 50% a few minutes after the ethanol flow had been stopped. We tentatively attribute this to the continuing abstraction of hydrogen from the silicon surfaces. This process appears to be enhanced when the surface is already at least partly oxidized in ethanol. The present FTIR results are consistent with this interpretation, showing that hydrogen removal cannot be completed even after extended exposures to dry O_2, but is rapidly removed after more complete oxidation during exposure to ethanol.

The observed PL switching is thus a result of several effects that can occur

simultaneously or in sequence (as illustrated in Fig. 5.6):

- Ethanol vapors are adsorbed on the Si-QD surface, quenching the PL intensity of un-oxidized Si-QDs. This step is reversible, analogous to the effects that occur in PSi [27], and in an inert atmosphere the PL returns close to its initial intensity after the ethanol vapor flow is closed (Fig. 5.6 (a-b)).

- Irradiation under dry O_2 facilitates the removal of hydrogen, leaving dangling bonds on the silicon surface. Even after long exposure, the Si–H related FTIR changes tend to saturate (*i.e.*, the Si–H signals never fully disappear), suggesting that it becomes increasingly difficult to remove additional hydrogen from an un-oxidized surface, (Fig. 5.6 (a) to (c)).

- Further irradiation under dry O_2 causes oxidation of surface P_b centers, leading to back-bonding on the Si-QD surface, (Fig. 5.6 (c) to (e)) [194]. Similar to bulk silicon, oxidation can occur under dry O_2 but the kinetics are slow [140].

- Injection of ethanol in the presence of O_2, under blue-light irradiation, causes a rapid oxidation of the surface, (Fig. 5.6 (b) to (d)). This is likely a multi-step mechanism similar to the Cabrera-Mott model proposed for slow, ambient oxidation [140]. The main effect of irradiation is to drastically increase the oxidation rate, similar to the case for bulk silicon [131]. During this stage, the oxide-related FTIR signals grow in intensity and the ESR signals also increase.

- When the ethanol pulse is stopped, the QD is partially oxidized. If the amount of oxidation is small (*i.e.*, after only a short exposure to ethanol), the main effect at this stage is a continuing gradual oxidation and a slow increase in the luminescence intensity. If the oxidation is already significantly completed, then the remaining surface hydrogen can be more easily removed, leading to a decrease in the PL intensity until the arrival of the next ethanol pulse (Fig. 5.6 (d) to (f)).

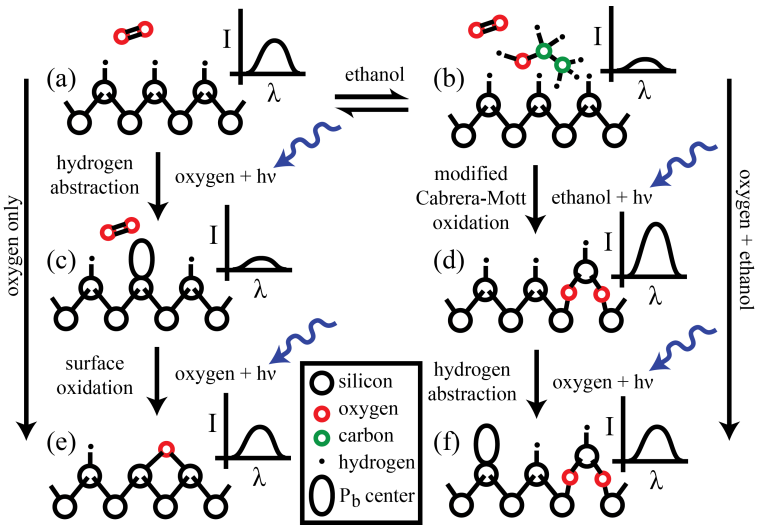

Figure 5.6. Proposed model of PL switching on the Si-QD surface. a) as-prepared hydrogen-terminated Si-QD surface with medium luminescence intensity, b) adsorbed ethanol on the Si-QD surface quenches the luminescence *via* energy-transfer, c) photon-mediated oxidation causes hydrogen abstraction on the Si-QD surface and quenches the luminescence due to the formation of P_b centers, d) a modified Cabrera-Mott mechanism breaks the silicon back-bonding by charge transfer from the hydroxide bond of the adsorbed ethanol, leading to the formation of an oxide with high luminescence intensity, e) photon-mediated oxidation of surface P_b centers leading to oxygen back-bonding and a relative increase in luminescence intensity, f) further photon-mediated hydrogen abstraction quenches the luminescence due to formation of P_b centers.

5.5 Concluding Remarks

The results show that the luminescence of Si-QDs responds rapidly to different environmental conditions under blue-light irradiation. Several processes occur in sequence or simultaneously, producing reversible or partly reversible changes in the PL intensity and central wavelength. The QD luminescence can switch between intermediate (mainly hydride-terminated), off (ethanol-quenched), or on (photoactivated) states. The photoactivated state is not truly reversible, but the intensity can still respond to periodic ethanol pulses until the surface becomes completely oxidized and all the hydride has been removed. Even where changes are not truly reversible, as during oxidation, they can evidently be cycled dozens of times before the response saturates. The PL response to gas exposure can be quite rapid (*i.e.*, seconds), suggesting potential applications of freestanding Si-QDs as rapid-response

environmental sensors. Since the QDs are freestanding and can be deposited on essentially any surface, fiber-optic sensors in particular might be fairly easy to realize [127].

Acknowledgements

The authors are grateful to W. Moffat and B. Mason for assistance with the FTIR and Dr. G. Schatte and K. Ramaswami for ESR data collection. X. Wang is thanked for the HRTEM and EELS images that were taken on the HF3000 instrument and R. Sinelnikov for weighing a sample for ESR quantification.

Chapter 6

Conclusion

The main objective of this work was to investigate FS-Si-QD photoluminescence in detail, to characterize the chemical composition of QDs as they undergo the process of photoactivation, and to outline the application of an optical sensor based on the luminescence of silicon quantum dots. The work began with a broad overview of the mechanisms associated with the QD photoluminescence, starting with first-principles and working towards the currently-accepted models. The chemistry of the surface-structures involved in the QD photoluminescence was also described, and the foundation laid for the interpretation of the experimental results detailed in the preceding chapters.

Methods used to fabricate FS-Si-QDs were detailed next, including the steps taken to prepare the samples for experiment. After fabrication, the Si-QDs were stabilized and stored in toluene under an inert atmosphere of argon, from which they were later taken for characterization and experiment. The experimental methods were described, with additional focus on the main methods as they apply to our understanding of QD interface structure. Brief descriptions of FTIR and ESR techniques were provided in order to show how the results were interpreted. Several of the methods employed apparatus that was built "in-house", which also required a more detailed explanation than is given in the paper-based chapters.

The main body of this thesis was composed of three first-authored publications, highlighting the results derived from the experimental and analytical work. Several aspects were investigated, beginning with the initial observation of the QD photoac-

tivation. PL spectral and lifetime data were first used to characterize the behavior of the QDs, but these studies identified phenomena that necessitated a more detailed analysis. The subsequent investigations produced a more detailed look at the properties of the free-standing Si-QDs and suggested the possible development of a silicon-QD-based sensor (described in Appendix A).

Chapter 3 discussed how the PL of silicon QDs changed in ambient conditions under various laser-irradiation wavelengths. The results showed that optical irradiation at wavelengths ranging from 325 to 514 nm produced an orders-of-magnitude increase in the overall PL intensity. We hypothesized that the removal of the hydride surface termination and subsequent oxidation were responsible for the observed changes, a conclusion supported by preliminary FTIR results. Investigations also included heating the samples both pre- and post-photoactivation; after heating, the PL intensity of the QDs was stabilized. Finally, the work illustrated how the quantum dots could be patterned into luminescent arrays, although the challenge of producing uniform and homogeneous films is still unresolved.

Chapter 4 discussed how the PL varied in controlled atmospheres of pure oxygen, and oxygen saturated with water vapors or vapors of various alcohols. The presence of OH-terminated species was identified as a requirement for the photoactivation rates to be appreciable, with pure-oxygen atmospheres resulting in little change to the overall PL intensity over the timescales investigated. Photoactivation rates were characterized by fitting the PL intensity as a function of time with an inverted stretched-exponential function, allowing indirect comparison between QDs photoactivated in various atmospheres. In this chapter, FTIR analysis was limited to samples that had been photoactivated for over an hour, but the results suggested that surface reconfiguration played an important role in the PA process.

Chapter 5 delved into more detailed chemical analysis, employing FTIR and ESR time-series data that were taken during FS-Si-QD photoactivation. These studies were used to propose a tentative model for the photoactivation process, and describe the structural changes as the PL evolved. This helped to relate data from FTIR and ESR analyses to the PL intensity, peak wavelength, and lifetime changes. This model and the associated experimental results suggest that FS-Si-QDs may have potential applications as environmental sensors.

Appendix A gives one example of an optical-fiber sensor based on these principles. The QDs applied to the end-facet of an optical fiber showed distinguishable responses in an oxygen atmosphere containing various combinations of water and alcohol vapors. In particular, reversibility, selectivity, and sensitivity were probed. Generally, it was discovered that the sensors could be cycled 30-times or more without a significant degradation in performance. Similar to the other studies, though, the non-uniformity of the QD films (*i.e.*, clumping, *etc.*) made it difficult to quantify both the specificity and detection limits. Finally, Appendix B is included to give an example of the Mathematica code that was used to analyze the time-series data.

To summarize, the important observations outlined in this work include:

- FS-Si-QDs exposed to short-wavelength laser irradiation in ambient atmosphere can undergo an exceptionally strong increase in PL intensity, a process called "photoactivation".

- Oxygen atmospheres containing vapors of water and various long-chain alcohols accelerate the photoactivation process.

- FTIR measurements during photoactivation indicate that Si–H structures on the Si-QDs decrease in number, while Si–O bond signatures increase rapidly.

- ESR measurements during photoactivation indicate that electronic defects on the Si-QDs also increase in number. This is contrary to a previous study of oxide-embedded Si-QDs [52] and illustrates the critical importance of oxidation in the QD photoluminescence.

- FS-Si-QDs can potentially be used as the sensing element in a QD-based sensor. A "prototype" QD-based fiber sensor was then reported.

Over the course of our investigations, we found that the QDs could sometimes respond differently in different experiments. For example, in Chapter 4, photoactivation of the QDs in the presence of ethanol vapor occurred more rapidly than it did in the presence of water vapor (Fig. 4.4 (c)). Water vapor also produced a more intense PL spectrum compared to ethanol vapor. In comparison, in Appendix A the opposite behavior appears, with PA of the QDs in ethanol increasing more slowly than

in water, but reaching a higher overall intensity (Fig. A.4). Possible explanations include:

1. Different power densities experienced by the QDs. On an optical fiber, the QDs would typically receive a photon flux significantly larger than they would during flat-wafer irradiation. Such differences could cause the QDs to respond differently [220].

2. Differences between samples prepared on the fiber tip *vs.* on silicon wafers. The distribution and clumping of QDs is probably quite different in the two cases (optical fibers *vs.* flat wafers). The fibers were simply dipped into the suspension and dried, whereas the wafers were drop-coated and blow dried.

3. Finally, differences between the "exposure geometries". For fiber-optic irradiation, vapors in the carrier gas must diffuse through the Si-QD layer to arrive at the source of optical irradiation on the fiber-tip; whereas, for free-space irradiation the QDs are exposed more directly. In other words, in fibers, the exposure to the vapor and to optical irradiation occur on opposite sides of the QD layer, but on a wafer they occur on the same side.

Additionally, in Chapters 3 and 4, PL lifetimes were observed to increase as a function of photoactivation time. In Chapter 5, the defect concentration associated with non-radiative processes also increased as a function of PA time. This is somewhat unusual, since an increasing defect concentration is usually related to lower intensity and shorter lifetimes, at least for oxide-embedded QDs [52]. One possible explanation is that the increase in luminescence intensity is a result of the formation of oxide-related luminescence states that trap carriers more efficiently than defect-related non-radiative states. As a result of this competition the PL lifetime and intensity may increase, despite the increasing defect concentrations.

Future Work

This thesis elucidated the chemical and structural changes that FS-Si-QDs can undergo under laser irradiation in selected atmospheres. Future directions may include the development of fiber-based sensors that are more selective to desired analytes

using various surface functionalization methods. The molecular signatures used in the manufacture of explosives (*e.g.,* nitrobenzene, dinitrotoluene, *etc.*), or vapors relevant to industrial applications (*e.g.* alcohols, sulfides, nitrides... *etc.*) are good candidates for further exploration. The first steps in this direction may include:

1. Real-time in-situ analysis of FS-Si-QD luminescence. Current methods take up to an hour to collect a single time-series dataset. The analyses that follow take several minutes to complete. Real-time analysis would take data directly from the spectrometer and send it to Mathematica (or other control software), effectively parallelizing data-collection and analysis. Clearly, for sensor applications live-time feedback is necessary, as opposed to waiting until the end of a long experiment before being able to evaluate the outcome.

2. Improved FS-Si-QD film quality. Currently, the evaporation of toluene from the FS-Si-QD/toluene suspension produces films consisting of highly agglomerated QDs. These inhomogeneities result in significant sample-to-sample variations.

3. Development of FS-Si-QDs with surface coatings that are selectively permeable to the desired analytes. This could be achieved by developing coatings that filter out large organic molecules through steric hinderance, or through direct chemical modification the surface of the QDs [221]. A second method could involve isolation of the FS-Si-QDs from all but the desired analytes, through the use of a semi-permeable membrane that filters out undesired molecular species. This effectively translates the selectivity away from the QDs themselves.

Free-standing silicon quantum dots may be a future tool for optical sensing applications, with the potential to become environmentally sensitive components in photonic circuits. A demonstration of the sensitivity of silicon-QD luminescence to the surrounding environment was reported, and the chemical mechanisms involved during the photoactivation process was described. While a FS-Si-QD-based sensor is one potential application of this research, there are many possible avenues for further exploration. This work represents another step in the development of silicon photonics and presents a glimpse into the possible future of quantum-dot based chemical sensors.

Bibliography

[1] W.F. Brinkman, D.E. Haggan, and W.W. Troutman. A history of the invention of the transistor and where it will lead us. *IEEE Journal of Solid-State Circuits*, 32(12):1858–1865, 1997.

[2] R.W. Keyes. Fundamental limits of silicon technology. *Proceedings of the IEEE*, 89(3):227–239, 2001.

[3] D.J. Frank. Power-constrained CMOS scaling limits. *IBM Journal of Research and Development*, 46:235–244, 2002.

[4] B. Jalali and S. Fathpour. Silicon photonics. *Journal of Lightwave Technology*, 24(12):4600–4615, 2006.

[5] J.R. Chelikowsky and M.L. Cohen. Electronic structure of silicon. *Physical Review B*, 10(12):5095–5107, 1974.

[6] D.J. Lockwood and L. Pavesi. Silicon fundamentals for photonics applications. *Topics in Applied Physics*, 94:1–52, 2004.

[7] L.T. Canham. Silicon quantum wire array fabrication by electrochemical and chemical dissolution of wafers. *Applied Physics Letters*, 57(10):1046–1048, 1990.

[8] S. Furukawa and T. Miyasato. Three-dimensional quantum well effects in ultrafine silicon particles. *Japanese Journal of Applied Physics*, 27(Part 2, No. 11):L2207–L2209, 1988.

[9] L. Pavesi, L. Dal Negro, C. Mazzoleni, G. Franzò, and F. Priolo. Optical gain in silicon nanocrystals. *Nature*, 408(6811):440–444, 2000.

[10] L. Canham. Gaining light from silicon. *Nature*, 408:411–412, 2000.

[11] J.-H. Park, L. Gu, G. von Maltzahn, E. Ruoslahti, S.N. Bhatia, and M.J. Sailor. Biodegradable luminescent porous silicon nanoparticles for in vivo applications. *Nature Materials*, 8(4):331–336, 2009.

[12] R.C. Anderson and R.S. Muller. Investigations of porous silicon for vapor sensing. *Sensors and Actuators A-Physical*, A21-A23:835–839, 1990.

[13] A.G. Cullis and L.T. Canham. Visible light emission due to quantum size effects in highly porous crystalline silicon. *Nature*, 353(6342):335–338, 1991.

[14] J.M. Lauerhaas, G.M. Credo, J.L. Heinrich, and M.J. Sailor. Reversible luminescence quenching of porous silicon by solvents. *Journal of the American Chemical Society*, 114(5):1911–1912, 1992.

[15] L.A. Balagurov, B.M. Leiferov, E.A. Petrova, A.F. Orlov, and E.M. Panasenko. Influence of water and alcohols on photoluminescence of porous silicon. *Journal of Applied Physics*, 79(9):7143–7147, 1996.

[16] J. Harper and M.J Sailor. Detection of nitric oxide and nitrogen dioxide with photoluminescent porous silicon. *Analytical Chemistry*, 68(21):3713–3717, 1996.

[17] M.J. Sailor and E.J. Lee. Surface chemistry of luminescent silicon nanocrystallites. *Advanced Materials*, 9(10):783–793, 1997.

[18] J.H. Song and M.J. Sailor. Functionalization of nanocrystalline porous silicon surfaces with aryllithium reagents: Formation of silicon-carbon bonds by cleavage of silicon-silicon bonds. *Journal of the American Chemical Society*, 120(10):2376–2381, 1998.

[19] J.H. Song and M.J. Sailor. Reaction of photoluminescent porous silicon surfaces with lithium reagents to form silicon-carbon bound surface species. *Inorganic Chemistry*, 38(7):1498–1503, 1999.

[20] H.K. Min and H.S. Yang. Extremely sensitive optical sensing of ethanol using porous silicon. *Sensors and Actuators B-Chemical*, 67:199–202, 2000.

[21] J. Das, S.M. Hossain, S. Chakraborty, and H. Saha. Role of parasitics in humidity sensing by porous silicon. *Sensors and Actuators A-Physical*, 94:44–52, 2001.

[22] F. Cunin, T.A. Schmedake, J.R. Link, Y.Y. Li, J. Koh, S.N. Bhatia, and M.J. Sailor. Biomolecular screening with encoded porous-silicon photonic crystals. *Nature Materials*, 1(1):39–41, 2002.

[23] G. Di Francia, A. Castaldo, E. Massera, I. Nasti, L. Quercia, and I. Rea. A very sensitive porous silicon based humidity sensor. *Sensors and Actuators B-Chemical*, 111:135–139, 2005.

[24] S.E. Lewis, J.R. DeBoer, J.L. Gole, and P.J. Hesketh. Sensitive, selective, and analytical improvements to a porous silicon gas sensor. *Sensors and Actuators B-Chemical*, 110(1):54–65, 2005.

[25] T. Islam and H. Saha. Study of long-term drift of a porous silicon humidity sensor and its compensation using ANN technique. *Sensors and Actuators A-Physical*, 133(2):472–479, 2007.

[26] L.Y. Li, Y.F. Dong, W.F. Jiang, H.F. Ji, and X.J. Li. High-performance capacitive humidity sensor based on silicon nanoporous pillar array. *Thin Solid Films*, 517(2):948–951, 2008.

[27] M.J. Sailor and E.C. Wu. Photoluminescence-based sensing with porous silicon films, microparticles, and nanoparticles. *Advanced Functional Materials*, 19(20):3195–3208, 2009.

[28] Z. Yuan, A. Anopchenko, N. Daldosso, R. Guider, D. Navarro-Urrios, A. Pitanti, R. Spano, and L. Pavesi. Silicon nanocrystals as an enabling material for silicon photonics. *Proceedings of the IEEE*, 97(7):1250–1268, 2009.

[29] T. Shimizu-Iwayama, T. Hama, D.E. Hole, and I.W. Boyd. Characteristic photoluminescence properties of Si nanocrystals in SiO_2 fabricated by ion implantation and annealing. *Solid-State Electronics*, 45:1487–1494, 2001.

[30] C.M. Hessel, E.J. Henderson, and J.G.C. Veinot. Hydrogen silsesquioxane: A molecular precursor for nanocrystalline Si-SiO_2 composites and freestanding hydride-surface-terminated silicon nanoparticles. *Chemistry of materials*, 18:6139–6146, 2006.

[31] J.G.C. Veinot. Synthesis, surface functionalization, and properties of freestanding silicon nanocrystals. *Chemical Communications*, 40:4160–4168, 2006.

[32] C.M. Gonzalez, M. Iqbal, M. Dasog, D.G. Piercey, R. Lockwood, T.M. Klapötke, and J.G.C. Veinot. Detection of high-energy compounds using photoluminescent silicon nanocrystal paper based sensors. *Nanoscale*, 6(5):2608–2612, 2014.

[33] J. Berzelius and H.G. Söderbaum. *Jac. Berzelius Lettres.* Almqvist & Wiksell, 1912.

[34] J.F. von Liebig and F. Wöhler. Jugend-erinnerungen eines chemikers. *Berichte der deutschen chemischen Gesellschaft*, 8(1):838–852, 1875.

[35] M.G. Voronkov. Silicon era. *Russian Journal of Applied Chemistry*, 84(7):371–378, 2007.

[36] J. Bardeen and W. Brattain. The transistor, a semi-conductor triode. *Physical Review*, 74(2):230–231, 1948.

[37] H. Herrmann and H. Herzer. Modern silicon technology. *Festkörperprobleme*, 15, 1975.

[38] A. Uhlir, Jr. Electrolytic shaping of germanium and silicon. *The Bell System Technical Journal*, March 1956.

[39] M.I.J. Beale, J.D. Benjamin, M.J. Uren, N.G. Chew, and A.G. Cullis. An experimental and theoretical study of the formation and microstructure of porous silicon. *Journal of Crystal Growth*, 73(3):622–636, 1985.

[40] L.G. Earwaker, J.P.G. Farr, P.E. Grzeszczyk, I. Sturland, and J.M. Keen. Analysis of porous silicon. *Nuclear Instruments and Methods in Physics Research Section B: Beam Interactions with Materials and Atoms*, 9(3):317–320, 1985.

[41] R.L. Smith, S.-F. Chuang, and S.D. Collins. A theoretical model of the formation morphologies of porous silicon. *Journal of Electronic Materials*, 17(6):533–541, 1988.

[42] A.G. Cullis, L.T. Canham, and P.D.J. Calcott. The structural and luminescence properties of porous silicon. *Journal of Applied Physics*, 82(3):909–965, 1997.

[43] J.M. Jasinski and S.M. Gates. Silicon chemical vapor deposition one step at a time: fundamental studies of silicon hydride chemistry. *Accounts of Chemical Research*, 24(1):9–15, 1991.

[44] J.G. Zhu, C.W. White, J.D. Budai, S.P. Withrow, and Y. Chen. Growth of Ge, Si, and SiGe nanocrystals in SiO_2 matrices. *Journal of Applied Physics*, 78(7):4386–4389, 1995.

[45] K.S. Min, K.V. Shcheglov, C.M. Yang, H.A. Atwater, M.L. Brongersma, and A. Polman. Defect-related versus excitonic visible light emission from ion beam synthesized Si nanocrystals in $PSiO_2$. *Applied Physics Letters*, 69:2033–2035, 1996.

[46] S. Hayashi, T. Nagareda, Y. Kanzawa, and K. Yamamoto. Photoluminescence of Si-rich SiO_2 films: Si clusters as luminescent centers. *Japanese Journal of Applied Physics*, 32(Part 1, No. 9A):3840–3845, 1993.

[47] Y. Kanzawa, T. Kageyama, S. Takeoka, M. Fujii, S. Hayashi, and K. Yamamoto. Size-dependent near-infrared photoluminescence spectra of Si nanocrystals embedded in SiO_2 matrices. *Solid State Communications*, 102(7):533–537, 1997.

[48] H. Morisaki, F. W. Ping, and H. Ono. Above-band-gap photoluminescence from Si fine particles with oxide shell. *Journal of Applied Physics*, 70(3):1869–1870, 1991.

[49] E. Werwa, A.A. Seraphin, L.A. Chiu, and C. Zhou. Synthesis and processing of silicon nanocrystallites using a pulsed laser ablation supersonic expansion method. *Applied Physics Letters*, 64(14):1821–1823, 1994.

[50] L.N. Dinh, L.L. Chase, M. Balooch, and L.J. Terminello. Photoluminescence of oxidized silicon nanoclusters deposited on the basal plane of graphite. *Applied Physics Letters*, 65:3111–3113, 1994.

[51] D. Riabinina, C. Durand, J. Margot, M. Chaker, G.A. Botton, and F. Rosei. Nucleation and growth of Si nanocrystals in an amorphous SiO_2 matrix. *Physical Review B*, 74(7):075334, 2006.

[52] B. Garrido Fernandez, M. Lopez, C. Garcia, A. Perez-Rodriguez, J.R. Morante, C. Bonafos, M. Carrada, and A. Claverie. Influence of average size and interface passivation on the spectral emission of Si nanocrystals embedded in SiO_2. *Journal of Applied Physics*, 91(2):798–807, 2002.

[53] G. Pearson and J. Bardeen. Electrical properties of pure silicon and silicon alloys containing boron and phosphorus. *Physical Review*, 75(5):865–883, 1949.

[54] C. Delerue, G. Allan, and M. Lannoo. Theoretical aspects of the luminescence of porous silicon. *Physical Review B*, 48(15):11024–11036, 1993.

[55] L. Pavesi. A review of the various approaches to a silicon laser. *Photonics Packaging and Integration III*, pages 206–220, 2003.

[56] M.S. Brandt, A. Breitschwerdt, H.D. Fuchs, A. Höpner, M. Rosenbauer, M. Stutzmann, and J. Weber. New growth technique for luminescent layers on silicon. *Applied Physics A Solids and Surfaces*, 54(6):567–569, 1992.

[57] S.M. Prokes. Light emission in thermally oxidized porous silicon: Evidence for oxide-related luminescence. *Applied Physics Letters*, 62(25):3244–3246, 1993.

[58] Y. Kanemitsu, T. Ogawa, K. Shiraishi, and K. Takeda. Visible photoluminescence from oxidized Si nanometer-sized spheres: Exciton confinement on a spherical shell. *Physical Review B*, 48(7):4883–4886, 1993.

[59] D.I. Kovalev, I.D. Yaroshetzkii, T. Muschik, V. Petrova-Koch, and F. Koch. Fast and slow visible luminescence bands of oxidized porous Si. *Applied Physics Letters*, 64(2):214–216, 1994.

[60] A.J. Kontkiewicz, A.M. Kontkiewicz, J. Siejka, S. Sen, G. Nowak, A.M. Hoff, P. Sakthivel, K. Ahmed, P. Mukherjee, S. Witanachchi, and J. Lagowski. Evidence that blue luminescence of oxidized porous silicon originates from SiO_2. *Applied Physics Letters*, 65(11):1436–1438, 1994.

[61] L. Tsybeskov, J. Vandyshev, and P. Fauchet. Blue emission in porous silicon: Oxygen-related photoluminescence. *Physical Review B*, 49(11):7821–7824, 1994.

[62] M. Wolkin, J. Jorne, P. Fauchet, G. Allan, and C. Delerue. Electronic states and luminescence in porous silicon quantum dots: The role of oxygen. *Physical Review Letters*, 82(1):197–200, 1999.

[63] A. Bagga, P.K. Chattopadhyay, and S. Ghosh. Stokes shift in quantum dots: Origin of dark exciton. pages 876–879, 2007.

[64] Jr. Bruchez, M. Semiconductor nanocrystals as fluorescent biological labels. *Science*, 281(5385):2013–2016, 1998.

[65] I.L. Medintz, H.T. Uyeda, E.R. Goldman, and H. Mattoussi. Quantum dot bioconjugates for imaging, labelling and sensing. *Nature Materials*, 4(6):435–446, 2005.

[66] A. Meldrum, K.S. Buchanan, and C.W. White. Effects of particle size and excitation spectrum on the photoluminescence of silicon nanocrystals formed by ion implantation. *Nuclear Instruments and Methods in Physics Research B*, 222:469–476, 2004.

[67] I. Vasiliev, J. Chelikowsky, and R. Martin. Surface oxidation effects on the optical properties of silicon nanocrystals. *Physical Review B*, 65(12):121302, 2002.

[68] J.S. Biteen, N.S. Lewis, H.A. Atwater, and A. Polman. Size-dependent oxygen-related electronic states in silicon nanocrystals. *Applied Physics Letters*, 84(26):5389–5391, 2004.

[69] S.V. Gaponenko. *Optical Properties of Semiconductor Nanocrystals*. Cambridge Studies in Modern Optics. Cambridge University Press, 1998.

[70] D.J. Griffiths. *Introduction to Quantum Mechanics*. Pearson Prentice Hall, 2005.

[71] S. Gangopadhyay and B.R. Nag. Energy levels in three-dimensional quantum-confinement structures. *Nanotechnology*, 8(1):14–17, 1999.

[72] M.A. Green. Intrinsic concentration, effective densities of states, and effective mass in silicon. *Journal of Applied Physics*, 67(6):2944–2954, 1990.

[73] V A Belyakov, V A Burdov, R Lockwood, and A Meldrum. Silicon nanocrystals: fundamental theory and implications for stimulated emission. *Advances in Optical Technologies*, pages 1–32, 2008.

[74] G. Ledoux, O. Guillois, D. Porterat, C. Reynaud, F. Huisken, B. Kohn, and V. Paillard. Photoluminescence properties of silicon nanocrystals as a function of their size. *Physical Review B*, 62(23):15942–15951, 2000.

[75] H. Hofmeister, F. Huisken, and B. Kohn. Lattice contraction in nanosized silicon particles produced by laser pyrolysis of silane. *The European Physical Journal D-Atomic, Molecular, Optical and Plasma Physics*, 9(1):137–140, 1999.

[76] A.K. Sood, K. Jayaram, and D.V.S. Muthu. Raman and high-pressure photoluminescence studies on porous silicon. *Journal of Applied Physics*, 72(10):4963–4965, 1992.

[77] R. Lockwood, Z. Yang, R. Sammynaiken, J.G.C. Veinot, and A. Meldrum. Light-induced evolution of silicon quantum dot surface chemistry – implications for photoluminescence, sensing, and reactivity. *Chemistry of Materials*, 26(19):5467–5474, 2014.

[78] T.K. Sham, D.T. Jiang, I. Coulthard, J.W. Lorimer, X.H. Feng, K.H. Tan, S.P. Frigo, R.A. Rosenberg, D.C. Houghton, and B. Bryskiewicz. Origin of luminescence from porous silicon deduced by synchrotron-light-induced optical luminescence. *Nature*, 363(6427):331–334, 1993.

[79] F. Zhou and J.D. Head. Role of SiO in the photoluminescence of porous silicon. *The Journal of Physical Chemistry B*, 104(43):9981–9986, 2000.

[80] B. Garrido, M. Lopez, O. Gonzalez, A. Perez-Rodriguez, J.R. Morante, and C. Bonafos. Correlation between structural and optical properties of Si nanocrystals embedded in SiO_2: The mechanism of visible light emission. *Applied Physics Letters*, 77(20):3143–3145, 2000.

[81] Y. Chabal, K. Raghavachari, X. Zhang, and E. Garfunkel. Silanone (Si=O) on Si(100): intermediate for initial silicon oxidation. *Physical Review B*, 66(16):161315, 2002.

[82] M. Lannoo, C. Delerue, and G. Allan. Nonradiative recombination on dangling bonds in silicon crystallites. *Journal of Luminescence*, 57(1-6):243–247, 1993.

[83] D. Goguenheim and M. Lannoo. Theoretical calculation of the electron-capture cross section due to a dangling bond at the Si(111)-SiO_2 interface. *Physical Review B*, 44(4):1724–1733, 1991.

[84] Y. Nishi. Study of silicon-silicon dioxide structure by electron spin resonance i. *Japanese Journal of Applied Physics*, 10(1):52–62, 1971.

[85] H. von Bardeleben, D. Stievenard, A. Grosman, C. Ortega, and J. Siejka. Defects in porous p-type Si: An electron-paramagnetic-resonance study. *Physical Review B*, 47(16):10899–10902, 1993.

[86] V Bratus, S Ishchenko, S Okulov, I Vorona, H von Bardeleben, and M Schoisswohl. EPR and ENDOR study of the P_b center in porous silicon. *Physical Review B*, 50(20):15449–15452, 1994.

[87] M. Schoisswohl, J.L. Cantin, H.J. von Bardeleben, and G. Amato. Electron paramagnetic resonance study of luminescent stain etched porous silicon. *Applied Physics Letters*, 66(26):3660–3662, 1995.

[88] J.L. Cantin, M. Schoisswohl, H.J. von Bardeleben, F. Rochet, and G. Dufour. P_{b1} defect study and chemical characterization of the Si(001)-SiO_2 interface in oxidized porous silicon. *Surface science*, 352:793–796, 1996.

[89] J.L. Cantin, M. Schoisswohl, H.J. von Bardeleben, N. Hadj Zoubir, and M. Vergnat. Observation of (100) surfaces in p-type porous silicon by electron paramagnetic resonance. *Thin Solid Films*, 276:241–243, 1996.

[90] M. Schoisswohl, J.L. Cantin, and M. Chamarro. Defects and visible photoluminescence in porous $Si_{1-x}Ge_x$. *Thin Solid Films*, 276:92–95, 1996.

[91] P.J. Caplan, E.H. Poindexter, B.E. Deal, and R.R. Razouk. ESR centers, interface states, and oxide fixed charge in thermally oxidized silicon wafers. *Journal of Applied Physics*, 50(9):5847–5854, 1979.

[92] E.H. Poindexter, P.J. Caplan, B.E. Deal, and R.R. Razouk. Interface states and electron spin resonance centers in thermally oxidized (111) and (100) silicon wafers. *Journal of Applied Physics*, 52(2):879–884, 1981.

[93] A. Stirling and A. Pasquarello. Modelling of paramagnetic trivalent silicon defect centres in amorphous silica and at Si–SiO_2 interfaces. *Journal of Physics: Condensed Matter*, 17(21):S2099–S2113, 2005.

[94] R.W. Liptak, U. Kortshagen, and S.A. Campbell. Surface chemistry dependence of native oxidation formation on silicon nanocrystals. *Journal of Applied Physics*, 106(6):064313, 2009.

[95] P. Pellegrino. Enhancement of the emission yield of silicon nanocrystals in silica due to surface passivation. *Physica E: Low-dimensional Systems and Nanostructures*, 16:424–428, 2003.

[96] C.A. Grimes, E.C. Dickey, and M.V. Pishko. *Encyclopedia of Sensors*. American Scientific Publishers, 2006.

[97] C.B. Murray, D.J. Norris, and M.G. Bawendi. Synthesis and characterization of nearly monodisperse CdE (E = sulfur, selenium, tellurium) semiconductor nanocrystallites. *Journal of the American Chemical Society*, 115(19):8706–8715, 1993.

[98] D J Norris, M Nirmal, C B Murray, A Sacra, and M G Bawendi. Size dependent optical spectroscopy of ii-vi semiconductor nanocrystallites (quantum dots). *Atoms, Molecules and Clusters*, 26:355–357, 1993.

[99] W.C.W. Chan and S. Nie. Quantum dot bioconjugates for ultrasensitive nonisotopic detection. *Science*, 281(5385):2016–2018, 1998.

[100] U. Resch-Genger, M. Grabolle, S. Cavaliere-Jaricot, R. Nitschke, and T. Nann. Quantum dots versus organic dyes as fluorescent labels. *Nature Methods*, 5(9):763–775, 2008.

[101] P. Alivisatos. The use of nanocrystals in biological detection. *Nature Biotechnology*, 22(1):47–52, 2003.

[102] D.R. Larson. Water-soluble quantum dots for multiphoton fluorescence imaging in vivo. *Science*, 300(5624):1434–1436, 2003.

[103] N.C. Shaner, R.E. Campbell, P.A. Steinbach, B.N.G. Giepmans, A.E. Palmer, and R.Y. Tsien. Improved monomeric red, orange and yellow fluorescent proteins derived from discosoma sp. red fluorescent protein. *Nature Biotechnology*, 22(12):1567–1572, 2004.

[104] X. Michalet. Quantum dots for live cells, in vivo imaging, and diagnostics. *Science*, 307(5709):538–544, 2005.

[105] J. Weng and J. Ren. Luminescent quantum dots: A very attractive and promising tool in biomedicine. *Current Medicinal Chemistry*, 13(8):897–909, 2006.

[106] A.M. Derfus, W.C.W. Chan, and S.N. Bhatia. Probing the cytotoxicity of semiconductor quantum dots. *Nano Letters*, 4(1):11–18, 2004.

[107] L. Ye, K.-T. Yong, L. Liu, I. Roy, R.i Hu, J. Zhu, H. Cai, W.-C. Law, J. Liu, K. Wang, J. Liu, Y. Liu, Y. Hu, X. Zhang, M.T. Swihart, and P.N. Prasad. A pilot study in non-human primates shows no adverse response to intravenous injection of quantum dots. *Nature Nanotechnology*, 7(7):453–458, 2012.

[108] F. Erogbogbo, K.-T. Yong, I. Roy, G. Xu, P.N. Prasad, and M.T. Swihart. Biocompatible luminescent silicon quantum dots for imaging of cancer cells. *ACS Nano*, 2(5):873–878, 2008.

[109] A.R. Zias, C.W. Clapp, D.J. DeMichele, P.R. Emtage, D.K. Hartman, J.W. Savery, and R.C. Thomas. Solid-state potentiometer. *Experimental Mechanics*, 3(9):19A–24A, 1963.

[110] E.J. Anglin, L. Cheng, W.R. Freeman, and M.J. Sailor. Porous silicon in drug delivery devices and materials. *Advanced Drug Deliver Reviews*, 60:1266–1277, 2008.

[111] J.M. Buriak. Organometallic chemistry on silicon and germanium surfaces. *Chemical Reviews*, 102(5):1271–1308, 2002.

[112] J.A. Kelly and J.G.C. Veinot. An investigation into near-UV hydrosilylation of freestanding silicon nanocrystals. *ACS Nano*, 4(8):4645–4656, 2010.

[113] J.A. Kelly, A.M. Shukaliak, M.D. Fleischauer, and J.G.C. Veinot. Size-dependent reactivity in hydrosilylation of silicon nanocrystals. *Journal of the American Chemical Society*, 133(24):9564–9571, 2011.

[114] M. Dasog and J.G.C. Veinot. Size independent blue luminescence in nitrogen passivated silicon nanocrystals. *Physica Status Solidi (A)*, 209(10):1844–1846, 2012.

[115] J.R. Heath. A liquid-solution-phase synthesis of crystalline silicon. *Science*, 258(5085):1131–1133, 1992.

[116] N.A. Dhas, C.P. Raj, and A. Gedanken. Preparation of luminescent silicon nanoparticles: a novel sonochemical approach. *Chemistry of Materials*, 10:3278–3281, 1998.

[117] R.K. Baldwin, J. Zou, K.A. Pettigrew, G.J. Yeagle, R.D. Britt, and S.M. Kauzlarich. The preparation of a phosphorus doped silicon film from phosphorus containing silicon nanoparticles. *Chemical Communications*, pages 658–660, 2006.

[118] R.A. Bley and S.M. Kauzlarich. A low-temperature solution phase route for the synthesis of silicon nanoclusters. *Journal of the American Chemical Society*, 118:12461–12462, 1996.

[119] T.U.M.S Murthy, N. Miyamoto, M. Shimbo, and J. Nishizawa. Gas-phase nucleation during the thermal decomposition of silane in hydrogen. *Journal of Crystal Growth*, 33(1):1–7, 1976.

[120] W.L. Wilson, P.F. Szajowski, and L.E. Brus. Quantum confinement in size-selected, surface-oxidized silicon nanocrystals. *Science*, 262(5137):1242–1244, 1993.

[121] J.D. Holmes, K.J. Ziegler, R.C. Doty, L.E. Pell, K.P. Johnston, and B.A. Korgel. Highly luminescent silicon nanocrystals with discrete optical transitions. *Journal of the American Chemical Society*, 123(16):3743–3748, 2001.

[122] F. Hua, F. Erogbogbo, M.T. Swihart, and E. Ruckenstein. Organically capped silicon nanoparticles with blue photoluminescence prepared by hydrosilylation followed by oxidation. *Langmuir*, 22(9):4363–4370, 2006.

[123] J. Valenta, P. Janda, K. Dohnalová, D. Nižňansky, F. Vácha, and J. Linnros. Colloidal suspensions of silicon nanocrystals: from single nanocrystals to photonic structures. *Optical Materials*, 27(5):1046–1049, 2005.

[124] Z. Zhou, L. Brus, and R. Friesner. Electronic structure and luminescence of 1.1- and 1.4-nm silicon nanocrystals: Oxide shell versus hydrogen passivation. *Nano Letters*, 3(2):163–167, 2003.

[125] R. Lockwood, S. McFarlane, J.R. Rodríguez Núñez, X.Y. Wang, J.G.C. Veinot, and A. Meldrum. Photoactivation of silicon quantum dots. *Journal of Luminescence*, 131(7):1530–1535, 2011.

[126] R. Lockwood, J.G.C. Veinot, and A. Meldrum. Sensing water and alcohol vapors with freestanding silicon quantum dots. *Sensor Letters*, 11(8):1535–1540, 2013.

[127] Z H Zhang, R Lockwood, J G C Veinot, and A Meldrum. Detection of ethanol and water vapor with silicon quantum dots coupled to an optical fiber. *Sensors and Actuators B-Chemical*, 181:523–528, 2013.

[128] S. Cheylan and R.G. Elliman. Hydrogen passivation of Si nanocrystals in silica. *MRS Proceedings*, 650:R3.38.1, 2000.

[129] J. Harper and M.J. Sailor. Photoluminescence quenching and the photochemical oxidation of porous silicon by molecular oxygen. *Langmuir*, 13(17):4652–4658, 1997.

[130] J.H. Song and M.J. Sailor. Quenching of photoluminescence from porous silicon by aromatic molecules. *Journal of the American Chemical Society*, 119(31):7381–7385, 1997.

[131] S. Ye, T. Saito, S. Nihonyanagi, K. Uosaki, P.B. Miranda, D. Kim, and Y.-R. Shen. Stability of the Si-H bond on the hydrogen-terminated Si (111) surface studied by sum frequency generation. *Surface science*, 476(1):121–128, 2001.

[132] S. Godefroo, M. Hayne, M. Jivanescu, A. Stesmans, M. Zacharias, O.I. Lebedev, G. van Tendeloo, and V.V. Moshchalkov. Classification and control of the origin of photoluminescence from Si nanocrystals. *Nature Nanotechnology*, 3(3):174–178, 2008.

[133] J.R. Rodríguez Núñez, J.A. Kelly, E.J. Henderson, and J.G.C. Veinot. Wavelength-controlled etching of silicon nanocrystals. *Chemistry of materials*, 24(2):346–352, 2012.

[134] P.F. Rusch and J.P. Lelieur. Analytical moments of skewed Gaussian distribution functions. *Analytical Chemistry*, 45(8):1541–1543, 1973.

[135] J Linnros, Nenad Lalic, Augustinas Galeckas, and Vytautas Grivickas. Analysis of the stretched exponential photoluminescence decay from nanometer-sized silicon crystals in SiO_2. *Journal of Applied Physics*, 86(11):6128–6134, 1999.

[136] M.N. Berberan-Santos, E.N. Bodunov, and B. Valeur. Mathematical functions for the analysis of luminescence decays with underlying distributions 1. Kohlrausch decay function (stretched exponential). *Chemical Physics*, 315:171–182, 2005.

[137] B.C. Smith. *Fundamentals of Fourier Transform Infrared Spectroscopy, Second Edition*. Taylor & Francis, 2011.

[138] P. Gupta, A.C. Dillon, A.S. Bracker, and S.M. George. FTIR studies of H_2O and D_2O decomposition on porous silicon surfaces. *Surface science*, 245:360–372, 1991.

[139] M. Zacharias, D. Dlmova-Malinovska, and M. Stutzmann. Properties of hydrogenated amorphous silicon suboxide alloys with visible room-temperature photoluminescence. *Philosophical Magazine Part B*, 73(5):799–816, 1996.

[140] R.N. Pereira, D.J. Rowe, R.J. Anthony, and U. Kortshagen. Oxidation of free-standing silicon nanocrystals probed with electron spin resonance of interfacial dangling bonds. *Physical Review B*, 83(15):155327, 2011.

[141] J. Wang, Y. Liu, F. Peng, C. Chen, Y. He, H. Ma, L. Cao, and S. Sun. A general route to efficient functionalization of silicon quantum dots for high-performance fluorescent probes. *Small*, 8(15):2430–2435, 2012.

[142] P.H. Rieger. *Electron Spin Resonance: Analysis and Interpretation.* RSC Publishing, 2007.

[143] C R Helms and E H Poindexter. The silicon-silicon dioxide system: Its microstructure and imperfections. *Reports on Progress in Physics*, 57(8):791, 1994.

[144] C.P. Poole and H.A. Farach. Line shapes in electron spin resonance. *Bulletin of Magnetic Resonance*, pages 162–194, 1979.

[145] A.L. Stancik and E.B. Brauns. A simple asymmetric lineshape for fitting infrared absorption spectra. *Vibrational Spectroscopy*, 47(1):66–69, 2008.

[146] A.M. Stoneham. Linewidths with gaussian and lorentzian broadening. *Journal of Physics D: Applied Physics*, 5(3):670–672, 1972.

[147] G. Van Gorp and A. Stesmans. Dipolar interaction between [111] P_b defects at the (111)Si/SiO_2 interface revealed by electron-spin resonance. *Physical Review B*, 45(8):4344–4371, 1992.

[148] M. Anwar, C.A. Hogarth, and K.A.K. Lott. Electron spin resonance study of thermally evaporated amorphous thin films of MoO_3/SiO. *Physica Status Solidi (A)*, 114(1):225–231, 1989.

[149] P. Hapala, K. Kusova, I. Pelant, and P. Jelínek. Theoretical analysis of electronic band structure of 2-to 3-nm si nanocrystals. *Physical Review B*, 87(19):195420, 2013.

[150] I. Nagai, T. Takahagi, A. Ishitani, H. Kuroda, and M. Yoshikawa. Epitaxial growth of silicon at low temperature by ultrahigh vacuum electron cyclotron resonance plasma chemical vapor deposition. *Journal of Applied Physics*, 64(10):5183–5188, 1988.

[151] G.T. Reed and A.P. Knights. *Silicon Photonics: An Introduction*. Wiley, 2004.

[152] P. Bianucci, J.R. Rodríguez, C.M. Clements, J.G.C. Veinot, and A. Meldrum. Silicon nanocrystal luminescence coupled to whispering gallery modes in optical fibers. *Journal of Applied Physics*, 105(2):023108, 2009.

[153] B.O. Dabbousi, J. Rodriguez-Viejo, F.V Mikulec, J.R. Heine, H. Mattoussi, R. Ober, K.F. Jensen, and M.G. Bawendi. Quantum crystallites and nonlinear optics. *The Journal of Physical Chemistry B*, 101(46):9463–9475, 1997.

[154] D. Jurbergs, E. Rogojina, L. Mangolini, and U. Kortshagen. Silicon nanocrystals with ensemble quantum yields exceeding 60%. *Applied Physics Letters*, 88(23):233116, 2006.

[155] L Pavesi. Silicon-based light sources for silicon integrated circuits. *Advances in Optical Technologies*, pages 1–12, 2008.

[156] W.-Q. Huang, R.-T. Zhang, H.-X. Wang, F. Jin, L. Xu, S.-J. Qin, K.-Y. Wu, S.-R. Liu, and C.-J. Qin. Laser on porous silicon after oxidation by irradiation and annealing. *Optics Communications*, 281(20):5229–5233, 2008.

[157] Z. Kang, Y. Liu, C.H.A. Tsang, D.D.D. Ma, X. Fan, N.-B. Wong, and S.-T. Lee. Water-soluble silicon quantum dots with wavelength-tunable photoluminescence. *Advanced Materials*, 21(6):661–664, 2009.

[158] R. Guerra, E. Degoli, and S. Ossicini. Size, oxidation, and strain in small Si/SiO_2 nanocrystals. *Physical Review B*, 80(15):155332, 2009.

[159] D.E. Harwell, J.C. Croney, W. Qin, J.T. Thornton, J.H. Day, E.K. Hajime, and D.M. Jameson. Effects of surface passivation on silicon nanoparticle photoluminescence. *Chemistry Letters*, 32(12):1194–1195, 2003.

[160] A. Fojtik and A. Henglein. Surface chemistry of luminescent colloidal silicon nanoparticles. *The Journal of Physical Chemistry B*, 110(5):1994–1998, 2006.

[161] S.P. Withrow, C.W. White, A. Meldrum, J.D. Budai, D.M. Hembree, and J.C. Barbour. Effects of hydrogen in the annealing environment on photoluminescence from Si nanoparticles in SiO_2. *Journal of Applied Physics*, 86(1):396, 1999.

[162] O. Guillois. Photoluminescence decay dynamics of noninteracting silicon nanocrystals. *Journal of Applied Physics*, 95(7):3677–3682, 2004.

[163] R. Lockwood, A. Hryciw, and A. Meldrum. Nonresonant carrier tunneling in arrays of silicon nanocrystals. *Applied Physics Letters*, 89(26):263112, 2006.

[164] A. Meldrum, R. Lockwood, V.A. Belyakov, and V.A. Burdov. Computational simulations for ensembles of luminescent silicon nanocrystals: Implications for optical gain and stimulated emission. *Physica E: Low-dimensional Systems and Nanostructures*, 41(6):955–958, 2009.

[165] J. Ji, Y. Chen, R.A. Senter, and J.L. Coffer. Surface modification of erbium-doped silicon nanocrystals. *Chemistry of Materials*, 13(12):4783–4786, 2001.

[166] C.-T. Lee, C.-H. Lin, T.-H. Lee, and T.-C. Tsai. Photoluminescence degradation and passivation mechanisms of Si nanoclusters in silicon oxide matrix. *Japanese Journal of Applied Physics*, 44(6A):4240–4244, 2005.

[167] G.J. Lee, S.H. Song, Y. Lee, H. Cheong, C.S. Yoon, Y.D. Son, and J. Jang. Arbitrary surface structuring of amorphous silicon films based on femtosecond-laser-induced crystallization. *Applied Physics Letters*, 89(15):151907, 2006.

[168] U. Höfer, L. Li, and T. Heinz. Desorption of hydrogen from Si(100)2x1 at low coverages: The influence of π-bonded dimers on the kinetics. *Physical Review B*, 45(16):9485–9488, 1992.

[169] R.Q. Zhang, W.C. Lu, Y.L. Zhao, and S.T. Lee. On the stability of hydride configurations on silicon cluster surfaces: A first-principle theoretical study. *The Journal of Physical Chemistry B*, 108(6):1967–1973, 2004.

[170] R.J. Hamers and Y. Wang. Atomically-resolved studies of the chemistry and bonding at silicon surfaces. *Chemical Reviews*, 96(4):1261–1290, 1996.

[171] X. Zhang, Y.J. Chabal, S.B. Christman, E.E. Chaban, and E. Garfunkel. Oxidation of H-covered flat and vicinal Si(111)-1x1 surfaces. *Journal of Vacuum Science & Technology A: Vacuum, Surfaces, and Films*, 19(4):1725–1729, 2001.

[172] H. Kajiyama, S. Heike, T. Hitosugi, and T. Hashizume. Initial backbond oxidation at an unpaired dangling bond site on a hydrogen-terminated Si(100)2x1 surface. *Japanese Journal of Applied Physics*, 37(Part 2, No. 11B):L1350–L1353, 1998.

[173] M.A. Zaïbi, C.A. Sébenne, and J.P. Lacharme. Effect of temperature on NH_3 reactivity with Si(100)2x1. *Surface Review and Letters*, 08(06):621–626, 2001.

[174] R. Eyre, J. Goss, and P. Briddon. Density functional study of oxygen migration processes for silicon quantum dots. *Physical Review B*, 76(24):245325, 2007.

[175] D.L. Staebler and C.R. Wronski. Reversible conductivity changes in discharge-produced amorphous Si. *Applied Physics Letters*, 31(4):292–294, 1977.

[176] H. Bahruji and P.R. Bowker, M.and Davies. Photoactivated reaction of water with silicon nanoparticles. *International Journal of Hydrogen Energy*, 34(20):8504–8510, 2009.

[177] M. Sauer. Reversible molecular photoswitches: A key technology for nanoscience and fluorescence imaging. *Proceedings of the National Academy of Sciences of the United States of America*, 102(27):9433–9434, 2005.

[178] J.W.M. Chon, P. Zijlstra, M. Gu, J. van Embden, and P. Mulvaney. Two-photon-induced photoenhancement of densely packed CdSe/ZnSe/ZnS nanocrystal solids and its application to multilayer optical data storage. *Applied Physics Letters*, 85(23):5514–5516, 2004.

[179] G.G. Yordanov, G.D. Gicheva, and Ceco D. Dushkin. Optical memory based on photo-activated fluorescence of core/shell CdSe/CdS quantum dots embedded in poly (butylmethacrylate). *Materials chemistry and physics*, 113(2):507–510, 2009.

[180] J. Dian, T. Holec, I. Jelinek, J. Jindřich, J. Valenta, and I. Pelant. Time evolution of photoluminescence response from porous silicon in hydrocarbon gas sensing. *Physica Status Solidi (A)*, 182(1):485–488, 2000.

[181] P.A. Snow, E.K. Squire, P. Russell, and L. T Canham. Vapor sensing using the optical properties of porous silicon bragg mirrors. *Journal of Applied Physics*, 86(4):1781–1784, 1999.

[182] B.H. King, A. Gramada, J.R. Link, and M.J. Sailor. Internally referenced ammonia sensor based on an electrochemically prepared porous SiO_2 photonic crystal. *Advanced Materials*, 19(22):4044–4048, 2007.

[183] S. Content, W.C. Trogler, and M.J. Sailor. Detection of nitrobenzene, DNT, and TNT vapors by quenching of porous silicon photoluminescence. *Chemistry-A European Journal*, 6(12):2205–2213, 2000.

[184] V.S. Lin. A porous silicon-based optical interferometric biosensor. *Science*, 278(5339):840–843, 1997.

[185] S. Chan, P.M. Fauchet, Y. Li, L.J. Rothberg, and B.L. Miller. Porous silicon microcavities for biosensing applications. *Physica Status Solidi (A)*, 182(1):541–546, 2000.

[186] S. Zangooie, R. Jansson, and H. Arwin. Ellipsometric characterization of anisotropic porous silicon Fabry-Pérot filters and investigation of temperature effects on capillary condensation efficiency. *Journal of Applied Physics*, 86(2):850–858, 1999.

[187] O. Bisi and S. Ossicini. Porous silicon: a quantum sponge structure for silicon based optoelectronics. *Surface Science Reports*, 38:1–126, 2000.

[188] V. Baranauskas, D.C. Chang, B.B. Li, A.C. Peterlevitz, V.J. Trava-Airoldi, E.J. Corat, R.K. Singh, and D.-G. Lee. Diamond coating of porous silicon. *Journal of Porous Materials*, 7:401–405, 2000.

[189] P. Mulvaney, L.M. Liz-Marzán, M. Giersig, and T. Ung. Silica encapsulation of quantum dots and metal clusters. *Journal of Materials Chemistry*, 10(6):1259–1270, 2000.

[190] F Lukes. Oxidation of Si and GaAs in air at room temperature. *Surface Science*, 30:91–100, 1972.

[191] W. Menz, J. Mohr, and O. Paul. *Microsystem Technology*. Wiley, 2008.

[192] T. Holec, T. Chvojka, I. Jelínek, J. Jindřich, I. Němec, I. Pelant, J. Valenta, and J. Dian. Determination of sensoric parameters of porous silicon in sensing of organic vapors. *Materials Science and Engineering: C*, 19(1):251–254, 2002.

[193] J.M. Lauerhaas and M.J. Sailor. Chemical modification of the photoluminescence quenching of porous silicon. *Science*, 261(5128):1567–1568, 1993.

[194] D.B. Mawhinney, J.A. Glass, and J.T. Yates. FTIR study of the oxidation of porous silicon. *The Journal of Physical Chemistry B*, 101(7):1202–1206, 1997.

[195] T. Maruyama and S. Ohtani. Photoluminescence of porous silicon exposed to ambient air. *Applied Physics Letters*, 65(11):1346–1348, 1994.

[196] G. Ledoux, J. Gong, and F. Huisken. Effect of passivation and aging on the photoluminescence of silicon nanocrystals. *Applied Physics Letters*, 79(24):4028–4030, 2001.

[197] M. Baran, L. Khomenkova, N. Korsunska, T. Stara, M. Sheinkman, Y. Goldstein, J. Jedrzejewski, and E. Savir. Investigation of aging process of Si-SiO_x structures with silicon quantum dots. *Journal of Applied Physics*, 98(11):113515, 2005.

[198] V. Švrček, T. Sasaki, R. Katoh, Y. Shimizu, and N. Koshizaki. Aging effect on blue luminescent silicon nanocrystals prepared by pulsed laser ablation of silicon wafer in de-ionized water. *Applied Physics B*, 94(1):133–139, 2009.

[199] C.M. Hessel, D. Reid, M.G. Panthani, M.R. Rasch, B.W. Goodfellow, J. Wei, H. Fujii, V. Akhavan, and B.A. Korgel. Synthesis of ligand-stabilized silicon nanocrystals with size-dependent photoluminescence spanning visible to near-infrared wavelengths. *Chemistry of materials*, 24(2):393–401, 2012.

[200] S.T. Lakshmikumar and P.K. Singh. Stabilization of porous silicon surface by low temperature photoassisted reaction with acetylene. *Current Applied Physics*, 3:185–189, 2003.

[201] A. Stegner, R. Pereira, R. Lechner, K. Klein, H. Wiggers, M. Stutzmann, and M. Brandt. Doping efficiency in freestanding silicon nanocrystals from the gas phase: Phosphorus incorporation and defect-induced compensation. *Physical Review B*, 80(16):165326, 2009.

[202] M Lopez, B Garrido, P Pellegrino, J R Morante, C Bonafos, M Carrada, and A Claverie. Elucidation of the surface passivation role on the photoluminescence emission yield of silicon nanocrystals embedded in SiO_2. *Applied Physics Letters*, 80(9):1637–1639, 2002.

[203] R. Espiau de Lamaëstre and H. Bernas. Significance of lognormal nanocrystal size distributions. *Physical Review B*, 73(12):125317, 2006.

[204] G. Lucovsky, R. Nemanich, and J. Knights. Structural interpretation of the vibrational spectra of a-Si:H alloys. *Physical Review B*, 19(4):2064–2073, 1979.

[205] P. Gupta, V.L. Colvin, and S.M. George. Hydrogen desorption kinetics from monohydride and dihydride species on silicon surfaces. *Physical Review B*, 37(14):8234–8244, 1988.

[206] D. Tsu, G. Lucovsky, and B. Davidson. Effects of the nearest neighbors and the alloy matrix on SiH stretching vibrations in the amorphous SiO_r:H ($0<r<2$) alloy system. *Physical Review B*, 40(3):1795–1805, 1989.

[207] K.H. Li, C. Tsai, J.C. Campbell, M. Kovar, and J.M. White. The effect of surface species on the photoluminescence of porous silicon. *Journal of Electronic Materials*, 23(4):409–412, 1994.

[208] X.J. Li, S.J. Chen, and C.Y. Feng. Characterization of silicon nanoporous pillar array as room-temperature capacitive ethanol gas sensor. *Sensors and Actuators B-Chemical*, 123(1):461–465, 2007.

[209] M.P. Stewart and J.M. Buriak. Photopatterned hydrosilylation on porous silicon. *Angewandte Chemie International Edition*, 37(23):3257–3260, 1998.

[210] R. Boukherroub, S. Morin, D.D.M. Wayner, and D.J. Lockwood. Thermal route for chemical modification and photoluminescence stabilization of porous silicon. *Physica Status Solidi (A)*, 182(1):117–121, 2000.

[211] M. McGonigal, V.M. Bermudez, and J.E. Butler. Infrared reflection absorption spectroscopy study of the chemisorption of small molecules (H_2, O_2 and H_2O) on silicon. *Journal of Electron Spectroscopy and Related Phenomena*, 54/55:1033–1044, 1990.

[212] M.A.L. Vargas, G. Busca, T. Montanari, M.C.H Delgado, and L.J. Alemany. Preparation and characterization of silicon hydride oxide: a fully hydrophobic solid. *Journal of Materials Chemistry*, 15(8):910–915, 2005.

[213] Tatsuo Shimizu and Minoru Kumeda. Rate equations for the creation of various metastable dangling bonds in a-Si:H mediated by floating bonds. *Japanese Journal of Applied Physics*, 38(Part 2, No. 8B):L911–L913, 1999.

[214] A. Gupta and H. Wiggers. Freestanding silicon quantum dots: origin of red and blue luminescence. *Nanotechnology*, 22(5):055707, 2010.

[215] M. Glover and A. Meldrum. Effect of "buffer layers" on the optical properties of silicon nanocrystal superlattices. *Optical Materials*, 27(5):977–982, 2005.

[216] R. Oren and S.K. Ghandhi. Ultraviolet-enhanced oxidation of silicon. *Journal of Applied Physics*, 42(2):752–756, 1971.

[217] A. Kazor and I.W. Boyd. Growth and modeling of cw-UV induced oxidation of silicon. *Journal of Applied Physics*, 75(1):227–231, 1994.

[218] R. Walsh. Bond dissociation energy values in silicon-containing compounds and some of their implications. *Accounts of chemical research*, 14(8):246–252, 1981.

[219] M. Fujii, S. Minobe, M. Usui, E. Hayashi, S.and Gross, J. Diener, and D. Kovalev. Generation of singlet oxygen at room temperature mediated by energy transfer from photoexcited porous Si. *Physical Review B*, 70(8):085311, 2004.

[220] M.A. Osborne and S.F. Lee. Quantum dot photoluminescence activation and decay: Dark, bright, and reversible populations in ZnS-capped CdSe nanocrystals. *ACS Nano*, 5(10):8295–8304, 2011.

[221] Z. Yang, M. Dasog, A.R. Dobbie, R. Lockwood, Y. Zhi, A. Meldrum, and J.G.C. Veinot. Hybrid materials: Highly luminescent covalently linked silicon nanocrystal/polystyrene hybrid functional materials: Synthesis, properties, and processability. *Advanced Functional Materials*, 24(10):1344–1344, 2014.

[222] G. Gagliardi, M. Salza, S. Avino, P. Ferraro, and P. De Natale. Probing the ultimate limit of fiber-optic strain sensing. *Science*, 330:1081–1084, 2010.

[223] M. McSherry, C. Fitzpatrick, and E. Lewis. Review of luminescent based fibre optic temperature sensors. *Sensor Review*, 25(1):56–62, 2005.

[224] V.I. Ruiz-Pérez and M.A. Basurto-Pensado. Fiber optic pressure sensor using multimode interference. *Journal of Physics: Conference Series*, 274:1–7, 2011.

[225] Y.-G. Lee. Transmissive grating-reflective mirror-based fiber optic accelerometer for stable signal acquisition in industrial applications. *Optical Engineering*, 51(5):054402, 2012.

[226] B. Schmauß, M. März, and J. Ernst. A fiber-optic sensor for microwave field measurements. *Review of Scientific Instruments*, 66(8):4031–4033, 1995.

[227] B.R. Soller, S.O. Heard, N.A. Cingo, C. Hsi, J. Favreau, T. Khan, R.R. Ross, and J.C. Puyana. Application of fiberoptic sensors for the study of hepatic dysoxia in swine hemorrhagic shock. *Critical Care Medicine*, 29(7):1438–1444, 2001.

[228] B. Lee. Review of the present status of optical fiber sensors. *Optical Fiber Technology*, 9(2):57–79, 2003.

[229] F. Baldini, A. Giannetti, A. Mencaglia, and C. Trono. Fiber optic sensors for biomedical applications. *Current Analytical Chemistry*, 4(4):378–390, 2008.

[230] C. Elosua, I. Matias, C. Bariain, and F. Arregui. Volatile organic compound optical fiber sensors: A review. *Sensors*, 6(11):1440–1465, 2006.

[231] M. El-Sherif, L. Bansal, and J. Yuan. Fiber optic sensors for detection of toxic and biological threats. *Sensors*, 7:3100–3118, 2007.

[232] Y.Z. Liao, V. Strong, Y. Wang, X.-G. Li, X. Wang, and R.B. Kaner. Oligotriphenylene nanofiber sensors for detection of nitro-based explosives. *Advanced Functional Materials*, 22(4):726–735, 2011.

[233] H. Steiner, M. Jakusch, M. Kraft, M. Karlowatz, T. Baumann, R. Niessner, W. Konz, A. Brandenburg, K. Michel, C. Boussard-Plédel, B. Bureau, J. Lucas, Y. Reichlin, A. Katzir, N. Fleischmann, K. Staubmann, R. Allabashi, J.M. Bayona, and B. Mizaikoff. *In Situ* sensing of volatile organic compounds in groundwater: First field tests of a mid-infrared fiber-optic sensing system. *Applied Spectroscopy*, 57(6):607–613, 2003.

[234] M. Morisawa and S. Muto. Plastic optical fiber sensing of alcohol concentration in liquors. *Journal of Sensors*, pages 1–5, 2012.

[235] G.R.C. Possetti, M. Muller, and J.L. Fabris. Refractometric optical fiber sensor for measurement of ethanol concentration in ethanol-gasoline blend. *SBMO/IEEE MTT-S International Microwave & Optoelectronics Conference*, pages 616–620, 2009.

[236] N.A. Yebo, P. Lommens, Z. Hens, and R. Baets. An integrated optic ethanol vapor sensor based on a silicon-on-insulator microring resonator coated with a porous ZnO film. *Opt. Express*, 18(11):11859–11866, 2010.

[237] F. Pang, X. Han, F. Chu, J. Geng, H. Cai, R. Qu, and Z. Fang. Sensitivity to alcohols of a planar waveguide ring resonator fabricated by a sol-gel method. *Sensors and Actuators B-Chemical*, 120(2):610–614, 2007.

[238] M. Konstantaki, A. Klini, D. Anglos, and S. Pissadakis. An ethanol vapor detection probe based on a ZnO nanorod coated optical fiber long period grating. *Optics Express*, 20(8):8472–8484, 2012.

[239] B. Renganathan, D. Sastikumar, and G. Gobi. Nanocrystalline ZnO coated fiber optic sensor for ammonia gas detection. *Optics & Laser Technology*, 43(1398-1404), 2011.

[240] W. Ma, H. Yang, W. Wang, P. Gao, and J. Yao. Ethanol vapor sensing properties of triangular silver nanostructures based on localized surface plasmon resonance. *Sensors*, 11(9):8643–8653, 2011.

[241] G.G. Salgado, T.D. Becerril, H.J. Santiesteban, and E.R. Andrés. Porous silicon organic vapor sensor. *Optical Materials*, 29(1):51–55, 2006.

[242] B.H. King, A.M. Ruminski, J.L. Snyder, and M.J. Sailor. Optical-fiber-mounted porous silicon photonic crystals for sensing organic vapor breakthrough in activated carbon. *Advanced Materials*, 19(24):4530–4534, 2007.

[243] F. Pourfayaz, A. Khodadadi, Y. Mortazavi, and S.S. Mohajerzadeh. CeO_2 doped SnO_2 sensor selective to ethanol in presence of CO, LPG and CH_4. *Sensors and Actuators B-Chemical*, 108:172–176, 2005.

[244] Y.D. Jeong, Y.H. Won, and S.O. Choi. Tunable single-mode Fabry-Perot laser diode using a built-in external cavity and its modulation characteristics. *Optics Letters*, 31(17):2586–2588, 2006.

Appendix A

Detection of ethanol and water vapor with silicon quantum dots coupled to an optical fiber

---

Abstract

The end facet of a standard multimode optical fiber was coated with fluorescent silicon quantum dots (Si-QDs) and used as a probe to detect water and alcohol vapors as a feasibility study for sensing applications. In this work, the response of the sensor to different analytes was observed, and the repeatability of the sensor response was investigated. When exposed to different vapors, the luminescence intensity of the Si-QDs varied over timescales of a few seconds to hours. By coupling the QDs to an optical fiber splitter, fiber-based measurements were demonstrated for ethanol and water vapor. At this stage, the Si-quantum-dot-based fiber sensing shows a fast response time and reasonable detection limits, but true quantification remains difficult owing in part to sample-to-sample variations.

A.1 Introduction

Optical fiber sensors present a vast array of practical remote sensing devices. They can be used to sense changes in strain [222], temperature [223], pressure [224], vibration and acceleration [225], and local electromagnetic fields [226]. They can perform refractometry [152] and measure solution properties such as pH and pO_2 [227], and they are finding a wide range of uses in biomedical analysis [228, 229]. Efforts have been made toward the development of a fiber optic sensor for volatile organics [230], for the remote analysis of toxic or explosive gases [231, 232] or for the detection of organic contaminants in groundwater [233]. Fiber sensors for measuring the ethanol concentration in alcoholic beverages [234] and in gasoline [235] have been reported. Optical sensors for ethanol vapors based on absorption of ethanol on ZnO particles attached to microring resonators [236, 237], nanorods [238], or thinned optical fibers [239] have also been reported. Surface plasmon resonances of silver particles coupled to an optical fiber have also been used for ethanol sensing [240].

Silicon-based detectors can be advantageous because of their benign chemistry, relative ease of handling, and low toxicity in biological environments [110]. Porous silicon (PSi) has been much studied for vapor sensing applications [27, 180, 241] due to its large surface area and wide range of transduction mechanisms, but the material is fragile and difficult to interface with an optical fiber. In one case, a planar PSi microcavity structure was adhered to one end of a bifurcated fiber [242]. When exposed to either humidity or one of three different volatile hydrocarbons, the cavity resonance shifted to longer wavelengths as measured by light injected through one arm of the fiber, reflected from the cavity, and analyzed by a spectrometer.

We previously showed that when freestanding (*i.e.*, not embedded in a matrix) Si-QDs are exposed to blue or UV light in room air, the luminescence intensity can increase by a factor of at least 10 [125]. This process is called "photoactivation". Fourier-transform infrared spectroscopy (FTIR) was used to show that photoactivation occurs in a two-step process. The first step involved the breaking of Si–H surface terminations, leaving behind a non-radiative trap (possibly the neutral P_b center). During this rapid initial stage, the fluorescence intensity decreases and the fluorescence lifetimes shorten. The second step involves the oxidation and hydration

of the dangling bonds, which leads to a prolonged gradual increase in the emission intensity over a period of hours in room air [125]. During this stage, signals from hydride and oxide surface bonds were observed to grow stronger with activation time.

In most synthesis methods the Si-QDs are encapsulated in a solid matrix. While advantageous for certain applications, solid encapsulation isolates the QDs from the environment and physically blocks their response to the surrounding atmosphere. The objective of the present work was, therefore, to integrate freestanding (unencapsulated) Si-QDs into a fluorescence sensor structure. We use a basic fiber-coupled design to detect water and ethanol vapors, using the quantum-dot photoactivation property as the transduction mechanism.

A.2 Materials and Methods

The Si-QDs were prepared in bulk by dissolution from a silica-like matrix [30]. Briefly, the procedure involved annealing gram quantities of hydrogen silsesquioxane ($H_{12}Si_8O_{12}$) for one hour at 1100 °C under an atmosphere consisting of 95% Ar + 5% H_2. This produced a tan-colored powder of consisting of Si-QDs embedded in a silica matrix. The powder was then mechanically pulverized and the Si-QDs were subsequently freed from the silica matrix by etching for 15 min in a solution of 7.5 mL HF (49%, v/v aqueous) + 0.2 mL HCl (37%, v/v aqueous). This was followed by an additional 5-min etch with 5.0 mL of ethanol (95%, v/v aqueous) added to the HF + HCl solution. The suspended QDs were then extracted into toluene. The toluene was evaporated until a relatively high concentration of particles in solution was obtained.

The sensor structure was designed using a 2 × 2 optical fiber coupler (Fig. A.1a) with 50% coupling at 800 nm, near the peak fluorescence wavelength of the Si-QDs. Light from a blue diode laser was coupled into one arm of the fiber coupler. A layer of Si-QDs was deposited on the opposite end of the same arm of the fiber coupler, by dipping one end of the cleaved fiber into the QD solution and allowing it to dry in ambient conditions. The QD-coated end of the fiber coupler was inserted into an environmentally sealed chamber with a volume of ∼30 mL. Fluorescence from the Si-QDs was collected by the same arm of the fiber and evanescently transferred

to the third arm of the coupler. This was attached to an Ocean Optics USB2000 spectrometer. The fourth arm of the coupler was used to monitor the power and stability of the pump laser. The coupling efficiency ratio was found to be about 2:1 at the 445 nm laser wavelength, so the QDs were always placed on the higher-pump-power arm (∼80 μW emitted from the fiber tip).

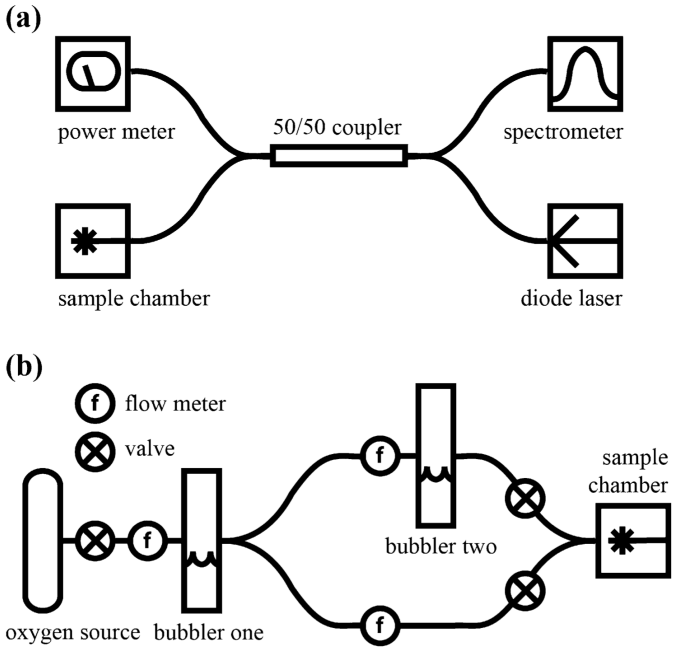

Figure A.1. (a) Diagram of the sensor structure and (b) diagram of the layout for the vapor sensing experiments.

To characterize the response of the sensor to different analytes, the sample chamber was partly filled with liquid, in order to obtain a saturated vapor pressure. The analytes tested were water, a 50% (v/v) mixture of ethanol and water, and 100% anhydrous ethanol, all with room air in the chamber. Calibration tests were also done using only air or 99.998% O_2 gas in the chamber, without an analyte liquid. A blank run was also performed in each set of experiments, without the Si-QDs on the fiber tip.

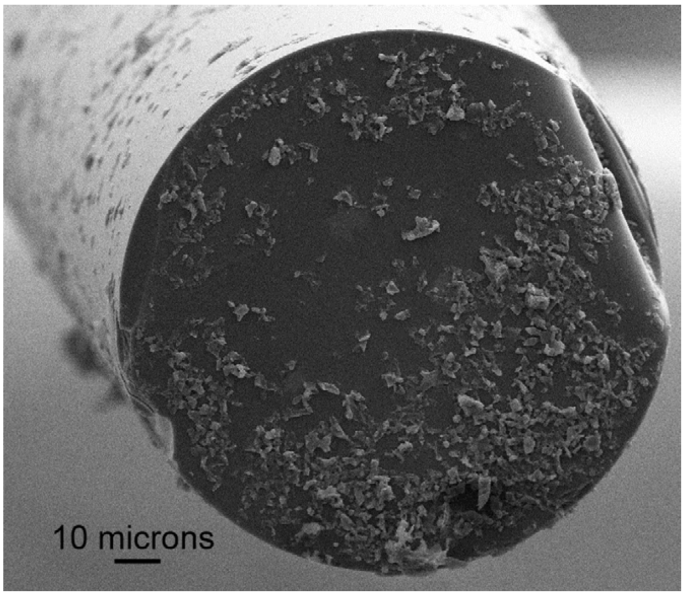

Figure A.2. Topographic SEM image showing the sensor end of a fiber. The Si-QDs appear as small clumps on the cleaved end of the fiber, and along the length of the fiber that was dipped into the solution.

In order to measure the repeatability of the sensor response, a similar gas chamber was used. A gas manifold linked two gas lines to the same input line on the chamber (Fig. A.1b). One line flows through bubbler 2, which contained water, ethanol or a mixture of the two liquids. The carrier gas was 99.998% dry O_2. The other line delivered only O_2 to the chamber. In order to measure the response to water and ethanol vapor, a set of valves diverts the flow from the dry line to the bubbler line. Thus, switching from the dry O_2 line to the bubbler-2 line could be repeated as often as desired. A second bubbler (bubbler 1) could be inserted before the gas manifold, for cases (as described below) in which both vapors of water and ethanol were needed in the same run.

A.3 Results

The Si-QDs formed micron-scale "clumps" on the end facet of the sensor arm of the fiber coupler (Fig. A.2). The luminescence from the QDs was readily detectable (Fig. A.3), initially peaking at a wavelength near 750 nm. With the chamber sealed with dry O_2 the fluorescence intensity decreased relatively quickly over the first 30 min, followed by a more gradual continuous decrease. In room air (*i.e.*, no liquid

in the chamber, 40% relative humidity), the integrated photoluminescence intensity decreased initially, followed by a slow continuous increase over 60 min, consistent with previous results for QDs deposited on a wafer [125].

The sensorgrams in Fig. A.4 highlight the different responses to different analytes in the chamber. The integrated intensity of first spectrum was subtracted from all the integrated intensity measurements. This effectively "subtracted out" underlying contributions from the fiber (which showed background luminescence) and the variations in QD concentration on the fiber tips. With water in the chamber, the PL intensity increased strongly over the first 10 min before approaching saturation. With ethanol in the chamber, the curve was somewhat different: in this case it showed a sigmoidal shape, increasing slowly at first but then increasing more quickly. The water–ethanol mixture showed a behavior intermediate between those for the two pure liquids. With dry O_2 in the chamber, there was a gradual decrease in the integrated intensity over time. For all the curves in Fig. A.4, there was no gas flow through the chamber: the chamber was simply sealed with the various samples inside.

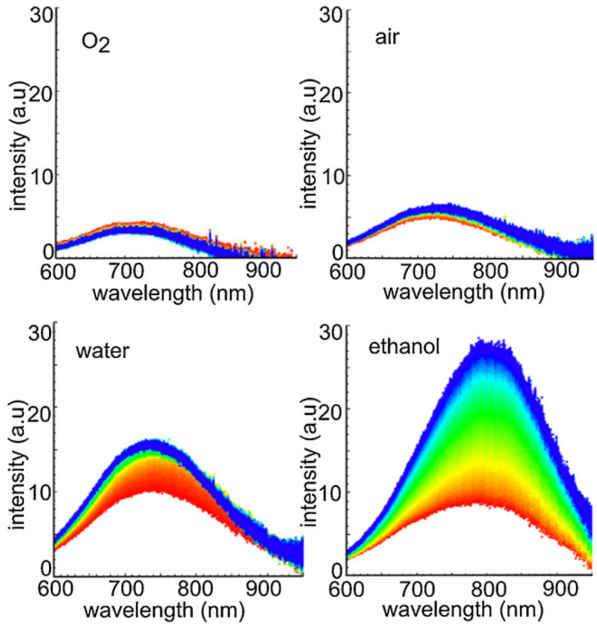

Figure A.3. Fluorescence spectra from the Si-QDs on the end of a fiber coupler, in various static atmospheres. The collection interval was 30 s. The colors red to blue represent successive spectra taken over a period of 1 h.

Having established the baseline sensor response, the repeatability was measured next. From the basic activation curves in Fig. A.4, alternating between either water or ethanol (showing a fluorescence intensity increase) and dry O_2 (showing a decrease) could permit the sensor response to be cycled. Thus, for these experiments, O_2 gas was flowed into the sample chamber at a rate of 0.13 L/min. The O_2 gas flow was diverted through the bubbler for periods of 15 s every 10 min. In order to compare the sensor response, experiments were conducted with water, ethanol, or a 50% by volume mixture in the bubbler.

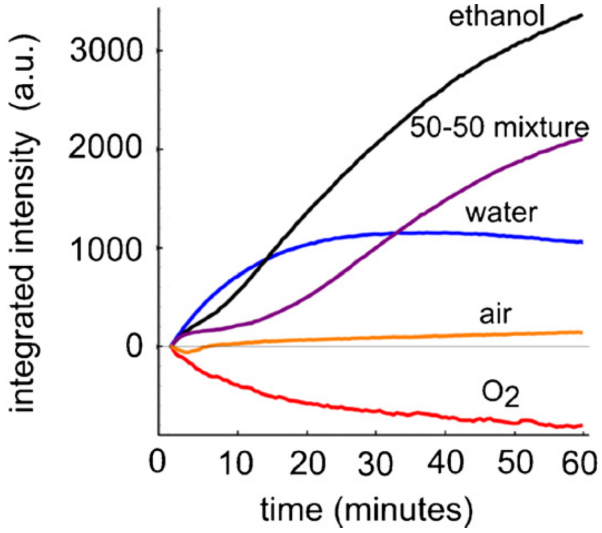

Figure A.4. Integrated fluorescence intensity as a function time for the Si-QD fiber sensor in O_2, room air, and air saturated with water, ethanol, or a 50% mixture of both. All data collected at room temperature. In order to facilitate comparisons between different samples, the first data point of each series was assumed to have a zero arbitrary intensity value. Thus, for an O_2 ambient, we see that the intensity decreased after the first measurement.

The sensor response was found to be repeatable (Fig. A.5). After a 15-s-long injection of the saturated vapor the fluorescence intensity increased sharply, reaching a maximum value approximately 16s after the bubbler valve was opened. This is approximately equal to the calculated delay based on the measured flow rate and the bubbler-to-chamber tubing volume, implying that the sensor response is fast. The luminescence then decayed over a period of about 2 min, reaching a level close to the original value. In various experiments, the sensor was tested up to 30 consecutive times; the response was found to be repeatable, although with a slight background

variation in the luminescence intensity. Furthermore, the response was different for each vapor; it was largest for water vapor, smallest for ethanol, and intermediate for mixtures of the two. This behavior is consistent with the "static" results in Fig. A.3, which showed the fastest initial increase for water.

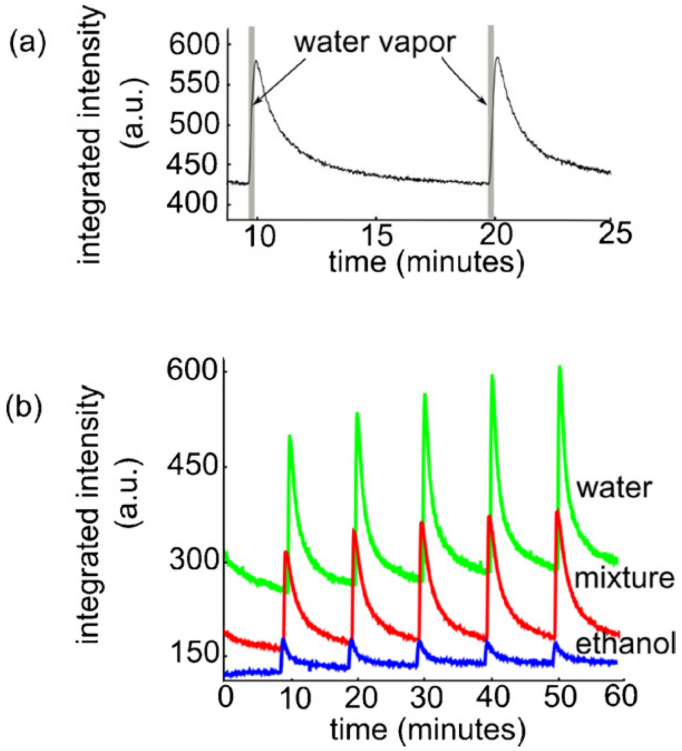

Figure A.5. Sensor response (integrated intensity) to repeated 15-s exposures to saturated water vapor, ethanol vapor, or a 50% mixture of both, using O_2 as the carrier gas. Data offset for clarity. The inset shows the timing of the 15-s vapor-injection intervals superimposed on the sensor response.

We next performed consecutive water and ethanol sensor response measurements on the same sample. One sample was first exposed to five cycles with water in the bubbler. The bubbler was then emptied, rinsed, re-filled with ethanol, and five further cycles were conducted with ethanol vapor. The same experiment was then repeated in reverse order for a second sample (ethanol first, then water). The results showed reasonable consistency; the response was always greatest for water (Fig. A.6). The responses did not completely mirror each other, however. When water vapor was injected first, the sensor response to ethanol was slightly larger than it was otherwise.

The sensor response to water and ethanol (and the mixture) might be difficult to distinguish, without an initial calibration to determine the magnitude of the response to each vapor (as in Fig. A.5). Two additional experiments were therefore conducted in order to determine whether the sensor could be specific to one vapor. First, a fresh sensor was made and continuously exposed to water vapor from a bubbler on the main line, while pumped with the laser. The sample was exposed for 50min, which was sufficiently long for the sensor response to become saturated, with little further evolution of the fluorescence spectrum. At this point, the sensor is no longer responsive to water vapor. The water–vapor-saturated carrier gas was then diverted through a second bubbler containing ethanol. While the changes are smaller in this case, the effect of the ethanol could be clearly observed by a small rise in the integrated emission intensity every time the second bubbler was added to the gas flow (Fig. A.7). In the reverse case, the sensor response was first saturated with ethanol vapor and then water was introduced in the second bubbler, for 15-s intervals. Again, a small response was clearly observed. Thus, if the magnitude of the response cannot unequivocally determine between different vapors (*i.e.*, no pre-calibration), then a pretreatment with one vapor might make the sensor responsive to the other one.

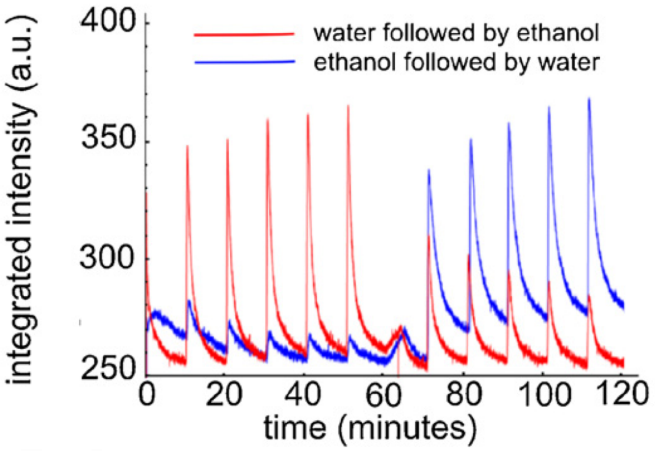

Figure A.6. Sensor response to repeated exposures to water vapor and ethanol. The blue curve shows the response to five 15-s ethanol vapor injections, followed by 5 injections of water vapor. The red line is similar, except in the reverse order.

A.4 Discussion

While the detailed mechanism for the sensor response will remain open to question, several lines of evidence are consistent with a set of possible surface modifications that can occur on the surface of the QDs. First, the response to ethanol vapor is different from that to water vapor (in terms of the photoactivation rate and saturation behavior). Second, when exposed to dry O_2, the photoactivation process is at least partly reversible. Third, the response can saturate and then bleach. Fourth, a weak photoactivation can be induced when the luminescence response was first saturated in one vapor, and the QDs were then exposed to a different vapor. Fifth, the effect of the carrier gas was investigated by repeating several measurements using N_2 or Ar as the carrier gas, in place of O_2. For these atmospheres, little to no detectable photoactivation was found. Thus, O_2 in the carrier is necessary for the photoactivation process to occur at a useful rate.

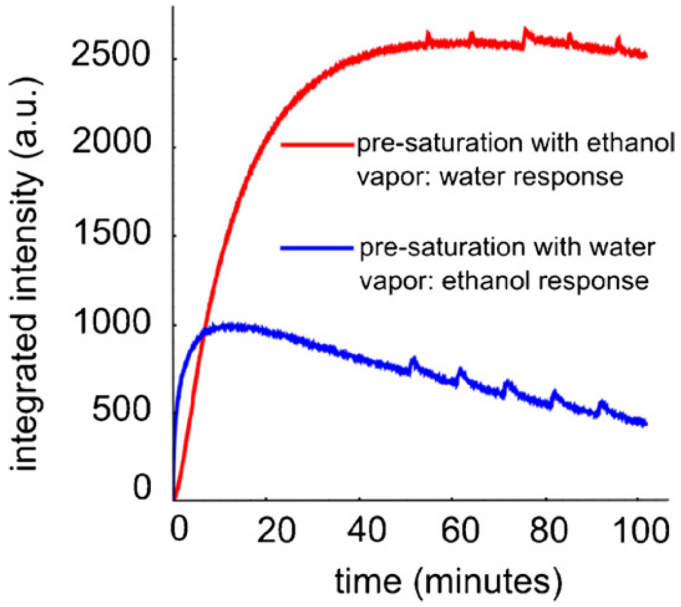

Figure A.7. The blue line shows the sensor response when the fiber was initially exposed to water vapor for 50 min. The ethanol–vapor injections are clearly observed. The red line shows the sensor response to water vapor, after being pre-saturated with ethanol. The carrier gas was O_2.

The processes (photoactivation or "de-activation") do not occur without blue-light irradiation. Allowing the sensor end of the fiber coupler to "sit" in any of

the investigated vapors resulted in no effect – in other words, one can partially photoactivate the QDs, turn the pump laser off while the sensor remains exposed to the analyte for 30-60 min, and when the laser is turned back on there are few changes in the fluorescence spectrum or intensity. This is illustrated in Fig. A.8, in which the "active" end of the sensor was allowed to remain in a water–vapor saturated atmosphere, and the laser was turned on periodically. The overall evolution of the luminescence intensity looks mainly similar to that in Fig. A.4, only interrupted by the periodic laser-off intervals.

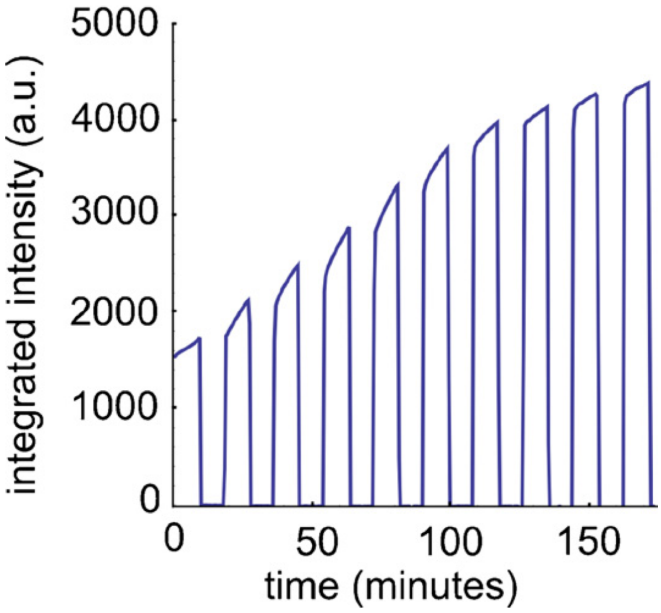

Figure A.8. Photoactivation response (integrated intensity) when the pump laser was cycled numerous times, while the sensing end of the fiber was continuously maintained in a water-saturated atmosphere. Unlike Fig. A.4, the intensity of the first measurement was not subtracted in this case.

While these present experiments cannot unambiguously determine the potentially numerous surface effects responsible for the sensor response, the fact that the response appears different for the two vapors investigated is encouraging from the point of view of making a sensor that could be specific to the desired analytes. Thus, we compare now the sensor response reported here with a selected number of alternative fiber sensors for ethanol vapor. The main points for a brief qualitative comparison are the detection limits, repeatability, response time, and cost.

In one particularly elegant example, a ring resonator was constructed for ethanol detection using evanescent coupling from a tunable laser source to measure the cavity resonances [237]. Ethanol was absorbed into the sol-gel layer of the resonator, causing the mode to shift. Detection of 31 ppm ethanol was clearly demonstrated, and sub-ppm levels could probably be probed with a sufficiently high-resolution scanning laser system. However, the maximum detection limit was close to 200 ppm, limited by the free spectral range of the resonator. In another example, ZnO nanoparticles absorbed ethanol in the vicinity of a silicon ring resonator [236], with a lower detection limit of 100 ppm.

In order to investigate the detection limit (DL), we made a solution of 5 vol.% ethanol dissolved in tetrahydrofuran (THF). Dry THF was found to produce no observable photoactivation, and is a solute for ethanol. The saturated ethanol concentration in the vapor is 7.3 mol.% for this mixture. This was further diluted by mixing with the oxygen carrier gas in the bubbler and combining it with a dry O_2 flow. In Fig. A.9, we observe the sensor response for five 15-s exposures to vapors ranging in concentration from 0.23 to 0.094 mol.% ethanol. The sensor response was observed and was repeatable. Assuming a 3 dB signal-to-noise detection limit, from Fig. A.9 we can estimate conservatively that the DL is $\sim$380 ppm for 15-s exposure times. For longer exposures, the detection limit should decrease accordingly. In Fig. A.4, we see that the 1-h response is orders of magnitude larger than it is after 15 s. This suggests that, given sufficient time, the detection limit could be reasonably low. Alternatively, the photoactivation rate can be increased by using a higher laser power. In recent work, we have found that a power as high as a few mW can be obtained in the sensor arm by using better coupling setups, although the effect of such high pump power was not investigated here.

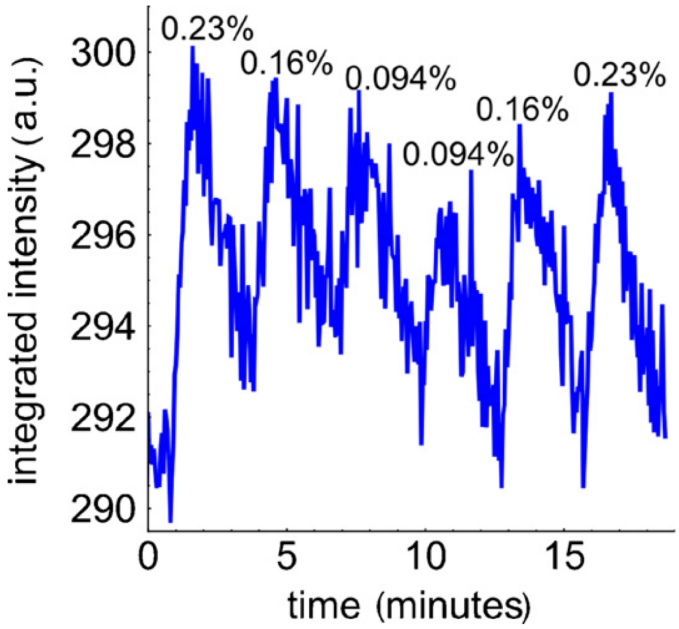

Figure A.9. Sensor response to various ethanol concentrations given as a mole percent above each peak.

This leads to the second point: the speed of analysis. For saturated vapors, the Si-QDs respond almost immediately, with the main delay being the ∼15 s required for the vapor to reach the testing chamber. Commercial ethanol detector technologies (*e.g.*, "breathalyzers") take a minute or less to provide a reading, with alternative sensor technologies capable of a similar range [236, 237, 240, 243]. In the present case, as discussed above there will be a tradeoff between analysis time and detection limit. However, the photoactivation rate depends on the optical intensity on the sample [125], so better coupling of the light source to the optical fiber could simultaneously increase the speed and lower the detection limit.

We can finally evaluate, briefly, the cost and re-usability of a Si-QD-based vapor sensor. The main experimental costs are the blue light source and a means to measure the luminescence intensity. This is common to many commercial devices that require a light source and a way to measure a solution color change. In contrast, optical ring resonators require a tunable laser, which places a large premium on the cost [244]. The QD-based fiber sensor investigated here can be cycled at least 30 times by periodically breathing into the testing chamber, without a significant degradation in the response. The overall cost of a device based on Si-QDs therefore appears

competitive with most proposed vapor sensing technologies.

Nevertheless, several outstanding issues must yet be addressed for this type of sensor, before any practical application can be realized. One of the most important is specificity. The Si-QD fiber sensor responds both to water vapor and to ethanol, which could make it difficult to use in "real-world" applications requiring the specific detection of alcohols. The response was different for the two cases however (Figs. A.5 and A.6), and can be made at least somewhat specific by pre-saturating it in the presence of the other vapor (Fig. A.7). Still, in cases where the ratios of the two vapors are unknown, specificity will, at this stage, be a significant problem.

The second issue is quantification. While clear trends are observed (*e.g.*, Fig. A.5 (b)), true quantification of the vapor concentration in the atmosphere is currently hampered by several underlying factors. First, there is a gradual drift in the luminescence over time, since the intensity generally did not completely revert to its lowest value after each exposure. This implies that quantification would change over time. Secondly, for the lowest vapor concentrations investigated (Fig. A.9), the variability in the integrated intensity under each peak is too large to clearly quantify the ethanol concentration. Thus, accurate quantification and clearly unambiguous analyte specificity are not possible with this structure, at the current time.

These issues may be related, at least in part, to sample-to-sample non-uniformity and aging. The number and concentration of QDs deposited onto the fiber surface is, at present, a significant problem that could make specificity and quantification much more difficult. This will affect not only the overall luminescence intensity, but also the overall photoactivation behavior, since large clumps like those shown in Fig. A.2 contain many buried QDs that may not be well exposed to the atmosphere. This problem can lead to considerable variation between different samples or batches, and we found that it takes both experimental care and some luck with a single batch to get results that were reproducible over timescales of a few days or weeks. This leads to the final issue: we observed an aging effect, in which the photoactivation properties of QDs suspended in toluene and stored in air gradually decayed over a similar period, probably as a result of gradual oxidation.

A.5 Conclusion

In this work, an optical fiber sensor with Si-QDs at the end facet was found to show a response to water and ethanol, a fast and reversible response time, and detection limits that could approach the range characteristic of standard ethanol sensors. The response is based on the QD fluorescence intensity which increases when the QDs are exposed under blue light irradiation to alcohol and water vapor. Reversibility is achieved by subsequent exposure to dry O_2. The magnitude of the fluorescence intensity change was found to depend on the vapor type and concentration: in 15-s exposures it was greatest for water vapor, intermediate for a water–ethanol mixture, and smallest for ethanol. The fluorescence sensor could be cycled more than 30 times without significant degradation of the performance. The work also showed the limitations of the proposed device structure, in which the two most significant were deemed to be selectivity and quantification, probably due mainly to physical clumping or agglomeration of the QDs on the fiber surface. The latter issue can lead to sample-to-sample variations in the response characteristics.

Acknowledgements

We thank the National Science and Engineering Research Council, Alberta Innovates Technology Futures and China Scholarship Council for funding this research. Thanks to Shalon McFarlane for SEM images, and Zhenyu Yang for assistance with sample etching.

Appendix B

Mathematica Analysis Code

DISCLAIMER: The sample code herein is provided "as is", without warranty of any kind, to the fullest extent permitted by law. The author does not warrant or guarantee the success individuals may have in implementing the sample code.

The following pages include code samples written in Mathematica used to analyze data generated from PL spectral, PL lifetime, and ESR experiments. Similar code was used throughout the thesis to generate graphs and figures. Datasets, along with the appropriate code, are available upon request from the author. The configuration most recently used to evaluate the Mathematica notebooks was: Mathematica 10.0.0 (Mac OS X x86, 64-bit kernel), running under OS X Yosemite 10.10 on a MacBook Pro (2.6 GHz Intel Core i7, 16 GB RAM).

PL Spectrum Analysis

Input Directories of Time-Series Spectral Data

```
(* Read in list of the directories from
 the data superdirectory and create a table *)
(* Note: superdirectory contains data in the following form:
 \\NotebookDirectory\\data\\datasets\\ *)

(* Set target directory *)
superdirectory = StringJoin[NotebookDirectory[], "data/"];
(* Change to target directory *)
SetDirectory[superdirectory];
(* Get dataset directory names - save as "directories" *)
directories = FileNames[];

(* On Macintosh, ignores .DS_Store hidden file *)
directories = DeleteCases[directories, ".DS_Store"];

(* Number of directories/datasets -
 IMPORTANT! "nod" used as a directory iterator, do not overwrite! *)
nod = Length[directories];

(* Make table of dataset directory name strings *)
alldirectories =
  Table[ToString[superdirectory] <> ToString[directories[[i]]], {i, nod}];

(* Displays a table of the datasets ready for import *)
TableForm[directories]
```

Import Data Sets

```
(* Read in each dataset from the directories above and create 'alldata' table *)
(* Note: dimensions of alldata = [directory,
  data set, data pair number = [wavelength, intensity] *)

(* Creates a list of filenames within each dataset directory *)
filenames = Table[FileNames[ToString[alldirectories[[i]]] <> "/*.txt"], {i, nod}];

(* Lists the number of files in each directory -
 IMPORTANT! "nof" used as a filename iterator, do not overwrite! *)
```

```
nof = Table[Length@filenames[[i]], {i, nod}];

(* Reads in the data from each filename in
 each directory. Can take a while, be patient! *)
alldata = Table[Import[#, "Data"] & /@ filenames[[i]][[1 ;; nof[[i]]]], {i, nod}];
```

Extract Integration Time

```
(* Extract integration time from
 headers and create 'allintegrationtime' table *)
(* Note: dimensions of allintegrationtime = [directory,dataset] *)

(* Take line 9 of header for integration time *)
allintegrationdata = Table[
    Take[alldata[[i, j]], {9}],
   {i, nod}, {j, nof[[i]]}];

(* Convert header line into string *)
allintegrationdata = Table[
    ToString[allintegrationdata[[i, j]]],
{i, nod}, {j, nof[[i]]}];

(* Extract numerical string of integration time from string *)
allintegrationdata = Table[
    (* Extract all numerical strings
    but use only the first (i.e., the integration time) *)
    StringCases[allintegrationdata[[i, j]], RegularExpression["\\d+"]][[1]],
{i, nod}, {j, nof[[i]]}];

(* Convert string to numerical value *)
allintegrationdata = Table[ToExpression[allintegrationdata[[i, j]]],
{i, nod}, {j, nof[[i]]}];
```

Extract Spectral Data

```
(* Extract spectral data from data sets and creat 'allspectraldata' table *)
(* Note: dimensions of allspectraldata = [directory,dataset] *)

allspectraldata = Table[
    (* Extract numerical pairs [wavelength, intensity] from data sets *)
       Take[alldata[[i, j]], {18, 2065}],
{i, nod}, {j, nof[[i]]}];
```

Filter Wavelength Range

```
maxlam = 950; (* Maximum wavelength *)
minlam = 550; (* Minimum wavelength *)

(* Apply a filter from minlam to maxlam upon spectral data *)
filterQ = Table[
    Cases[allspectraldata[[i, j]], {a_, b_} → maxlam > a > minlam],
{i, nod}, {j, nof[[i]]}];

allspectraldata = Table[
    Pick[allspectraldata[[i, j]], filterQ[[i, j]]],
{i, nod}, {j, nof[[i]]}];
```

Normalize Spectral Data

```
(* Normalize each spectrum to its corresponding integration time *)
allNspectraldata = Table[{allspectraldata[[i, j, k, 1]],
    N[allspectraldata[[i, j, k, 2]] / allintegrationdata[[i, j]]]},
{i, nod}, {j, nof[[i]]}, {k, Length@allspectraldata[[i, j]]}];

(* Find the global maximum *)
allMax = Max[allNspectraldata[[All, All, All, 2]]];

(* Normalize all sets to global maximum *)
allNspectraldata = Table[{allNspectraldata[[i, j, k, 1]],
    N[allNspectraldata[[i, j, k, 2]] / allMax]},
{i, nod}, {j, nof[[i]]}, {k, Length@allNspectraldata[[i, j]]}];
```

Generate Time Vectors

```
(* Extract time from headers and create 'timevector' table *)
(* Note: dimensions of timevector = [directory,dataset] *)

timevector = Table[
    (* Take line 3 of header for the time of collection *)
    Take[alldata[[i, j]], {3}],
   {i, nod}, {j, nof[[i]]}];


timevector = Table[
    (* Convert header line into string *)
    ToString[timevector[[i, j]]],
{i, nod}, {j, nof[[i]]}];
```

```
(* Extract numerical string of the time of collection from string *)
timevectorExtracted = Table[
    (* Extract all numerical strings but use only the 2nd,
   3rd and 4th (hours, minutes, seconds) *)
    StringCases[timevector[[i, j]], RegularExpression["\\d+"]][[{2, 3, 4}]],
{i, nod}, {j, nof[[i]]}];

(* Convert string to numerical value *)
timevectorExtracted = Table[
    ToExpression[timevectorExtracted[[i, j]]],
{i, nod}, {j, nof[[i]]}];

(* Convert to delta seconds from start time *)
timevectorConverted = Table[
    (* jth element time minus... *)
    (timevectorExtracted[[i, j]][[1]] * 60 * 60 +
      timevectorExtracted[[i, j]][[2]] * 60 + timevectorExtracted[[i, j]][[3]]) -
    (* ...start time *)
    (timevectorExtracted[[i, 1]][[1]] * 60 * 60 +
      timevectorExtracted[[i, 1]][[2]] * 60 + timevectorExtracted[[i, 1]][[3]]),
{i, nod}, {j, nof[[i]]}];
```

Integrate Numerical Data

```
(* Create interpolation function for spectral data *)
integrationfunctions =
  Table[Interpolation[allNspectraldata[[i, j]], {i, nod}, {j, nof[[i]]}];

(* Integrate spectral data
 (note: Quiet silences error reporting for NIntegrate) *)
integrationvalues = Quiet@Table[NIntegrate[integrationfunctions[[i, j]][x],
     {x, minlam, maxlam}], {i, nod}, {j, nof[[i]]}];

(* Calculate the maximum intensity in every directory *)
maxvals = Table[Max[integrationvalues[[i]]], {i, nod}];
```

Plot Time-Series Spectra Using a Rainbow Colormap

```
(* Be sure to install Mathematica's
 CustomTicks package prior to using this section *)
Needs["CustomTicks`"]

directorynumber = 1; (* select which directory to plot a time-series from *)

xmin = minlam;
xmax = maxlam;
ymin = 0;
ymax = 1;
```

```
ListPlot[Table[allNspectraldata[[directorynumber, j]], {j, nof[[directorynumber]]}],
    PlotStyle →
  Table[Hue[0.7 - j * 0.7 / nof[[directorynumber]]], {j, nof[[directorynumber]]}],
    PlotRange → {{xmin, xmax}, {ymin, ymax}},
    AspectRatio → 1,
    BaseStyle → FontSize → 18,
    AspectRatio → 1,
    ImageSize → 400,
    FrameStyle → Thick,
    Frame → {{True, True}, {True, True}},
    FrameTicksStyle → Black,
    FrameTicks → {
        {LinTicks[ymin, ymax, 0.2, 5, MajorTickLength → {0.03, 0},
     MinorTickLength → {0.015, 0}, ShowTickLabels → True],
        LinTicks[ymin, ymax, 0.2, 5, MajorTickLength → {0.03, 0},
     MinorTickLength → {0.015, 0}, ShowTickLabels → False]},
        {LinTicks[xmin, xmax, 50, 5, MajorTickLength → {0.03, 0},
     MinorTickLength → {0.015, 0}, ShowTickLabels → True],
        LinTicks[xmin, xmax, 50, 5, MajorTickLength → {0.03, 0},
     MinorTickLength → {0.015, 0}, ShowTickLabels → False]}},
    FrameLabel → {"wavelength (nm)", "intensity (a.u.)"}
]
```

Spectral Data Fitting

```
(* Find PL Max according to raw data *)
peakvals = Table[
    Max[allNspectraldata[[i, j, All, 2]]],
{i, 1, nod}, {j, 1, nof[[i]]}];

(* Find the index of the maxima in wavelength *)
maxindices = Table[
    Position[allNspectraldata[[i, j]], peakvals[[i, j]]][[1, 1]],
   {i, 1, nod}, {j, 1, nof[[i]]}
];

(* Find the corresponding wavelength of maximum *)
peaklams = Table[
    allNspectraldata[[i, j]][[maxindices[[i, j]]][[1]], {i, 1, nod}, {j, 1, nof[[i]]}
];
(* Fits each spectra in each directory to a skew-normal function *)

nlmspectraSN = Quiet@Table[
NonlinearModelFit[
    (* data to fit *)
    allNspectraldata[[i, j]],
    (* function to apply *)
```

```
    {A * Exp[-Log[2] * (Log[1 + (2 b * (x - μ))/σ] * 1/b)^2]},
    (* variables and their initial guesses *)
    {{A, integrationvalues[[i, j]]},
      {μ, (peaklams[[i, j]] + 825) / 2}, {σ, 200}, {b, 0.10}}, x]
, {i, nod}, {j, nof[[i]]}];

μfitvalsSN = Table[nlmspectraSN[[i, j, 1, 2]][[2, 2]], {i, nod}, {j, nof[[i]]}];

(* Fits each spectra in each directory to a gaussian function *)
nlmspectraG = Quiet@Table[
NonlinearModelFit[
    (* data to fit *)
    allNspectraldata[[i, j]],
    (* function to apply *)
    {A / (σ * Sqrt[2 * Pi]) * Exp[-(x - μ)^2 / (2 * σ^2)]},
    (* variables and their initial guesses *)
    {{A, integrationvalues[[i, j]]}, {μ, (peaklams[[i, j]] + 825) / 2}, {σ, 200}}, x]
, {i, nod}, {j, nof[[i]]}];

μfitvalsG = Table[nlmspectraG[[i, j, 1, 2]][[2, 2]], {i, nod}, {j, nof[[i]]}];

(* Fits each spectra in each directory to a lorentzian function*)
nlmspectraL = Quiet@Table[
NonlinearModelFit[
    (* data to fit *)
    allNspectraldata[[i, j]],
    (* function to apply *)
    {A / Pi * (γ / ((x - μ)^2 + γ^2))},
    (* variables and their initial guesses *)
    {{A, integrationvalues[[i, j]]}, {μ, (peaklams[[i, j]] + 825) / 2}, {γ, 200}}, x]
, {i, nod}, {j, nof[[i]]}];

μfitvalsL = Table[nlmspectraL[[i, j, 1, 2]][[2, 2]], {i, nod}, {j, nof[[i]]}];
```

Plot Fitting Results

```
directorynumber = 1; (* Directory of dataset *)
filenumber = 500; (* Spectrum within dataset to plot *)

Show[
    (* raw data *)
    ListPlot[
        allNspectraldata[[directorynumber, filenumber]],
        PlotStyle → {Blue, Thick},
        PlotRange → {{xmin, xmax}, {ymin, ymax}},
```

```
        AspectRatio → 1,
        BaseStyle → FontSize → 18,
        AspectRatio → 1,
        ImageSize → 400,
        FrameStyle → Thick,
        Frame → {{True, True}, {True, True}},
        FrameTicksStyle → Black,
        FrameTicks → {
            {LinTicks[ymin, ymax, 0.2, 5, MajorTickLength → {0.03, 0},
      MinorTickLength → {0.015, 0}, ShowTickLabels → True],
            LinTicks[ymin, ymax, 0.2, 5, MajorTickLength → {0.03, 0},
      MinorTickLength → {0.015, 0}, ShowTickLabels → False]},
            {LinTicks[xmin, xmax, 50, 5, MajorTickLength → {0.03, 0},
      MinorTickLength → {0.015, 0}, ShowTickLabels → True],
            LinTicks[xmin, xmax, 50, 5, MajorTickLength → {0.03, 0},
      MinorTickLength → {0.015, 0}, ShowTickLabels → False]}},
        FrameLabel → {"wavelength (nm)", "intensity (a.u.)"}
    ],

    (* skew-normal fit *)
    Plot[nlmspectraSN[[directorynumber, filenumber]][x], {x, minlam, maxlam},
    PlotStyle → {Red, Thickness[0.01]}],

    (* gaussian fit *)
    Plot[nlmspectraG[[directorynumber, filenumber]][x], {x, minlam, maxlam},
    PlotStyle → {Green, Thickness[0.01]}],

    (* lorentzian fit *)
    Plot[nlmspectraL[[directorynumber, filenumber]][x], {x, minlam, maxlam},
    PlotStyle → {Orange, Thickness[0.01]}]
]
```

Plot Intensity vs Time

```
directorynumber = 1;

ListPlot[
    Table[{timevectorConverted[[directorynumber, i]] / 60,
   integrationvalues[[directorynumber, i]] /
    Max[integrationvalues[[All, All]]]}, {i, nof[[1]]}],
    BaseStyle → FontSize → 18,
    PlotMarkers → Graphics[{Blue, Thick, Circle[]}, ImageSize -> 10],
    AspectRatio → 1,
    BaseStyle → FontSize → 18,
    FrameStyle → Thick,
    ImageSize → 400,
    Axes → {True, False},
    Frame → {{True, True}, {True, True}},
    FrameTicksStyle → Black,
    FrameTicks → {
        {LinTicks[0, 1, 0.2, 5, MajorTickLength → {0.03, 0},
     MinorTickLength → {0.015, 0}, ShowTickLabels → True],
```

```
        LinTicks[0, 1, 0.2, 5, MajorTickLength → {0.03, 0},
      MinorTickLength → {0.015, 0}, ShowTickLabels → False]},
        {LinTicks[0, 60, 10, 5, MajorTickLength → {0.03, 0},
      MinorTickLength → {0.015, 0}, ShowTickLabels → True],
        LinTicks[0, 60, 10, 5, MajorTickLength → {0.03, 0},
      MinorTickLength → {0.015, 0}, ShowTickLabels → False]}},
    FrameLabel → {"time (minutes)", "intensity (a.u.)"}
    ]
```

Overlayed Intensity vs Time Plots

```
ListPlot[
    Table[{timevectorConverted[[i, j]] / 60, integrationvalues[[i, j]] /
     Max[integrationvalues[[All, All]]]}, {i, nod}, {j, nof[[i]]}],
    BaseStyle → FontSize → 18,
    PlotMarkers → Graphics[{Thick, Circle[]}, ImageSize -> 10],
    PlotStyle -> Table[Hue[0.7 - i * 0.7 / nod], {i, nod}],
    AspectRatio → 1,
    BaseStyle → FontSize → 18,
    FrameStyle → Thick,
    ImageSize → 400,
    Axes → {True, False},
    Frame → {{True, True}, {True, True}},
    FrameTicksStyle → Black,
    FrameTicks → {
        {LinTicks[0, 1, 0.2, 5, MajorTickLength → {0.03, 0},
      MinorTickLength → {0.015, 0}, ShowTickLabels → True],
        LinTicks[0, 1, 0.2, 5, MajorTickLength → {0.03, 0},
      MinorTickLength → {0.015, 0}, ShowTickLabels → False]},
        {LinTicks[0, 60, 10, 5, MajorTickLength → {0.03, 0},
      MinorTickLength → {0.015, 0}, ShowTickLabels → True],
        LinTicks[0, 60, 10, 5, MajorTickLength → {0.03, 0},
      MinorTickLength → {0.015, 0}, ShowTickLabels → False]}},
    FrameLabel → {"time (minutes)", "intensity (a.u.)"}
]
```

Overlayed Peak Wavelength vs Time Plots

```
ListPlot[
    Table[{timevectorConverted[[i, j]] / 60, μfitvalsSN[[i, j]]}, {i, nod}, {j, nof[[i]]}],
    PlotRange → {{0, 60}, {740, 900}},
    BaseStyle → FontSize → 18,
    PlotMarkers → Graphics[{Thick, Circle[]}, ImageSize -> 10],
    PlotStyle -> Table[Hue[0.7 - i * 0.7 / nod], {i, nod}],
    AspectRatio → 1,
    BaseStyle → FontSize → 18,
    FrameStyle → Thick,
```

```
    ImageSize → 400,
    Axes → {True, False},
    Frame → {{True, True}, {True, True}},
    FrameTicksStyle → Black,
    FrameTicks → {
        {LinTicks[740, 900, 20, 5, MajorTickLength → {0.03, 0},
     MinorTickLength → {0.015, 0}, ShowTickLabels → True],
        LinTicks[740, 900, 20, 5, MajorTickLength → {0.03, 0},
     MinorTickLength → {0.015, 0}, ShowTickLabels → False]},
        {LinTicks[0, 60, 10, 5, MajorTickLength → {0.03, 0},
     MinorTickLength → {0.015, 0}, ShowTickLabels → True],
        LinTicks[0, 60, 10, 5, MajorTickLength → {0.03, 0},
     MinorTickLength → {0.015, 0}, ShowTickLabels → False]}},
    FrameLabel → {"time (minutes)", "peak wavelength (nm)"}
]
```

PL Lifetime Analysis

Input Directories of Lifetime Data

```
(* Read in list of the datasets from the data directory and create a table *)
(* Note: directory contains data in the following form:
 \\NotebookDirectory\\data\\datasets *)


(* Set target directory *)
directory = StringJoin[NotebookDirectory[], "data/"];
(* Change to target directory *)
SetDirectory[directory];
(* Get data filenames - save as "filenames" *)
filenames = FileNames[];

(* On Macintosh, ignores .DS_Store hidden file *)
filenames = DeleteCases[filenames, ".DS_Store"];

(* Number of datasets - IMPORTANT! "nof" used as a directory iterator,
do not overwrite! *)
nof = Length[filenames];

(* Make table of filepaths directory name strings *)
filepaths = Table[ToString[directory] <> ToString[filenames[[i]]], {i, nof}];

(* Displays a table of the datasets ready for import *)
TableForm[filepaths]
```

Import Data Sets

```
(* Read in each dataset from the directories above and create 'data' table *)

(* Reads in the data from each filename. Can take a while, be patient! *)
data = Table[Import[filenames[[j]], "Data"], {j, nof}];

(* specific boundaries need to be
 gathered depending on the experimental setup *)
n = 4000; (* number of data points in a set *)
tpp = 5.0 * 10^-7; (* associated time per point in seconds *)

data[[1]][[4013]];(* First Data Point *)
data[[1]][[4013 + 1999]]; (* First Data Point of Decay *)
data[[1]][[4013 + 1 - 2 + n / 2]];(* First Data Point of Decay *)
```

```
data[[1]][[4013 + 3999]]; (* Last Data Point *)

time = Table[i * tpp, {j, nof}, {i, n / 2}]; (* Generates Time Vector *)

decay = Table[ToExpression[data[[j]][[4013 + n / 2 + (i - 1)]]], {j, nof}, {i, n / 2}];
(* Generates Decay Vector *)

(* for some reason, sets 8 and 9 don't import corrrectly,
this fixes those files *)
decay[[8]] = Flatten@decay[[8]];
decay[[9]] = Flatten@decay[[9]];

(* Concatenates Time and Decay Vectors *)
listdecay = Table[{time[[j, i]] / 10^-6, decay[[j, i]]}, {j, nof}, {i, n / 2}];
(* note, converted seconds to microseconds in listdecay *)
```

Plot a Time-Decay Curve

```
(* Be sure to install Mathematica's
 CustomTicks package prior to using this section *)
Needs["CustomTicks`"]

set = 3; (* select which dataset to plot a time-decay curve *)

xmin = 0;
xmax = Max[time[[set]] / 10^-6];
ymin = 0;
ymax = Round[Max[decay[[set]]], 1000];

ListLinePlot[listdecay[[set]],
     PlotRange → {{xmin, xmax}, {ymin, ymax}},
     AspectRatio → 1,
     BaseStyle → FontSize → 18,
     AspectRatio → 1,
     ImageSize → 400,
     FrameStyle → Thick,
     Frame → {{True, True}, {True, True}},
     FrameTicksStyle → Black,
     FrameTicks → {
         {LinTicks[0, ymax, ymax / 5, 5, MajorTickLength → {0.03, 0},
      MinorTickLength → {0.015, 0}, ShowTickLabels → True, DecimalDigits -> 0],
         LinTicks[0, ymax, ymax / 5, 5, MajorTickLength → {0.03, 0},
      MinorTickLength → {0.015, 0}, ShowTickLabels → False]},
         {LinTicks[0, xmax, xmax / 4, 5, MajorTickLength → {0.03, 0},
      MinorTickLength → {0.015, 0}, ShowTickLabels → True, DecimalDigits -> 0],
         LinTicks[0, xmax, xmax / 4, 5, MajorTickLength → {0.03, 0},
      MinorTickLength → {0.015, 0}, ShowTickLabels → False]}},
     FrameLabel → {"time (μs)", "intensity (a.u.)"}
]
```

Plot Time-Series of PL Lifetimes

```
(* Plots each decay sequentially *)

xmin = 0;
xmax = Max[time[[All]] / 10^-6];
ymin = 0;
ymax = Round[Max[decay[[All]]], 1000];

ListLinePlot[listdecay,
     PlotStyle → Table[Hue[0.7 - 0.7 / (nof - 1) * (i - 1)], {i, nof}],
     PlotRange → {{xmin, xmax}, {ymin, ymax}},
     AspectRatio → 1,
     BaseStyle → FontSize → 18,
     AspectRatio → 1,
     ImageSize → 400,
     FrameStyle → Thick,
     Frame → {{True, True}, {True, True}},
     FrameTicksStyle → Black,
     FrameTicks → {
         {LinTicks[0, ymax, ymax / 5, 5, MajorTickLength → {0.03, 0},
      MinorTickLength → {0.015, 0}, ShowTickLabels → True, DecimalDigits -> 0],
         LinTicks[0, ymax, ymax / 5, 5, MajorTickLength → {0.03, 0},
      MinorTickLength → {0.015, 0}, ShowTickLabels → False]},
         {LinTicks[0, xmax, xmax / 4, 5, MajorTickLength → {0.03, 0},
      MinorTickLength → {0.015, 0}, ShowTickLabels → True, DecimalDigits -> 0],
         LinTicks[0, xmax, xmax / 4, 5, MajorTickLength → {0.03, 0},
      MinorTickLength → {0.015, 0}, ShowTickLabels → False]}},
     FrameLabel → {"time (μs)", "intensity (a.u.)"}
]
```

Lifetime Data Fitting

```
Aguess = Table[listdecay[[j, 1, 2]], {j, nof}];
(* initial guess for the total intensity, A *)
Cguess = Table[listdecay[[j, 2000, 2]], {j, nof}];
(* initial guess for the DC offset, C *)

(* code to identify an initial guess for the lifetime, τ *)
value = Table[Nearest[listdecay[[j, All, 2]], N[Aguess[[j]] / E]], {j, nof}];
(* find the 1/e intensity *)
indexes = Flatten[Table[Position[listdecay[[j]], value[[j, 1]]], {j, nof}], 1];
(* find the corresponding time-point *)
indexes = indexes[[All, 1]];
τguess = Table[listdecay[[j, indexes[[j]], 1]], {j, nof}];
(* table of initial guess for τ *)

(* guesses for initial values of beta are done manually *)
(* in this case, guesses for beta are copied and pasted from
 the output of the fitting function over several iterations *)
(* WARNING: THIS MAY PRODUCE RESULTS AT LOCAL MINIMA *)
```

```
βguess = {0.7577484145757432, 0.7470710564578465,
    0.7449697593094032, 0.7387992567655999, 0.73, 0.695744399305555,
    0.6892931627950571, 0.6790328082578511, 0.6415922622114445, 0.64};

(* fits each lifetime to a stretched-exponential function *)

nlm = Quiet@Table[
NonlinearModelFit[
     (* data to fit *)
     listdecay[[j]],
     (* function to apply *)
     {A * Exp[-(t / τ)^β] + C, Aguess[[j]] - 10 < A < Aguess[[j]] + 10,
       0 < C < Cguess[[j]], 0.000005 < τ < τguess[[j]], 0.01 < β < .99},
     (* variables and their initial guesses *)
     {{A, Aguess[[j]]}, {τ, τguess[[j]]}, {β, βguess[[j]]}, {C, Cguess[[j]]}}, t]
, {j, nof}];

(* fitting results displayed in table form *)

nlmparams = Table[nlm[[i]]["BestFitParameters"], {i, 1, nof}];
TableForm@Table[nlm[[i]]["BestFitParameters"], {i, 1, nof}]

(* lifetime decay data plotted with the associated fit *)

set = 3; (* select which dataset to plot a time-decay curve *)

xmin = 0;
xmax = Max[time[[All]] / 10^-6];
ymin = 0;
ymax = Round[Max[decay[[All]], 1000];

Show[

    ListLinePlot[
        listdecay[[set]],
        PlotRange → {{xmin, xmax}, {ymin, ymax}},
        AspectRatio → 1,
        BaseStyle → FontSize → 18,
        AspectRatio → 1,
        ImageSize → 400,
        FrameStyle → Thick,
        Frame → {{True, True}, {True, True}},
        FrameTicksStyle → Black,
        FrameTicks → {
            {LinTicks[0, ymax, ymax / 5, 5, MajorTickLength → {0.03, 0},
      MinorTickLength → {0.015, 0}, ShowTickLabels → True, DecimalDigits -> 0],
            LinTicks[0, ymax, ymax / 5, 5, MajorTickLength → {0.03, 0},
      MinorTickLength → {0.015, 0}, ShowTickLabels → False]},
            {LinTicks[0, xmax, xmax / 4, 5, MajorTickLength → {0.03, 0},
      MinorTickLength → {0.015, 0}, ShowTickLabels → True, DecimalDigits -> 0],
            LinTicks[0, xmax, xmax / 4, 5, MajorTickLength → {0.03, 0},
      MinorTickLength → {0.015, 0}, ShowTickLabels → False]}},
        FrameLabel → {"time (μs)", "intensity (a.u.)"}
    ],
```

```
    Plot[nlm[[set]][x], {x, 10^-6, xmax / 5},
    PlotStyle → {Red, Thick}],

    (* graphing error requires second interval to appear *)
    Plot[nlm[[set]][x], {x, xmax / 5, xmax},
    PlotStyle → {Red, Thick}]
]
```

Tables of Fitting Values

```
(* intensity, A, fit values *)
afitvals = Table[nlmparams[[i]][[1]], {i, 1, nof}];

(* lifetime, τ, fit values (μs) *)
taufitvals = Table[nlmparams[[i]][[2]], {i, 1, nof}];

(* stretching factor, β, fit values *)
betafitvals = Table[nlmparams[[i]][[3]], {i, 1, nof}];

(* DC offset, C, fit values *)
cfitvals = Table[nlmparams[[i]][[4]], {i, 1, nof}];

(* visualizetion of τ fits as a function of dataset *)
ListPlot[taufitvals[[All, 2]],
    Frame → {{True, True}, {True, True}},
    FrameLabel → {"dataset", "lifetime τ (μs)"}]

Show[
    Table[ListLinePlot[
        listdecay[[j]],
        PlotRange → {{xmin, xmax}, {ymin, ymax}},
        PlotStyle → Hue[0.7 - 0.7 / (nof - 1) * (j - 1)],
        AspectRatio → 1,
        BaseStyle → FontSize → 18,
        AspectRatio → 1,
        ImageSize → 400,
        FrameStyle → Thick,
        Frame → {{True, True}, {True, True}},
        FrameTicksStyle → Black,
        FrameTicks → {
            {LinTicks[0, ymax, ymax / 5, 5, MajorTickLength → {0.03, 0},
          MinorTickLength → {0.015, 0}, ShowTickLabels → True, DecimalDigits -> 0],
            LinTicks[0, ymax, ymax / 5, 5, MajorTickLength → {0.03, 0},
          MinorTickLength → {0.015, 0}, ShowTickLabels → False]},
            {LinTicks[0, xmax, xmax / 4, 5, MajorTickLength → {0.03, 0},
          MinorTickLength → {0.015, 0}, ShowTickLabels → True, DecimalDigits -> 0],
            LinTicks[0, xmax, xmax / 4, 5, MajorTickLength → {0.03, 0},
          MinorTickLength → {0.015, 0}, ShowTickLabels → False]}},
        FrameLabel → {"time (μs)", "intensity (a.u.)"}
    ], {j, nof}],

    Table[Plot[nlm[[j]][x], {x, 10^-6, xmax / 5},
```

```
    PlotStyle → {Black}], {j, nof}],

    (* graphing error requires second interval to appear *)
    Table[Plot[nlm[[j]][x], {x, xmax / 5, xmax},
    PlotStyle → {Black}], {j, nof}]
]
```

ESR Analysis

Input File Names

```
(* Read in list of the datasets from the data directory and create a table *)
(* Note: directory contains data in the following form:
 \\NotebookDirectory\\data\\datasets *)

(* Set target directory *)
directory = StringJoin[NotebookDirectory[], "data/"];

(* Change to target directory *)
SetDirectory[directory];

(* Get data filenames - save as "filenames" *)
filenames = FileNames[];

(* Number of datasets - IMPORTANT! "nof" used as a directory iterator,
do not overwrite! *)
nof = Length[filenames];

(* Make table of filepaths directory name strings *)
filepaths = Table[ToString[directory] <> ToString[filenames[[i]]], {i, nof}];

(* Displays a table of the datasets ready for import *)
TableForm[filepaths]
```

Import Data Sets

```
(* Read in each dataset from the directories above and create 'data' table *)

(* Reads in the data from each filename. Can take a while, be patient! *)
data = Table[Import[filenames[[j]], "Data"], {j, nof}];

(* Generates an index spectral header variable *)
header = Table[data[[i]][[1 ;; 4]], {i, nof}];

(* Generates an indexed spectral data variable *)
spectrum = Table[data[[i]][[5 ;; 1028]], {i, nof}];
```

Other Setup Data

```
(* Microwave frequency in GHz *)
ν = 9.356166;

(* Plank's constant in J/GHz *)
h = 6.62607 * 10^-25;

(* Bohr magneton in J/G *)
μb = 9.274 * 10^-28;

(* g-factor - used to recalculate plot axes *)
g[B_] := (h * ν / μb) / B;

(* field as a function of g-factor *)
B[g_] := (h * ν / μb) / g;

(* used to generate the g-factor axes in graphs *)
gticks = {6685 / #, NumberForm[N@#, {4, 4}]} & /@ FindDivisions[6685 / {##}, 8] &;

xMin = Table[Min[spectrum[[i, All, 1]]], {i, nof}];
xMax = Table[Max[spectrum[[i, All, 1]]], {i, nof}];
yMin = Table[Min[spectrum[[i, All, 2]]] * 1.1, {i, nof}];
yMax = Table[Max[spectrum[[i, All, 2]]] * 1.1, {i, nof}];
```

Import Background

```
bdirectory = StringJoin[NotebookDirectory[], "background/"];
(* Set background directory *)
SetDirectory[bdirectory]; (* Change to background directory *)
backgroundname = FileNames[]; (* Get filename *)
backgroundpath = ToString[bdirectory] <> ToString[backgroundname[[1]]];
(* Make filepathes *)

background = Import[backgroundpath, "Data"];
(* Reads in the data. Can take a while. *)
backgroundheader = background[[1 ;; 4]];
(* Generates an index spectral header variable *)
backgroundspectrum = background[[5 ;; 1028]];
(* Generates an indexed spectral data variable *)

ListLinePlot[backgroundspectrum, Frame → True,
PlotRange → {{Min[backgroundspectrum[[All, 1]]], Max[backgroundspectrum[[All, 1]]]},
    {Min[backgroundspectrum[[All, 2]]] * 1.1, Max[backgroundspectrum[[All, 2]]] * 1.1}},
FrameLabel → {"Magnetic Field (G)", "Intensity (a.u.)", "g-factor"},
FrameTicks → {{Automatic, None}, {Automatic, gticks}},
Axes → {True, False}
]
```

Subtract Background from All Spectra

```
(* point-wise subtraction of the background from all datasets *)
spectrumsubtracted =
  Table[{spectrum[[i, j, 1]], spectrum[[i, j, 2]] - backgroundspectrum[[j, 2]]},
   {i, nof}, {j, Length[backgroundspectrum]}];
```

Plot Raw Data Sets

```
set = 1; (* select which dataset to plot *)

ListLinePlot[spectrumsubtracted[[set]],
     Frame → True,
     PlotRange → {{xMin[[set]], xMax[[set]]}, {yMin[[set]], yMax[[set]]}},
     FrameLabel → {"Magnetic Field (G)", "Intensity (a.u.)", "g-factor"},
     FrameTicks → {{Automatic, None}, {Automatic, gticks}},
     Axes → {True, False}
]
```

Plot Overlayed Raw Data Sets

```
(* Be sure to install Mathematica's
 CustomTicks package prior to using this section *)
Needs["CustomTicks`"]

xmin = 3300;
xmax = 3360;
ymin = -8000;
ymax = 7000;

ListLinePlot[Table[spectrumsubtracted[[i]], {i, nof}],
     PlotStyle → Table[Hue[0.7 - i * 0.7 / nof], {i, nof}],
     PlotRange → {{Min[spectrum[[All, All, 1]]], Max[spectrum[[All, All, 1]]]},
    {Min[spectrum[[All, All, 2]]] * 1.1, Max[spectrum[[All, All, 2]]] * 1.1}},
     BaseStyle → FontSize → 18,
     ImageSize → 500,
     Axes → False,
     AspectRatio → 0.8,
     FrameStyle → Thick,
     Frame → {{True, True}, {True, True}},
     FrameTicksStyle → Black,
     FrameTicks → {
         {LinTicks[-8000, 8000, 2000, 3,
       MajorTickLength → {0.03, 0}, MinorTickLength → {0.015, 0}],
          LinTicks[-8000, 8000, 2000, 3, MajorTickLength → {0.03, 0},
       MinorTickLength → {0.015, 0}, ShowTickLabels → False]},
          {LinTicks[3300, 3360, 10, 5, MajorTickLength → {0.03, 0},
       MinorTickLength → {0.015, 0}],
```

```
        gticks}}]
```

Fitting Raw Data Sets with Gaussian Derivatives

```
(* initial guesses for ESR fitting *)

fwhmMin = 1; (* FWHM lower bound *)
fwhmMax = 3.5; (* FWHM upper bound *)

(* Common g-factors of defects in silicon, values in g-factor *)
gperpguess = 2.0086;
gparaguess = 2.0019;
gDguess = 2.0053;

(* Initial intensity guesses for all defects *)
Agperpguess = 20 000;
Agparaguess = 20 000;
AgDguess = 2000;

(* Initial FWHM guesses for all defects *)
σgparaguess = 2.5;
σgperpguess = 2.5;
σgDguess = 2.5;

(* fits each ESR spectrum with a Gaussian (Normal Distribution) function *)
(* to fit with a Lorentzian,
replace NormalDistribution with CauchyDistribution *)

nlm = Quiet@Table[NonlinearModelFit[
    (* data to fit *)
    spectrumsubtracted[[i]],
    (* function to apply, note the use of D[ ] to take derivatives *)
    {Evaluate[D[Agpara * PDF[NormalDistribution[B[gpara], σgpara], x] +
          Agperp * PDF[NormalDistribution[B[gperp], σgperp], x] +
          AgD * PDF[NormalDistribution[B[gD], σgD], x], x]],
    (* variables and their initial guesses *)
    {0 < Agpara < 23 000, 0 < Agperp, 0 < AgD,
       fwhmMin < σgpara < fwhmMax, fwhmMin < σgperp < fwhmMax, 1 < σgD < fwhmMax,
       2.0009 < gpara < 2.0039, 2.006 < gperp < 2.0090,  2.0033 < gD < 2.0073}},
    {{Agpara, Agparaguess}, {σgpara, σgparaguess}, {gpara, gparaguess}, {Agperp,
       Agperpguess}, {σgperp, σgperpguess}, {gperp, gperpguess}, {AgD, AgDguess},
      {σgD, σgDguess}, {gD, gDguess}}, x, ConfidenceLevel → 0.999999999]
,
    {i,
     nof}];

(* fitvalues from ESR spectrum fitting *)

(* gpara defect *)
Agparafitvals = Table[nlm[[i, 1, 2, 1, 2]], {i, nof}]; (* intensity, A *)
σgparafitvals = Table[nlm[[i, 1, 2, 2, 2]], {i, nof}]; (* linewidth, σ *)
gparafitvals = Table[nlm[[i, 1, 2, 3, 2]], {i, nof}]; (* g-factor, g *)
```

```
(* gperp defect *)
Agperpfitvals = Table[nlm[[i, 1, 2, 4, 2]], {i, nof}];
σgperpfitvals = Table[nlm[[i, 1, 2, 5, 2]], {i, nof}];
gperpfitvals = Table[nlm[[i, 1, 2, 6, 2]], {i, nof}];

(* gD defect *)
AgDfitvals = Table[nlm[[i, 1, 2, 7, 2]], {i, nof}];
σgDfitvals = Table[nlm[[i, 1, 2, 8, 2]], {i, nof}];
gDfitvals = Table[nlm[[i, 1, 2, 9, 2]], {i, nof}];

(* fitting results displayed in table form *)
TableForm[nlm[[All, 1, 2]]]
```

Plot Raw Data Set with Decomposed Gaussian Derivative Fits

```
(* ESR spectral data plotted with the associated defect fits and total fit *)

set = 4; (* select which dataset to plot the ESR fits *)

Show[
    ListLinePlot[spectrumsubtracted[[set]],
  PlotRange → {{xMin[[set]], xMax[[set]]}, {yMin[[set]], yMax[[set]]}}, PlotStyle → Black,
    BaseStyle → FontSize → 18,
    ImageSize → 500,
    Axes → False,
    AspectRatio → 0.8,
    FrameStyle → Thick,
    Frame → {{True, True}, {True, True}},
    FrameTicksStyle → Black,
    FrameTicks →
   {{LinTicks[-8000, 8000, 2000, 5, MajorTickLength → {0.03, 0}, MinorTickLength →
        {0.015, 0}], LinTicks[-8000, 8000, 2000, 5, MajorTickLength → {0.03, 0},
      MinorTickLength → {0.015, 0}, ShowTickLabels → False]},
    {LinTicks[3300, 3360, 10, 5, MajorTickLength → {0.03, 0},
      MinorTickLength → {0.015, 0}], gticks}}

],

    Plot[Evaluate[D[Agparafitvals[[set]] *
      PDF[NormalDistribution[B[gparafitvals[[set]]], σgparafitvals[[set]]], x], x]],
  {x, Min[spectrum[[set, All, 1]]], Max[spectrum[[set, All, 1]]]},
       PlotRange → {{xMin[[set]], xMax[[set]]}, {yMin[[set]], yMax[[set]]}},
       PlotStyle → {Thick, Red}],

    Plot[Evaluate[D[Agperpfitvals[[set]] *
      PDF[NormalDistribution[B[gperpfitvals[[set]]], σgperpfitvals[[set]]], x], x]],
  {x, Min[spectrum[[set, All, 1]]], Max[spectrum[[set, All, 1]]]},
       PlotRange → {{xMin[[set]], xMax[[set]]}, {yMin[[set]], yMax[[set]]}},
       PlotStyle → {Thick, Green}],

    Plot[Evaluate[D[AgDfitvals[[set]] *
      PDF[NormalDistribution[B[gDfitvals[[set]]], σgDfitvals[[set]]], x], x]],
```

```
  {x, Min[spectrum[[set, All, 1]]], Max[spectrum[[set, All, 1]]]},
        PlotRange → {{xMin[[set]], xMax[[set]]}, {yMin[[set]], yMax[[set]]}},
        PlotStyle → {Thick, Blue}],

    Plot[nlm[[set]][x], {x, Min[spectrum[[set, All, 1]]], Max[spectrum[[set, All, 1]]]},
        PlotRange → {{xMin[[set]], xMax[[set]]}, {yMin[[set]], yMax[[set]]}},
        PlotStyle → {Thick, Magenta}]
]

(* plot of defect intensitys as a function of photoactivation time *)

PAtime = {-1, 0, 5, 10, 15, 60};
(* experimentally determined photoactivation times (a priori) *)

g1 = ListLinePlot[Table[{PAtime[[i]], Agparafitvals[[i]]}, {i, nof}],
   PlotRange → {{-1, 65}, {0, 370 000}},
    BaseStyle → FontSize → 18,
    Axes → {True, False},
    Frame → {{True, True}, {True, True}},
    PlotStyle → {Red, Thickness[0.01], Dashed},
    FrameTicks → {{Automatic, None}, {Automatic, None}},
    FrameStyle → Thick,
    AspectRatio → 1,
    ImageSize → 500,
    FrameStyle → Thick,
    PlotMarkers → {●, 25},
    FrameLabel → {Style["photoactivation time (mins)", Bold, 20],
     Style["g-factor intensity (a.u.)", Bold, 20]}
    ];
g2 = ListLinePlot[Table[{PAtime[[i]], Agperpfitvals[[i]]}, {i, nof}],
   PlotStyle → {Green, Thickness[0.01], Dashed}, PlotMarkers → {●,
  25}];
g3 = ListLinePlot[Table[{PAtime[[i]], AgDfitvals[[i]]}, {i, nof}],
   PlotStyle → {Blue, Thickness[0.01], Dashed}, PlotMarkers -> {●, 25}];

g4 = ListLinePlot[
   Table[{PAtime[[i]], Agparafitvals[[i]] + Agperpfitvals[[i]] + AgDfitvals[[i]]}, {i, nof}],
   PlotStyle → {Black, Thickness[0.01], Dashed}, PlotMarkers -> {●, 25}];

Show[g1, g2, g3, g4]
```